UNIVERSITY OF CALIFORNIA, SAN DIEGO

Structural Studies of Ternary Mixture Lipid Multilayer Systems and the Effect of High Hydration with X-ray Diffraction

A dissertation submitted in partial satisfaction of the
requirements for the degree
Doctor of Philosophy

in

Physics

by

Yicong Ma

Committee in charge:

Professor Sunil K. Sinha, Chair
Professor Terry Hwa
Professor Judy Kim
Professor Ratnesh Lal
Professor Oleg Shpyrko

2015

The dissertation of Yicong Ma is approved, and it is acceptable in quality and form for publication on microfilm and electronically:

_____

_____

_____

_____

_____
Chair

University of California, San Diego

2015

DEDICATION

To Yanjin.

TABLE OF CONTENTS

LIST OF FIGURES

LIST OF TABLES

ACKNOWLEDGEMENTS

First and foremost, I would like to express my sincere gratitude to my thesis advisor, Professor Sunil Sinha, for sharing his wisdom and giving me encouraging guidance and constant support throughout my journey of grad school. PhD is a tough journey. I am lucky to have him as my mentor who teaches me science, gives me freedom and support to explore, and takes me under his wings when things go awry. His serious attitude towards science, optimistic spirit towards life, and a noble character, have inspired me, and will benefit me deeply in my future.

I would also like to thank some special people who have extended their caring hands to me at my most difficult times. I owe a big thank to Hyunjung Kim, who helped me fix my first piece of equipment, encouraged me when I lost heart, acknowledged my growth when she saw my progress, which all meant a lot to me. I would also like to thank Zhang Jiang, Mrinmay Mukhopadhyay, who have given guidance and encouragement to me, and inspired me with their knowledge and insights. I would like to thank Larry Lurio, who has contributed tremendous amount of time and knowledge to this research, whose lovely character I deeply appreciate. I would like to thank Atul Parikh, for sharing his humor and insights and giving me guidance and care to my graduation. I would like to thank David Worcester for sharing his knowledge with me, lending us the sample chamber and showing hospitality to invite me to his wifes delicious cooking when I did not have a place for dinner at NIST. I would like to thank Brad Hanson, who has taught me using the machine shop and spent extra time and effort helping me make my humidity chamber. Special thanks go to San-Wen Chen, my 5$\sim$6 year office mate and lab mate, for mentoring me, helping me like my brother, and caring about me as my friend.

This research cannot be done by one alone. I would like to thank Sajal Ghosh, Sambunath Bera who contributed a lot of time and knowledge to this work, particularly helping to take long shifts at the beamline. I would like to thank Curt DeCaro, Justin Berry, Wonsuk Cha, who have helped me and supported me in the research, and being my friends. I would like to acknowledge my friend Feifei Wei, who helped me with fluorescent microscopy setup. I would like to acknowl-

edge the collaborations with Professor Atul Parikhs group, Professor Ratnesh Lals group, Argonne National Lab APS beamline scientists Suresh Narayanan, Alec Sandy (sector 8), Christian M. Schleptz, and Evguenia Karapetrova (sector 33), NIST beamline scientist Chuck Majkrzak and Los Alamos National Lab beamline scientist Rex Hjelm for their help in all the research projects. This work was supported by the Office of Basic Energy Sciences, U.S. Dept. of Energy under DOE Grant number: DE-FG02-04ER46173.

I would like to thank my committee members Oleg Shpyrko, Terry Hwa, Judy Kim and Ratnesh Lal for taking their precious time serving on my thesis committee and also sharing with me their knowledge and mentorship.

I would like to thank all my group members, Hongyu Guo, David DiLena, Ben Holladay, Jingjin Song, Yi Yang for being supportive and making such a great group.

Finally, I would like to give my deepest appreciation to all my life-time friends who have been loving and supporting me throughout all these years, sharing tears and laughter, complaints and comforts. I would like to thank my mom and dad for their understanding and support for my pursuit so far from home, and apologize for not being able to take care of them. I would like to give my inexpressible appreciation to my dear husband, who has been sharing my passion and pain and made the bumpy road a poem with his caring and loving heart.

The texts of Chapter 3, 4, 5, 6, 7 are reprints of the materials as they appear in:

Yicong Ma, Sajal K. Ghosh, David A. DiLena, Sambhunath Bera, Laurence B. Lurio, Atul N. Parikh and Sunil K. Sinha. Cholesterol Partition and Condensing Effect in Phase Separated Ternary Mixture Lipid Multilayers, submitted (2015).

Yicong Ma, Sajal K. Ghosh, Sambhunath Bera, Zhang Jiang, Stephanie Tristram-Nagle, Laurence B. Lurio, and Sunil K. Sinha. Accurate Calibration and Control of Relative Humidity close to 100% by X-Raying a DOPC Multilayer. Physical

Chemistry Chemical Physics 17, no. 5 (January 21, 2015): 357076.

Yicong Ma, Sajal K. Ghosh, Sambhunath Bera, Zhang Jiang, Christian M. Schleptz, Evguenia Karapetrova, Laurence B. Lurio and Sunil K. Sinha. Anomalous Swelling Type II in Phase Separated Ternary mixture Lipid multilayers, submitted (2015).

Yicong Ma, Sajal K. Ghosh, David A. DiLena and Sunil K. Sinha. X-ray Studies of Domain Growth Kinetics, in preparation (2015).

Yicong Ma, Laura Connelly, Nirav Patel, Fernando Teran Arce, Ratnesh Lal and Sunil K. Sinha. AFM, Optical and Fluorescence imaging studies on phase separated lipid multilayer surface morphology, in preparation (2015).

VITA

2007	B. S. in Applied Physics, University of Science and Technology of China, Hefei, China
2009	M. S. in Physics, University of California, San Diego
2009	National School on Neutron and X-ray Scattering, Argonne National Laboratory, Chicago, Illinois
2015	Ph. D. in Physics, University of California, San Diego

PUBLICATIONS

Y. Ma, S.K. Ghosh, S. Bera, Z. Jiang, S. Tristram-Nagle, L.B. Lurio and S.K. Sinha., "Accurate calibration and control of relative humidity close to 100% by X-raying a DOPC multilayer", *Phys. Chem. Chem. Phys.*, 17, 3570 (2015).

F. Wei, D. Lu, R. Aguinaldo, **Y. Ma**, S.K. Sinha and Z. Liu, "Localized surface plasmon assisted contrast microscopy for ultrathin transparent specimens", *Appl. Phys. Lett.*, 105, 163102 (2014).

J. Carnis, W. Cha, J. Wingert, J. Kang, Z. Jiang, S. Song, M. Sikorski, A. Robert, C. Gutt, S.-W. Chen, Y. Dai, **Y. Ma**, H. Guo, L.B. Lurio, O. Shpyrko, S. Narayanan, M. Cui, I. Kosif, T. Emrick, T.P. Russell, H.C. Lee, C.-J. Yu, G. Grbel, S.K. Sinha and H. Kim, "Demonstration of Feasibility of X-Ray Free Electron Laser Studies of Dynamics of Nanoparticles in Entangled Polymer Melts", *Sci. Rep.*, 4, 6017 (2014).

L. Tayebi, **Y. Ma**, D. Vashaee, G. Chen, S.K. Sinha, and A.N. Parikh, "Long-range interlayer alignment of intralayer domains in stacked lipid bilayers", *Nat. Mater.*, 11, 1074 (2012).

C.M. DeCaro, J.D. Berry, L.B. Lurio, **Y. Ma**, G. Chen, S. Sinha, L. Tayebi, A.N. Parikh, Z. Jiang and A.R. Sandy, "Substrate suppression of thermal roughness in stacked supported bilayers", *Phys. Rev. E.*, 84, 041914 (2011).

ABSTRACT OF THE DISSERTATION

Structural Studies of Ternary Mixture Lipid Multilayer Systems and the Effect of High Hydration with X-ray Diffraction

by

Yicong Ma

Doctor of Philosophy in Physics

University of California, San Diego, 2015

Professor Sunil K. Sinha, Chair

Phase separated lipid mixtures systems have been of vast interest due to their possible relationship with lipid raft formation which is believed to facilitate certain protein activities and is associated with important biological processes. While a lipid multilayer system serve as an ideal system for high resolution structural studies with X-ray scattering techniques and has mostly been used to obtain an averaged result for pure or mixed systems (e.g., proteins, peptides in membrane), we have found that multilayer systems of phase separated lipid mixtures are actually able to give independent information regarding the coexisting phases due to the demonstrated columnar order of each of the two phases arising from the selective coupling in the third dimension. This finding opens up another dimension

of studies for phase separated lipid mixture systems.

In the first part of the dissertation, we describe a quantitative study of cholesterol partition and its condensing effect in phase separated ternary lipid mixtures using X-ray diffraction. The electron density profiles (EDP) of both phases were constructed and a newly invented EDP baseline-scaling model was used to extract the quantitative information of the cholesterol composition and lipid packing.

Next, the effect of close to 100% hydration on the different phases in the phase separated lipid mixture multilayer was studied. Firstly, we developed a high precision method for achieving and controlling hydration close to 100%, and an accurate method for calibrating the relative humidity using a $1,2-dioleoyl-sn-glycero-3-phosphocholine$ (DOPC) multilayer. With this setup, we discovered the novel phenomenon of anomalous swelling type II in the liquid disordered (L_d) phase of the phase separated mixed multilayer. This anomalous swelling is most likely due to the hydrophobic mismatch energy at the phase boundaries.

1 Introduction

Over the past decade, the role that lipids play in membrane organization has been a central focus of membrane biology and biophysics. As was first proposed by Simons and Ikonon[7] in 1997, rafts, localized regions of certain proteins and lipids, are associated with important biological processes such as adhesion, signaling and protein transport, etc. Lipid-driven lateral phase separation of multi-component liquid mixtures is thought to be a possible factor in the formation of rafts. A ternary mixture consists of saturated lipids, unsaturated lipids and cholesterol has been serving as a typical model system to study lipid-driven lateral separation of liquid phases, due to its advantages of measurable, controllable phase separation behavior. The phase diagrams of this system were mapped with the mixtures in the form of vesicles using fluorescence microscopy by Veatch and Keller [8, 9, 10, 11]. They also quantitatively measured tie-lines for certain compositions using NMR [12, 13, 14].

While X-rays have a long history with structural studies in smectic liquid crystals, they have become a powerful tool for lipid studies as well. Some of the most commonly used model systems for X-ray scattering experiments are lipid monolayers at the air-water interface, solid supported bilayers, free suspended lipid bilayers (also called black membranes), unilamellar lipid vesicles in solution, multilamellar lipid vesicles in solution, and solid supported multilayer systems in water vapor. Each modeled system is suitable for certain X-ray scattering techniques, for example, unilamellar vesicle solutions are usually used for small angle X-ray scattering (SAXS) while monolayers are usually used for grazing incidence diffraction (GID). Lipid multilayers are ideal systems for X-ray diffraction (XRD) measurements, for the smectic phase forms a one dimensional crystal similar to

the smectic liquid crystals. Not only have high resolution lipid structures for some typical lipid species been measured to angstrom accuracy [15, 16, 17, 1], but also mixtures of lipid and peptides or proteins has been explored to study the lipid-peptide or lipid-protein interaction. In the lipid-peptides/protein measurements, an averaged electron density profile (EDP) is obtained, such as works by Salditt [18, 19, 20], Huang [21, 22], Nagle and Tristram-Nagle [23, 24].

Interesting behavior occurs when phase separating ternary lipid mixtures are made into lipid multilayers. In our previous studies, we have found that the phase separated domains registers vertically through inter-lamellar coupling interaction and form columnar order across hundreds and thousands of bilayers [25]. The aligned domain size can reach tens to hundreds of microns in diameter laterally. Each phase generates a set of X-ray diffraction peaks based on its own periodicity and form factor, which allows independent EDP construction. This phenomenon was also characterized by confocal fluorescence microscopy and Atomic Force Microscopy. This new behavior in the third dimension opens up new possibilities for high precision measurements of individual phase structure, interlayer phase coupling, and also creates new problems associated with the phase boundaries, which will be discussed in detail in this dissertation.

This dissertation is structured the following way: Chapter 2 conducts a brief review of application of X-ray diffraction on lipid studies, EDP generation method used, and sample preparation methods. From Chapter 3, the main body of the dissertation starts. In Chapter 3 the study of cholesterol partition and condensing effect in both liquid ordered (L_o) and liquid disordered (L_d) phase of the phase separated ternary mixture multilayer is presented. Chapter 4 describes the method we developed to accurately control humidity close to 100% and calibration with DOPC multilayer. In Chapter 5, the described humidity control method is applied to measure the phase separated lipid multilayers. The anomalous swelling type II phenomenon is discovered close to full hydration, which leads to discussion of the phase boundary mismatch energy. Chapter 6 and 7 describes preliminary results of domain morphology and formation kinetic studies: AFM results of the system surface morphology are presented in Chapter 6; X-ray results of domain evolution

vs. time are presented in Chapter 7. Chapter 8 concludes the whole thesis.

2 The Application of X-ray diffraction to lipid multilayers

X-ray diffraction has been applied to studies of multi-lamellar lipid samples since the 1960s. It is by far the only technique that can measure lipid structures to sub-nanometer resolution. This chapter provides a brief background on X-ray diffraction, EDP reconstruction methods and the methods of sample preparation for lipid multilayer studies. The sections 2.1-2.3 are based on reference books [26, 27, 28].

2.1 Principles of X-ray diffraction

A scattering event is described by the wavevector transfer $\vec{q}$, defined as the difference between final and initial wavevectors,

$$\vec{q} = \vec{k_f} - \vec{k_l}. \tag{2.1}$$

In elastic scattering,

$$|\vec{k_f}| = |\vec{k_l}| = \frac{2\pi}{\lambda}, \tag{2.2}$$

where λ is the wavelength of the X-ray beam. In the kinematic approximation, the scattering amplitude $A(\vec{q})$ is the factor r_0 times the Fourier transform of the sample electron density distribution $\rho(\vec{r})$,

$$A(\vec{q}) = r_0 \int \rho(\vec{r}) \mathrm{e}^{-i\vec{q}\cdot\vec{r}}\, \mathrm{d}^3 r, \tag{2.3}$$

where $r_0 = \mathrm{e}^2/mc^2$, with e and m the charge and mass of an electron, c the speed of light, is the Thompson scattering length of the electron.

For a crystal structure, the lattice vectors can be written as follows,

$$\vec{R}_{uvw} = u \cdot \vec{a} + v \cdot \vec{b} + w \cdot \vec{c}, \qquad u, v, w \quad integers \tag{2.4}$$

where $\vec{a}, \vec{b}, \vec{c}$ are the primitive translational vectors of the lattice.

Therefore the electron density $\rho(\vec{r})$ can be written as the sum of the electron densities of the unit cell $\rho_{u.c.}(\vec{r})$, where $\rho_{u.c.}$ is the electron density in the origin unit cell,

$$\rho(\vec{r}) = \sum_{\vec{R_{uvw}}} \delta(\vec{r} - \vec{R}_{uvw})\rho(\vec{r}). \tag{2.5}$$

Plug equation 2.5 into equation 2.3, and using the properties of the δ distribution and the convolution theorem, the scattering amplitude can be re-written as the product of the structure factor $S(\vec{q})$ and the form factor $F(\vec{q})$,

$$A(\vec{q}) = S(\vec{q}) \cdot F(\vec{q}), \tag{2.6}$$

where

$$S(\vec{q}) = \sum_{\vec{R_{uvw}}} \mathrm{e}^{-i\vec{q}\cdot\vec{R}_{uvw}}, \tag{2.7}$$

$$F(\vec{q}) = \int_{V_{u.c.}} \rho_{u.c.}(\vec{r})\mathrm{e}^{-i\vec{q}\cdot\vec{r}}\,\mathrm{d}^3r, \tag{2.8}$$

where $V_{u.c.}$ is the origin unit cell volume. $F(\vec{q})$ is known as the form-factor for the electron density in the unit cell.

The observed scattering intensity is proportional to the modulus square of the scattering amplitude, thus

$$I(\vec{q}) \propto |S(\vec{q})|^2 \cdot |F(\vec{q})|^2 \tag{2.9}$$

The intensity also depends on several additional experimental factors, which we will discuss in the following section 2.2.

$|S(\vec{q})|^2$ reaches maxima when

$$e^{i\vec{q}\cdot\vec{R}_{uvw}} = 1 \tag{2.10}$$

which occurs when $q = q_{hkl}$ which are the set of vectors of the reciprocal lattice. For an infinite crystal, these maxima become a series of delta functions at the reciprocal lattice vectors.

Thus the diffraction intensity from a crystal can be derived:

$$I(\vec{q}) \propto \sum_{hkl} \delta(\vec{q} - \vec{q}_{hkl}) \cdot |\int_{V_{u.c.}} \rho_{u.c.}(\vec{r}) e^{-i\vec{q}\cdot\vec{r}} d^3r|^2 \tag{2.11}$$

This expression means that the diffraction intensity is given by the modulus square of the form factor sampled at discrete values fulfilling the Laue condition $\vec{q}_{hkl}$. The electron density can be expanded as a Fourier series with complex-valued coeffecients F_{hkl},

$$\rho_{u.c.}(\vec{r}) = \frac{1}{V} \sum_{h,k,l} F_{hkl} e^{i\vec{q}_{hkl}\cdot\vec{r}}, \tag{2.12}$$

where F_{hkl} is $F(\vec{q})$ evaluated at $\vec{q} = \vec{q}_{hkl}$,

$$F_{hkl} = |F_{hkl}| e^{i\phi_{hkl}}, \quad \phi_{hkl} \in [0, 2\pi]. \tag{2.13}$$

From the measured intensities, only the amplitudes of the form factor can be obtained on a relative scale, with the phase not directly accessible, as in the well-known phase problem in crystallography. In case of the lipid muli-lamellar systems, this phase problem can get simplified due to centrosymmetry, which will be discussed in detail in section 2.3. Also, the lipid multi-lamellar systems are one-dimensional crystals, so the dimensionality is reduced to 1 dimension, which makes the geometry of the diffraction measurements the same as the reflectivity measurements with respect to the lamellar plane. As a result (hkl) collapse to a single index n, which indicates the order of the reflection, with $q_z = q_n$.

One of our experimental setups is depicted in Figure 2.1, where a charge-couple device (CCD) camera is used as the detector during synchrotron measure-

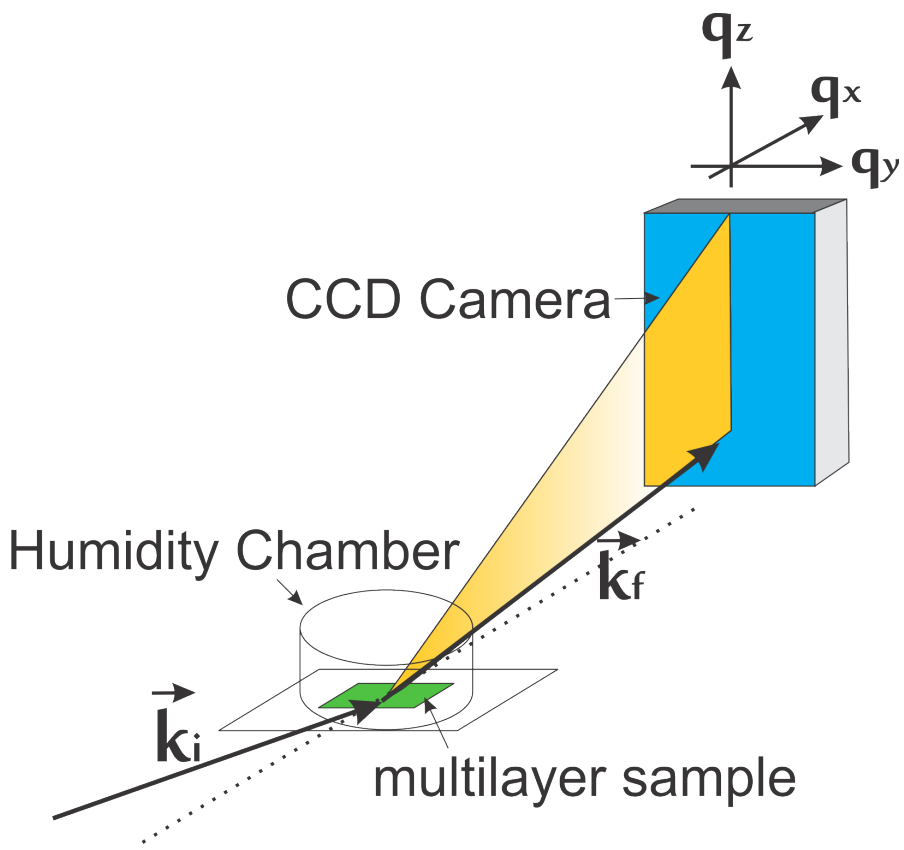

Figure 2.1: The experimental setup and geometry in our X-ray diffraction measurements with lipid multilayers.

ments. For in-house measurements, a point X-ray scintillator detector is used instead of the CCD, while the geometry stays the same.

2.2 Intensity correction factors

Before the integrated diffraction intensities can be used to get Fourier coefficients, the intensity has to be corrected with certain correction factors according to the exact experimental conditions. The correction factors for lipid multilayer diffraction include: instrumental factor, absorption correction, polarization correction, Lorentz factor and illumination correction, as follows [29, 30]

$$I_{hkl} = K \cdot C_{abs} \cdot C_{pol} \cdot C_L \cdot C_{ill} \cdot |F_{hkl}|^2. \tag{2.14}$$

Instrumental factor K is a constant decided by all global experimental parameters such as primary beam intensity, scattering volume and detector efficiency. For a fixed experimental setup, this factor should stay constant for all measurements.

Absorption correction takes into consideration of the X-ray absorption by the lipid film, sample chamber windows and air in the flight path. In the reflection geometry, the contributions from sample chamber windows and the air in the flight path are identical for all incident angles, so only absorption by the lipid film is considered. In reflectivity geometry, the beam path length though the sample is

$$I = \frac{2z}{\sin\theta} \tag{2.15}$$

where z is the sample thickness, θ is the incident angle. The absorption factor is

$$C_{abs} = \exp(-\mu l), \tag{2.16}$$

with μ the absorption coefficient for the lipid film at the X-ray wave length employed.

Because the absorption coefficient μ is proportional to the X-ray wavelength $lambda^3(1)$, with our in-house $8Kev$ tube source, the absorption is a big enough factor that should be taken into consideration. During data reduction, a film thickness of $3.5\mu m$ is used for calculation. In synchrotron experiments, a high energy X-ray beam of 20 Kev is used, and the contribution from absorption is significantly reduced, therefore not considered in the data reduction.

Polarization correction depends on the polarization of the beam. Synchrotron beams are linearly polarized therefore no polarization correction is needed for reflectivity measurement. On the other hand, the X-ray beam generated by a sealed tube source is unpolarized, and a polarization correction factor is calculated as follows [31]:

$$C_{pol} = \frac{1}{2}[1 + \cos^2(2\theta)]. \tag{2.17}$$

Within the small angle regime, this is a relatively small correction compared to all other correction factors.

Lorentz factor is the largest correction factor in our data reduction, and therefore affects the result the most. This factor takes consideration of the number of crystallites that contribute to the reflection, which depends on the structure of the sample [26, 29, 31, 32]:

$$C_L = \begin{cases} \dfrac{1}{\sin 2\theta} \propto q_z^{-1} & \text{reflection geometry} \\ \\ \dfrac{\cos\theta}{\sin^2 2\theta} \propto q^{-2} & \text{powder diffraction} \end{cases} \tag{2.18}$$

for small angles θ. For oriented stacks the correction is q_z^{-1} while for unoriented multi-lamellar vesicles it is q^{-2}. However, Li et al. [18] also suggested q_z^{-1} correction for oriented stacks from comparison with reflectivity fitting profile, which we adopted in our data correction in Chapter 4.

Illumination factor, also called the "footprint correction" in reflectivity data analysis, applies to the low angle data when not the whole beam illuminates the sample. This is an essential correction for data close to critical angle in reflectivity measurements. However, in our diffraction measurements the angles for which this is necessary are far lower than that for our first diffracted order, therefore this correction is omitted.

2.3 Construction of EDP

After the diffraction intensity is properly corrected with absorption factor and polarization factor, a sloping background is subtracted from the data, and Gaussians were fitted to the background subtracted diffraction peaks. The areas of the fitted Gaussians are considered the integrated peak intensities and the amplitudes of Fourier coefficients are calculated from these peaks to construct EDPs.

2.3.1 The phase problem

As was mentioned in section 2.1, there is a well-known problem in crystallography known as the phase problem. The amplitude of the Fourier coefficients can be obtained from the measured diffraction intensities; however the phase information is lost during the modulus square process.

In lipid multilayer systems, this problem still exists. However, it can be simplified due to the centrosymmetry of the modeled bilayer structure [28]. Through our selection of model lipid bilayers, a bilayer EDP is symmetric with respect to the bilayer midplane. Taking the bilayer midplane as $z = 0$, we have

$$\rho(z) = \rho(-z). \tag{2.19}$$

Using this symmetry, we can get

$$\begin{aligned} F(q_z) &= \int_{-d/2}^{+d/2} \rho(z) \mathrm{e}^{-iq_n z} \mathrm{d}^3 r \\ &= \int_{-d/2}^{+d/2} \rho(z)[\cos(q_z z) - i\sin(q_z z)]\mathrm{d}z \\ &= \int_{-d/2}^{+d/2} \rho(z)\cos(q_z z)\mathrm{d}z \end{aligned} \tag{2.20}$$

which shows that the F_{hkl} defined in Eq. 2.13 must be real, so the phase factor can only be ± 1 and the phase problem is reduced to a "sign problem" and $F_n = (\pm 1)|F_n|$.

The relative EDP (i.e. apart from a scaling factor) therefore can be calculated with (9)

$$\rho_{relative}(z) = \frac{2}{d} \sum_{n=-\infty}^{\infty} \nu_n \cdot |F_n| \cdot \cos\left(\frac{2\pi n z}{d}\right), \quad \nu(n) = \pm 1 \tag{2.21}$$

where d is the d-spacing of the bilayer, n is the Bragg peak order number, $F_n = \sqrt{nI_n}$ for q^{-1} Lorentz correction and $F_n = n\sqrt{I_n}$ for q^{-2} Lorentz correction. And the absolute EDP is [33, 16, 34]

$$\rho_{absolute}(z) = \rho_0 + \frac{1}{K}\rho_{relative}(z), \tag{2.22}$$

where $_0$ is the average density of lipid and K is the instrumental factor.

In order to get an accurate EDP, many methods have been developed to retrieve the phases for lipid multilayers. Among which, the most reliable and commonly used method, the swelling method, is the method we choose to use in our studies in this dissertation and will be discussed in detail in the next section.

2.3.2 The swelling method

The swelling method for lamellar phase was introduced more than 40 years ago [35, 36]. This method is based on the assumption that over a certain hydration range, the water thickness change does not change the structure of the lipid bilayer. Therefore, by taking the form factor of the EDP relative to water , the Fourier coefficients for different hydration conditions should fall on the same continuous and smooth curve [36, 37]. This is related to the sampling theorem known from signal theory [38, 39].

By plugging equation 2.21 into equation 2.20, we can get

$$F(q_z) = \sum_{n=-\infty}^{\infty} \nu_n |F_n| sinc\left(\frac{d}{2}q_z - n\pi\right), \tag{2.23}$$

where $sinc(x) = \sin x/x$. Define relative electron density

$$\rho_{(-)} = \rho(z) - \rho_w, \tag{2.24}$$

where ρ_w is the water density. Then the form factor would be

$$\begin{aligned} F_{(-)}(q_z) &= \int_{-d_0/2}^{+d_0/2} \rho_{(-)}(z)\cos(q_z z)\,\mathrm{d}z \\ &= \sum_{n=-\infty}^{\infty} \nu_n |F_n| sinc\left(\frac{d}{2}q_z - n\pi\right) - \rho_w d sinc\left(\frac{d}{2}\right) \\ &= \sum_{n=-\infty}^{\infty} \nu_n |F_{n(-)}| sinc\left(\frac{d}{2}q_z - n\pi\right), \end{aligned} \tag{2.25}$$

where d_0 is the lipid bilayer thickness without water, and

$$F_{n(-)}(q_n) = \begin{cases} F_0 - \rho_w d & n = 0 \\ F_n & n \neq 0 \end{cases} \tag{2.26}$$

While the water thickness changes with varying relative humidity (RH), the $|F_{n(-)}|$ are sampled at different values of d-spacings. Because the lipid bilayer structure stays the same, the continuous form factor $|F_{(-)}(q_z)|$ is sampled at slightly different q_z values on a continuous and smooth curve. The correct phase combination is decided by the requirement that the form factors fall on a continuous smooth curve.

2.4 Multilayer sample preparation methods

All the data presented in this thesis is obtained using the solid supported lipid multilayers, which are sometimes also called the oriented lipid bilayer stacks. The multilayers are prepared by deposition of lipids in organic solution on a smooth substrate, from which highly aligned bilayer stacks will self-assemble to form a one dimensional crystal multi-lamellar structure during the drying process, just like the smectic liquid crystals. By this spreading method [40], the number of bilayers can range from hundreds to thousands of bilayers, which can be controlled by tuning the concentration of the lipid solution. Figure 2.2 is a schematic drawing of the spreading method and a self-assembled multilayer stack.

The quality of the sample is directly related to 3 factors. First is the leveling of substrate. The substrate needs to be leveled carefully in order for the lipid multilayer to grow uniformly. Second factor is the choice of solvent. There are different combinations of solvents that people have experimented with in order to get the best quality samples. In principle, one should use a fast-evaporating solvent mixed with a slow-evaporating solvent for the optimum result. We have experimented with different combinations mentioned in the literature, and decided to follow the recipe developed by Li et al. [18] that uses 1 : 1 chloroform : TFE solution for our sample preparation. The solution concentration was around $6 \sim 8mg/ml$.

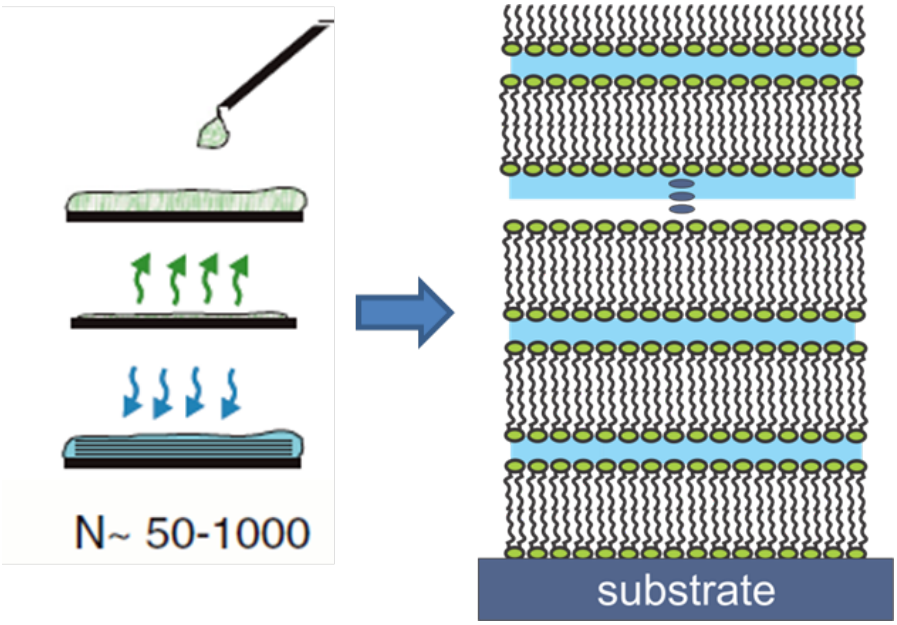

Figure 2.2: Spreading method (left) shows the lipid solution (green) was deposited by pipette, then solvent evaporates, the sample is re-hydrated with water (blue); schematics of multilayer stack (right) with water depicted as blue.

The last factor is the controlled venting. The evaporation speed of the solvent is closely related with how tightly the chamber is covered. Theoretically, the slower the evaporation, the better the sample is aligned; but on the other hand, if the evaporation is too slow, the sample could de-wet the substrate (especially on the silicon substrate) and form droplets instead of a uniform film. So a proper venting speed needs to be figured out empirically, to allow for optimum film self-assembly.

After the solution is deposited on the substrate, the samples are kept in the fume hood for $3 \sim 4$ hours to allow the bulk of the solvents to evaporate. After which, they were put into a weak vacuum ($\sim$ 70 Torr) for an additional 36 hours to evaporate any trace of solvent. A much stronger vacuum is not recommended, since the violent sucking would disrupt the lipid alignment. The elimination of any trace of solvent is essential for obtaining accurate d-spacings in hydration measurements (details in Chapters 4 and 5) because any leftover organic solvent attached to the headgroups will cause the interaction potential to deviate from that in a pure water environment. Therefore we prolonged the vacuum treatment

from that suggested in the literature from 24 hours to 36 hours to be sure.

After the vacuum treatment, the samples are transferred to heated humidity chambers for incubation for an additional 2 days. The humidity in the incubators are maintained at $\sim 98\%$ RH by placing saturated K_2SO_4 solution inside chamber, and whole chamber is heated to $50°C$. At $50°C$, samples are in the liquid disordered phase for both pure DOPC samples (used in Chapter 4) and the ternary mixture DOPC:DPPC:Cholesterol samples (used in Chapters 3 and 5), so that the samples would be homogenously mixed, aligned and equilibrated. After 2 days of incubation, the samples are cooled down to room temperature and ready to use.

One thing worth pointing out for ternary mixture samples is that the alignment process takes additional time after cooling down. The time required to finish alignment depends on both hydration conditions and also lipid mixture component. Generally, the higher the humidity, the faster the alignment will be; also the higher the cholesterol content, the faster the alignment. The alignment can take from several hours to months depending on the sample and the environment. For measurements of EDP for individual phases in the phase separated ternary mixture samples under partial hydration (such as the research described in Chapter 3), the samples have to be equilibrated for an additional several days at room temperature before measurement to give accurate Fourier coefficients.

3 Cholesterol Partition and Condensing Effect in Phase Separated Ternary Mixture Lipid Multilayers

3.1 Overview

The cholesterol partitioning and condensing effect in the liquid ordered (L_o) and liquid disordered (L_d) phases were systematically investigated for ternary mixture lipid multilayers consisting of 1:1 $1,2-dipalmitoyl-sn-glycero-3-phosphocholine(DPPC):1,2-dioleoyl-sn-glycero-3-phosphocholine(DOPC)$ with varying concentrations of cholesterol. X-ray lamellar diffraction was used to deduce the electron density profiles (EDP) of each phase. The cholesterol concentration in each phase was quantified by fitting of the EDP with a newly invented the Basic Lipid Profile (BLP) scaling method which minimizes the number of fitting parameters. The obtained cholesterol concentration in each phase vs. total cholesterol concentration in the sample increases linearly for both phases. The condensing effect of cholesterol in ternary lipid mixtures was evaluated in terms of phosphate-to-phosphate distances (PtP), which together with the estimated cholesterol concentration in each phase was converted into an average area per molecule. In addition, the cholesterol position was determined with precision and an increase of disorder in the lipid packing in the L_o phase was observed for total cholesterol

concentration of 20% and above.

3.2 Introduction

The "raft hypothesis" of biological membranes, first advanced now more than two decades ago, continues to invoke considerable debate and controversy [41, 7, 42, 43]. Its central claim has been that the lipid bilayer in cellular membranes is not an unstructured solvent; rather it is chemically textured, consisting of phase-separated domains enriched in saturated lipids, cholesterol, sphingolipids, and certain integral membrane proteins (e.g., GPI anchored proteins, SRC kinases). The hypothesis is based on the experimental observations that insoluble membrane fragments resistant to disruption by Triton X-100 at 4 $^{\circ}C$ are generally enriched in saturated lipids and cholesterol. This led to the proposition that these detergent-resistant membrane (DRM) fragments correspond to discrete raft domains within cell membranes. Because the physical state of the membrane is most likely altered in going from the physiological 37 $^{\circ}C$ to 4 $^{\circ}C$ used for detergent solubilization, the notion that DRM correspond to identifiable membrane domains in living cells has been largely discredited. However, extensive search over the past two decades for micro-domains has brought the question of how cholesterol mixes with membrane lipids into a sharp, renewed focus.

In the absence of cholesterol, essentially cylindrically-shaped phospholipids, saturated or unsaturated, adopt bilayer motif. Below their main phase transition temperature (T_m), the bilayers (typically composed of saturated lipids) exist in a gel (or solid) state characterized by tight packing of conformationally ordered, extended acyl chains. When the bilayer Tm is lower than the membrane temperature, such as for many unsaturated lipids, conformationally disordered chains in loose packing characterize two-dimensionally fluid bilayers. The non-ideal mixing of cholesterol, first reported in 1925 by Loathes, with saturated (or unsaturated) lipids profoundly influences molecular packing generating new phases: when added to high-melting saturated lipids, cholesterol perturbs the tight packing of the gel phase exerting fluidizing effect and transforming the gel phase, above a threshold

concentration, into a new liquid-ordered (L_o) phase. By contrast, cholesterol association with the fluid phase phospholipids above Tm produces a condensing effect by intercalating between loosely packed acyl tails and ordering neighboring chains as a consequence. In other words, cholesterol fluidizes the gel phase of saturated lipids and condenses fluid phases of unsaturated lipids, driving each toward an intermediate L_o phase characterized by intermediate packing density and membrane fluidity.

In multicomponent lipid mixtures, consisting of both saturated and unsaturated lipids, then, the phase behavior is determined by the balance of quantitative distribution of cholesterol between the two lipid types. In the work reported here, we report X-ray diffraction measurements in conjunction with a newly developed modeling procedure to extract detailed, quantitative information regarding cholesterol distribution in ternary mixtures containing a saturated and an unsaturated lipid in a hydration-controlled smectic lipid multilayer. We find that cholesterol associates in greater concentrations with the saturated phospholipid stabilizing L_o phase within the Ld surrounding within the three-dimensionally phase.

Phase diagrams of ternary lipid mixtures consisting of saturated lipids, unsaturated lipids and cholesterol have been studied systematically by Veatch and Keller [9, 10, 11, 13] mainly using fluorescence microscopy. There are also been studies with NMR to determine tie lines in the phase diagrams [12], as well as X-ray scattering studies in attempts to determine the composition of coexisting phases [44].

In these cholesterol-induced phase separation processes, the role of condensing effect due to cholesterol remains unclear. Although the condensing effect of cholesterol in binary systems has been studied systematically [45, 46], no systematic and quantitative studies have been carried out to measure the condensing effect in ternary systems, nor its relation to cholesterol-induced phase separation. In order to do that, we carried out X-ray diffraction studies on supported multilayer of lipid mixtures consisting of saturated, unsaturated lipid and cholesterol, and used quantitative modeling of the electron density profiles (EDP) to extract such information.

X-ray and neutron lamellar diffraction methods applied to lipid multilayers have been well-established and demonstrated as powerful techniques to quantitatively study the detailed lipid bilayer structures. Using these methods, cholesterol packing structures with several different kinds of lipids have been studied [47, 48]. Diffraction data usually are converted to electron density profiles, and decomposed into different chemical group densities with modeling [49], sometimes with the help of molecular simulations [50, 51]. In this study of mixed lipid multilayer systems with cholesterol, we propose a simple yet effective modeling scheme which helps to quantify the composition and to localize the cholesterol positional distribution with angstrom accuracy.

3.3 Materials and Methods

$1,2-dipalmitoyl-sn-glycero-3-phosphocholine(DPPC)$ and $1,2-dioleoyl-sn-glycero-3-phosphocholine(DOPC)$ solutions were purchased from Avanti Polar Lipids, Inc. (Alabaster, AL, USA) with accurate concentrations of the lipids specified. Cholesterol was purchased from Sigma Chemicals (St. Louis, MO, USA). All the purchased chemicals were used without further purification. The phospholipids and cholesterol were mixed in the desired proportions and dissolved in a chloroform and Tetrafluoroethylene (TFE) 1:1 mixture solvent [18], to yield a final concentration 8 mg/mL.

Silicon substrates, cut to 17 mm by 20 mm wafers, were first sonicated for 15 min in methanol followed by another 15 min in deionized water (miliQ, $18M\cdot Ohm\cdot cm^{-1}$). Substrates were then nitrogen-dried, and exposed to short-wavelength UV radiation for $\sim$ 15 min to make the surface hydrophilic. The prepared substrates were then placed on a carefully leveled platform for lipid deposition. 150 μL of lipid solution were deposited on each substrate and covered by a large Petri dish for slow evaporation in the fume hood. After $3 \sim 4$ hrs, the samples were transferred to a vacuum chamber for 36 hrs to remove remaining traces of solvent. After removing from the vacuum, the samples were placed in humidity chambers maintained at 96% relative humidity (RH) at 50 $^{\circ}C$ and incubated for 48 hrs.

Subsequently, the samples are cooled to room temperature at the ambient rate. Depending on the lipid composition, samples equilibrate to a uniform multibilayer or phase separate into two co-existing lamellar phases (a DPPC rich L_o phase and a DOPC rich L_d phase). Consistent with our earlier findings, equilibration of phase separating lipid mixtures involves thickness-dependent lateral coarsening of the domains and interlayer domain registration producing a columnar mesophase [25]. Depending on the humidity in the chamber and sample thickness, domain equilibration process above takes one to several days to complete. The diffraction measurements were carried out after the registering process was mostly complete.

Although elaborate, the procedure above ensures reproducibility producing high quality of samples as reflected by the observations of up to the 9th order of diffraction peaks with in-house X-ray tube source. A sample set consisting of a fixed 1:1 DPPC: DOPC containing systematically varied molar fraction cholesterol (0%, 10%, 16%, 20%, 25%, 30%) were prepared (e.g., for the 16% cholesterol sample, the composition is 42% : 42% : 16% DPPC : DOPC : cholesterol in molar ratio) and characterized. This cholesterol molar fraction will be denoted with Φ_c in later uses. All samples were measured at room temperature ($\sim 25°C$), except for the sample containing 30% cholesterol, which was measured at 11 $°C$ due to a much lower phase transition temperature of this specific mixture ($\sim 20°C$) , as shown by Mills et al. [52].

3.4 Results

3.4.1 X-ray diffraction

X-ray diffraction measurements were carried out using an in-house CuK_α tube spectrometer with wavelength 1.54 Å operating in the horizontal plane. Beam dimensions were set to be 0.2 mm in the horizontal direction and wide open (10 mm) in the vertical direction. Our custom designed humidity chamber [53], which can control RH to 0.01% accuracy close to full hydration when used as a high humidity control chamber was used for the measurements. The chamber was loaded with a saturated salt solution to keep the samples at a fixed partial hydration at

room temperature ($\sim 25°C$) during measurements.

In comparison with the synchrotron X-ray diffraction data obtained typically for membrane samples consisting of multi-lamellar vesicles (with highest order n = 4) [44], the diffraction data we collected in house were at significantly better quality and extended to larger q (with highest order n = 9). This is because our sample preparation procedure (see above) produces multilayer samples consisting of several hundreds of bilayers with high-level of inter-layer registration of each of the two co-existing phases. Polarization corrections and absorption corrections were applied to the data collected. The lineshapes of multilayer diffraction peaks are often fitted by expressions due to Caille [54]. However, we did not observe Caille line shapes here, probably due to the partial hydration condition, which result in suppressed interlayer fluctuations. Thus, the diffraction peaks were fitted to Gaussians after subtracting a sloping background. The integrated intensity I_n of $n-th$ order peaks were then used to calculate the electron density profiles with the following equation [33]:

$$\rho_{relative}(z) = \frac{2}{d}\sum_{n}\nu(n)n\sqrt{I_n}cos\left(\frac{2\pi nz}{d}\right), \tag{3.1}$$

where d is the lamellar spacing, $\nu(n)$ is the phase factor for the nth order reflection, and the factor n arises from the Lorentz correction of q_z^{-2} applied to the raw intensities I_n, as suggested by Li et al. [18]. Because of the mirror symmetry of the bilayers in the z direction, it can be shown that the phase factors can only be ± 1. For each phase, intensities of all diffraction orders are normalized by the sum of all peak intensities in that phase to account for the full beam intensity normalization correction. This correction is essential before the electron density profile is normalized to an absolute scale using the method described in the next section.

3.4.2 Absolute electron density profile generation

In order to extract quantitative information of cholesterol content from the electron density profiles, correct phase choices for every diffraction order and

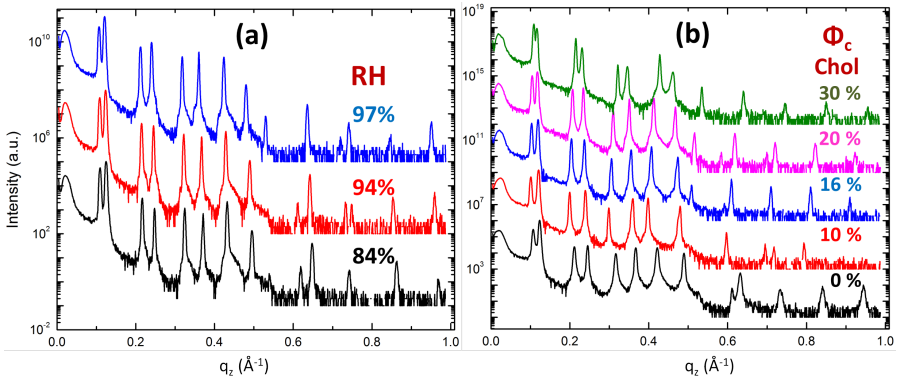

Figure 3.1: The diffraction patterns for (a) 0% cholesterol sample at different RH; (b) samples with different cholesterol content at 97% RH.

proper normalization to an absolute scale are both required.

Phasing

Lipid samples with 0%, 16%, 20%, 25% cholesterol Φ_c were measured under 3 different hydrations (with saturated salt solution as reservoir): 84% (KCl), 94% (K_2NO_3) and 97% (K_2SO_4) RH so that the swelling method [35, 55] could be used to determine the phases. A representative set of diffraction patterns of 0% cholesterol sample measured at room temperature under different hydrations is shown in Figure 3.1 (a). An example of phasing diagrams for the same sample is shown in Figure 3.2. The determined choices for the phase factors of the DPPC-rich phase at 97% RH were [-1,-1,1,-1,-1,-1,-1,-1,-1] for the 0% cholesterol sample, and [-1, -1, 1, -1, 1, -1, -1, -1, -1] for the 16%, 20%, 25% cholesterol samples. Note that the only difference between these two sets of phases is the sign reversal for the 5th order peak. This sign reversal is further supported by the fact that the 5th order peak was missing in the 10% cholesterol sample. For the DOPC-rich phase, 4 6 orders of peaks were observed, and the phase factor choices were [-1, -1, 1, -1, 1, -1] for all. The diffraction patterns for samples with different cholesterol concentrations at 97% RH are shown in Figure 3.1 (b). Correct phase choices are crucial for the detailed data analysis needed to accurately estimate cholesterol content, described in the next section 3.3 below.

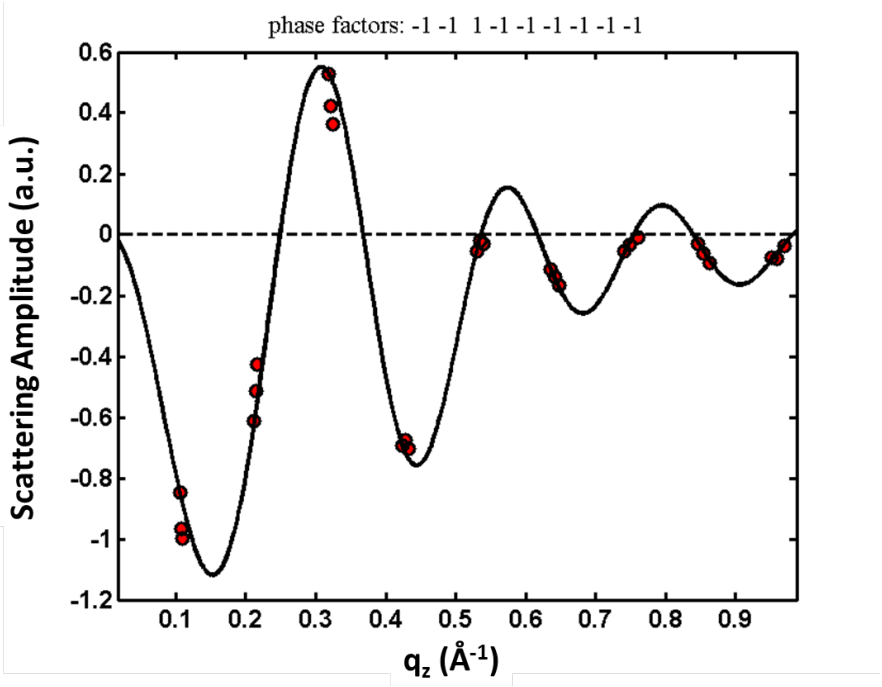

Figure 3.2: An example of a phasing diagram for the data in Figure 3.1(a). Diffraction by a sample was measured at 3 different RHs so as to obtain the scattering amplitudes at a series of different lamellar spacings. The scattering amplitudes are either positive or negative. The phases are chosen such that the continuous form factor (solid curve) constructed from one set of data at one lamellar spacing goes through all other sets of data.

Scaling

In order to normalize the relative electron density profiles to an absolute scale, the instrumental factor needs to be determined. The absolute density profile $\rho_{absolute}(z)$ is given by King, Jacob and White [33, 16, 34]:

$$\rho_{relative}(z) = \rho_0 + \frac{1}{K}\rho_{relative}(z) \tag{3.2}$$

where both the average density of the lipid ρ_0 and the instrumental factor K need to be determined. We obtain these two factors by comparing the EDP of our DPPC-rich phase from the 0% cholesterol sample to the EDP of the pure DPPC obtained by Wiener and Nagle [3]. As shown in Figure 3.3 (a), the EDPs are almost identical in the head group region and around the CH3 groups. Furthermore, our EDP can resolve the plateau region of the DPPC tails, which we attribute to the higher orders of the diffraction peaks. The disagreement in the water region is most likely due to the differences in hydration: our data are measured under partial hydration while Weiner and Nagle measured vesicles in excess water. While multilayer samples we investigated have less than 8Å of water, vesicles in Weiner and Nagle study have 25Å, which then explains the presence of better resolved water region in their profile.

The rest of the data were all normalized with the same two factors since the average lipid densities were similar and experimental conditions were identical. Comparisons of the EDPs for the different phases from samples with 0%, 16%, 25% cholesterol are shown in Figure 3.3 (b) and (c). Even a casual inspection of the data reveals that the increase of the electron density at the lipid chain region due to the added cholesterol in the DPPC rich phase is more than in the DOPC rich phase, which we quantify in the next section.

3.4.3 A new method of quantifying cholesterol content by fitting EDPs

There are several methods in the literature regarding decomposion of the EDP into contributions from individual components. Two popular ones namely

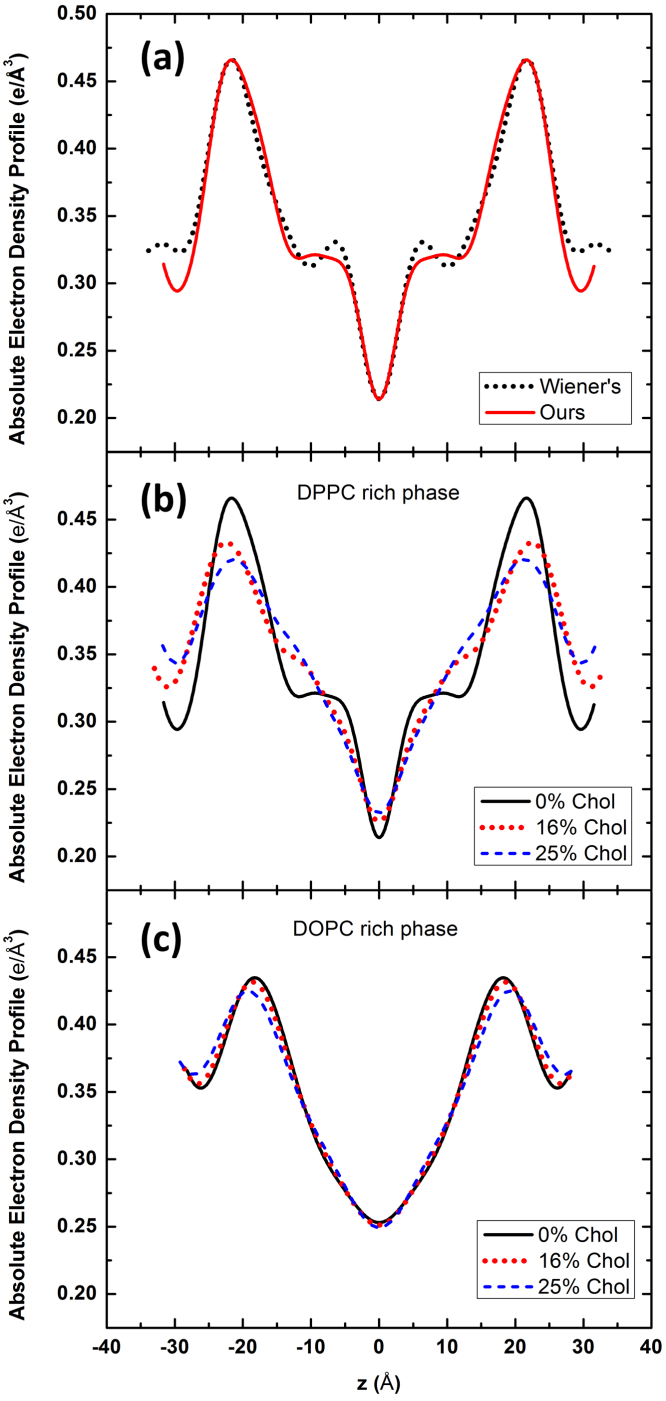

Figure 3.3: (a) Normalizing our EDP for the DPPC-rich phase of the sample with 0% cholesterol to Wiener and Nagles absolute EDP for DPPC [3]. (b) & (c) comparison of the normalized EDPs for the samples with 0%, 16%, 25% cholesterol Φ_c from the DPPC-rich phase and the DOPC-rich phase respectively on an absolute scale.

1G and 2G models, fit either one or two Gaussian functions to the headgroup region respectively, in addition to one Gaussian fitting of the methyl groups. Others such as 4S and 5S strip models, interpret the profiles in terms of boxes [3]. In our case, one could in principle fit every EDP with a 2G model plus an additional Gaussian for cholesterol, for example, to obtain a set of parameters for the headgroup, tail group and cholesterol density. The parameters, so derived, can then be compared across the entire sample set consisting of lipid mixtures with systematically varied cholesterol content. Applying this approach, however, would lead to over parameterization: Each EDP fitted with 4 Gaussians (2 for headgroup of the asymmetric shape, 1 for the methyl group and 1 for cholesterol) plus a constant baseline, will generate 12 independent parameters (the position for methyl group is taken as 0). Fitting the EDP to such heavily parameterized model will obviously result in broad ranges of fitting parameters losing unique solution rendering the analysis less meaningful. In order to circumvent this issue and find a minimal set of parameters, which adequately quantifies the change in the cholesterol content, we have developed a new fitting method. We call it the Basic Lipid Profile (BLP) scaling method. The essence of this method is to eliminate redundant parameters by keeping the basic lipid structure proportions fixed.

Basic Lipid Profile generation based on modified 2G model

After cooling down to room temperature, the sample with 0% cholesterol phase separates into a DPPC-rich gel phase and a DOPC-rich fluid phase. Our method is based on generating a Basic Lipid Profile (BLP) by fitting the EDPs of the respective phases of the sample with 0% cholesterol. One can use conventional methods for this fitting, either 1G or 2G model, depending on the headgroup shape. In our case, we used the 2G model with one baseline. The electron density profile is decomposed into 2 Gaussians for the headgroup (G_1, G_2), 1 Gaussian for the methyl group (G_3), with one constant baseline C_B:

$$\rho_0(z) = C_B + \sum_{n=1}^{3} G_n, \tag{3.3}$$

where $G_n = a_n exp\left(-\frac{(z-b_n)^2}{2c_n^2}\right), n = 1,2,3$. Note that a_3 is negative. The fitting parameters are listed in Table 3.1. The fits for the DPPC-rich and DOPC-rich phases are shown in Figure 3.4 (a) top figure and 3.4 (b) top figure respectively.

Scaling of BLP - minimizing the fitting parameters

With the fitted parameters for the BLPs for each of the phases, we can start fitting the EDPs for samples with added cholesterol. We use 2 scaling parameters for the BLP: the overall amplitude scaling factor C_1, and Gaussian width scaling factor C_2. The scaling factor for the Gaussian position was fixed to $\frac{D_{hh}}{D_{hh}^0}$, where D_{hh} is the phosphate-to-phosphate distance (PtP) for the sample with added cholesterol (determined as the distance between two maximums on the EDP), and D_{hh}^0 is the PtP for the 0% cholesterol sample (BLP sample). The functional form for the scaled BLP is as follows (compare with Eq.3):

$$\rho_{BLP}(z) = C_1 \left[\frac{d_0}{d} C_B + \frac{1}{C_2} \sum_{n=1}^{3} a_n exp\left(-\frac{\left(z - \frac{D_{hh}}{D_{hh}^0} b_n\right)^2}{2(C_2 c_n)^2} \right) \right] \tag{3.4}$$

The $\frac{d_0}{d}$ factor in the first term and the $\frac{1}{C_2}$ factor in the second term ensure that the integrated area under the density profile represented by the expression inside the square bracket is constant. Physically, C_1 models the overall electron density change due to looser or denser packing; while C_2 models the smearing of electron density profile due to roughness, disorder, or fluctuations.

After the scaled BLP is constructed, we can write out the equation for fitting the EDPs with added cholesterol as:

$$\rho(z) = \rho_{BLP}(z) + \Delta\rho_{Chol} \tag{3.5}$$

where $\Delta\rho_{Chol} = a_{Chol} exp\left(-\frac{(z-b_{Chol})^2}{2c_{Chol}^2}\right)$, is the Gaussian representing the increased electron density due to the added cholesterol.

Table 3.1: Gaussian fitting results of gel phase and fluid phase EDP with 0% cholesterol.

		Constant Baseline	Tail Region	Head Region I	Head Region II
Gel Phase (DPPC rich)	Baseline ($e/\text{Å}^3$)	0.319 ± 0.002	-	-	-
	Height ($e/\text{Å}^3$)	-	-0.106 ± 0.002	0.085 ± 0.005	0.130 ± 0.005
	Width (Å)	-	2.3 ± 0.1	2.3 ± 0.1	2.3 ± 0.1
	Position (Å)	-	-	18.1 ± 0.3	22.5 ± 0.3
Fluid Phase (DOPC rich)	Baseline ($e/\text{Å}^3$)	0.289 ± 0.002	-	-	
	Height ($e/\text{Å}^3$)	-	-0.036 ± 0.002	0.062 ± 0.005	0.114 ± 0.005
	Width (Å)	-	3.8 ± 0.1	3.8 ± 0.1	4.0 ± 0.1
	Position (Å)	-	-	14.6 ± 0.3	19.7 ± 0.3

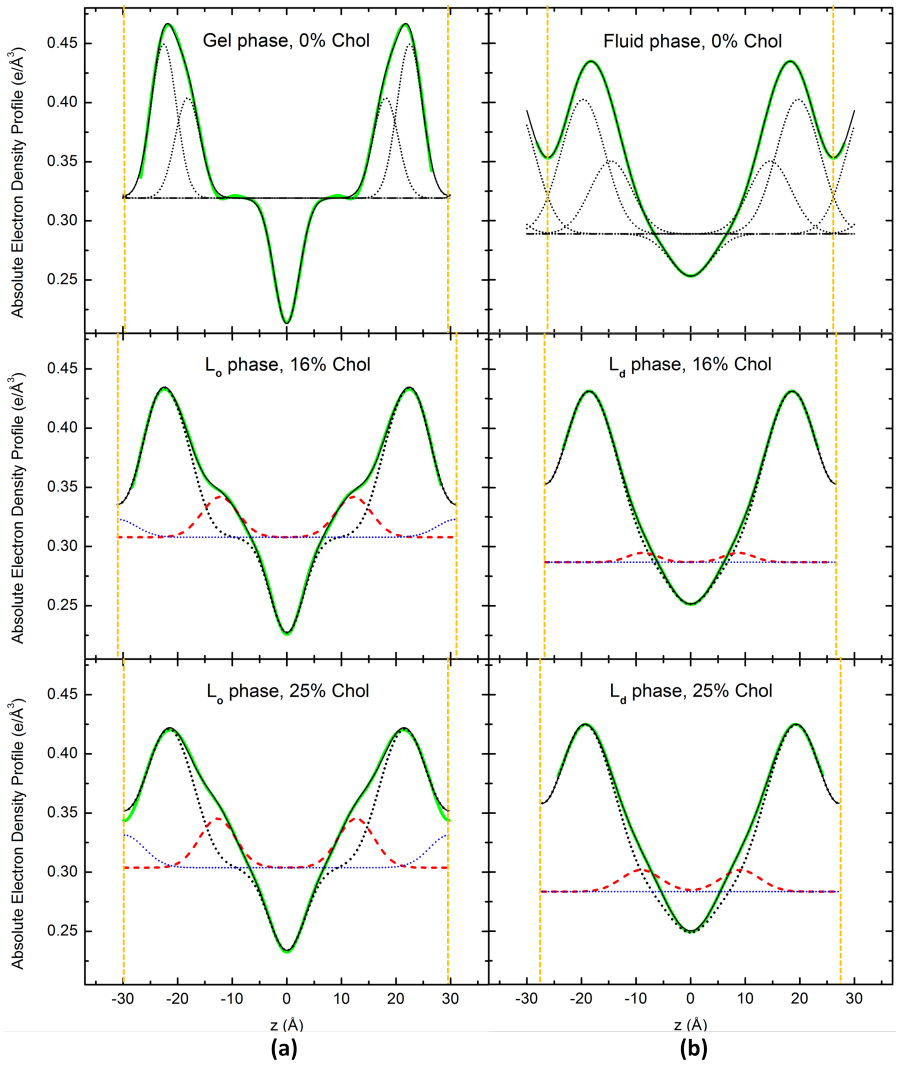

Figure 3.4: The fitting of 0%, 16%, 25% cholesterol sample EDPs of the DPPC-rich phase (a) and the DOPC-rich phase (b) using the BLP scaling method. The pair of yellow vertical dotted lines marks one period of the unit cell, namely the d-spacing. The solid green line shows the EDP generated from diffraction measurements. The solid black line is the fitted curve. The top figures are the BLP fitting of the 0% cholesterol sample using the 2G model. The Gaussian components and the constant baseline are represented by the dotted black lines. The middle and bottom figures are the fittings of cholesterol content for the 16% and 25% cholesterol samples with the scaled BLP obtained from the 0% cholesterol EDP fitting. The black dotted lines are the BLP scaled from (a). The red dash lines are Gaussian fits of the electron density increase due to added cholesterol. The blue dotted lines represent additional water smear into the outer headgroups due to the change of lipid packing.

The EDPs of samples with added cholesterol are thus fitted with 2 scaling factors C_1, C_2, plus 3 parameters for $\Delta\rho_{Chol}$, a total of 5 free parameters.

This result of the fitting allows us to quantitatively compare the EDPs of the samples with added cholesterol to the ones without cholesterol. The fittings in the middle and lower figures of Figure 3.4 show the EDPs of each phase derive from the samples with 16% and 25% cholesterol respectively. The green solid lines are the Fourier constructed EDPs from diffraction measurements, the dotted black lines are the scaled BLPs, the red dashed lines are Gaussian fits of the electron density increase due to added cholesterol, and the black solid lines are the total fitted curves. Blue dotted line marks the additional density of water at the outer side of the headgroup added due to the change in lipid packing, and our results are not sensitive to this parameter since the cholesterol sits at the tailgroup side. The fitted results for all cholesterol concentrations are listed in Table 3.2.

3.4.4 Distribution of cholesterol between saturated and unsaturated lipids

The increased electron densities resulting from the fitting are due to the ring structures in the cholesterol molecule. This increase in terms of the electron density per unit area $\Delta\delta$ is calculated as the integrated area of $\Delta\rho_{Chol}$,

$$\Delta\delta = \int_{-d/2}^{d/2} \Delta\rho_{Chol} dz \tag{3.6}$$

The plot of $\Delta\delta$ vs. initial cholesterol concentration Φ_c is plotted in Figure 3.5 (a). Note that this is not the integrated electron density of cholesterol molecules, but rather the averaged electron density difference at the chain region after adding cholesterol. In order to determine how the cholesterol partitions between the two, DOPC and DPPC, lipids, we carried out the following calculation. Assuming that the electron density differences between the cholesterol ring structure and the lipid chain region are roughly the same for the L_o and L_d phases, the amount of the cholesterol in each phase would be proportional to the averaged difference $\Delta\delta$ multiplied by the phase volume percentage ϕ. Thus, the percentage

Table 3.2: Gaussian fitting results of gel phase and fluid phase EDP with 0% cholesterol.

	Φ_c (Initial Chol %)	C_1 ($\pm$0.005)	C_2 ($\pm$0.01)	Chol Gaussian Height ($e/$Å^3)($\pm 0.001 e/$Å^3)	Chol Gaussian Width (Å)($\pm$0.1Å)	Chol Gaussian Position (Å)($\pm$0.5Å)
	10%	1.038	1.36	0.032	3.0	10.2
	16%	1.008	1.33	0.034	3.3	12.2
L_o phase	20%	0.993	1.33	0.039	3.2	11.6
(DPPC rich)	25%	0.956	1.45	0.041	3.3	12.7
	30%	0.947	1.48	0.046	3.3	12.7
	10%	1.000	1.00	0	-	-
	16%	1.010	1.02	0.008	2.8	8.8
L_d phase	20%	1.013	1.03	0.014	3.0	9.1
(DOPC rich)	25%	1.021	1.06	0.018	3.5	9.1
	30%	1.008	1.07	0.023	3.8	9.2

Table 3.3: Linear fitting results of x.

	a (Intercept)	b (Slope)
x_{L_o}	0.22 ± 0.02	0.5 ± 0.1
x_{L_d}	-0.11 ± 0.01	1.1 ± 0.1

of cholesterol partitioned into L_o phase is

$$\vartheta_{L_o} = \frac{\Delta\delta_{L_o} \times \phi_{L_o}}{\Delta\delta_{L_o} \times \phi_{L_o} + \Delta\delta_{L_d} \times \phi_{L_d}}. \tag{3.7}$$

While for the L_d phase, the fractional cholesterol content is the reminder of the total:

$$\vartheta_{L_d} = 1 - \vartheta_{L_o}. \tag{3.8}$$

The plot for the cholesterol partition is shown in Figure 3.5 (b), with ϕ in the insert. The ϕ was taken as proportional to the ratio of the sum of the integrated intensities of diffraction peaks in each phase. Here we measured integrated intensity ratios for Φ_c of 16% and 25%, and linearly interpolated for the remaining concentrations.

The concentration of cholesterol in L_o and L_d phase after phase separation would be

$$x_{L_o/L_d} = \frac{\vartheta_{L_o/L_d} \times \Phi_c}{\phi_{L_o/L_d}}. \tag{3.9}$$

And the plot is shown in Figure 3.5 (c) with linear fits. The fitting results are in Table 3.3.

Note that this result indicates that the cholesterol only start to partition into the L_d phase when Φ_c is greater than 10%, below which almost all the cholesterol segregates into the L_o phase.

The distribution coefficient K, defined as the ratio of concentration of the two phases, is plotted in Figure 3.5 (d).

$$K = \frac{x_{L_o}}{x_{L_d}}. \tag{3.10}$$

If x is linear with respect to Φ_c, then

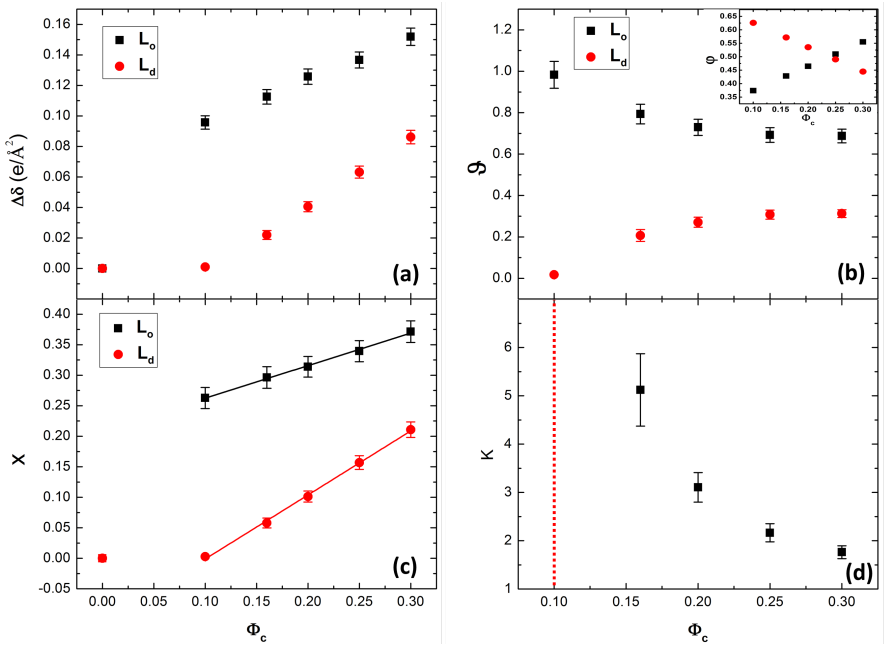

Figure 3.5: (a) Plots of $\Delta delta$ vs. Φ_c; (b) cholesterol partition ϑ vs. Φ_c with phase volume fraction ϕ as inset; (c) cholesterol concentration x fitted with linear functions for each phase; (d) distribution coefficient K vs. Φ_c.

$$K = \frac{a_1 + b_1\Phi_c}{a_2 + b_2\Phi_c}. \tag{3.11}$$

Previously, Veatch et al. [14] have mapped out a phase diagram for the DOPC, DPPC with cholesterol using NMR and measured the two tie lines across 1:1 DOPC:DPPC with 15% and 20% cholesterol at $25°C$. Comparing our result of 16% and 20% to these values, we find an excellent agreement, within experimental error, between the cholesterol concentration in each phase estimated from our fitting and their NMR results.

3.4.5 Condensing effect

Figure 3.6 (a) shows the measured PtP vs. Φ_c plot. We can see that above 10% Φ_c where the DPPC-rich phase is in the L_o phase instead of the gel phase, the added cholesterol increases the bilayer thickness of the L_d phase, while it decreases the bilayer thickness of the L_o phase. This is known as the cholesterol condensing effect, and in this ternary mixture is consistent with the theory and results by

Hung et al. on binary systems [45], who showed that the hydrophobic regions of lipids tend to match the hydrophobic thickness of the cholesterol. In our case, the hydrophobic thickness of cholesterol is intermediate between the chain lengths of the DPPC and the DOPC, and therefore the bilayers in the L_o phase are thinned and the bilayers in the L_d phase are thickened after adding cholesterol.

We can also calculate the average molecular area in each phase according to Hung et al.:

$$A_{av} = xA_{cho} + (1-x)A_{av.pc}, \tag{3.12}$$

where x is the cholesterol concentration in that phase, $A_{av.pc}$ is the average cross section area of phospholipid in that phase, calculated by

$$A_{av.pc} = \frac{2V_c}{PtP - 10}. \tag{3.13}$$

V_c is the chain volume of the lipid, 10Å is the twice the length of the glycerol region. A_{av} is plotted in Figure 3.6 (c). For V_c, we choose to use the chain volume of the majority lipid in the particular phase under consideration.

Also the PtP and A_{av} can be plotted vs. x, the concentration of cholesterol in each phase after phase separation (Figure 3.6 (b,d)), which can be better compared to the binary system results [45]. We can see that the change of PtP in the L_o phase is more than that of the L_d phase, which agrees well with the results by Hung et al. of binary systems with saturated (DMPC) and unsaturated (DOPC) lipids. Note that here the DPPC has longer chain length than the DMPC, which leads to a thinning effect caused by the cholesterol rather than a thickening effect for the DMPC. The average molecular area of the L_o phase slightly goes up, while that of the L_d phase goes down by a much larger amount. This is mainly due to a larger difference in molecular area between the DOPC and cholesterol than that of the DPPC and cholesterol.

3.4.6 Cholesterol position

The fitting localizes the cholesterol packing distribution with great precision. Figure 3.7 shows the maximum position of fitted cholesterol distribution for

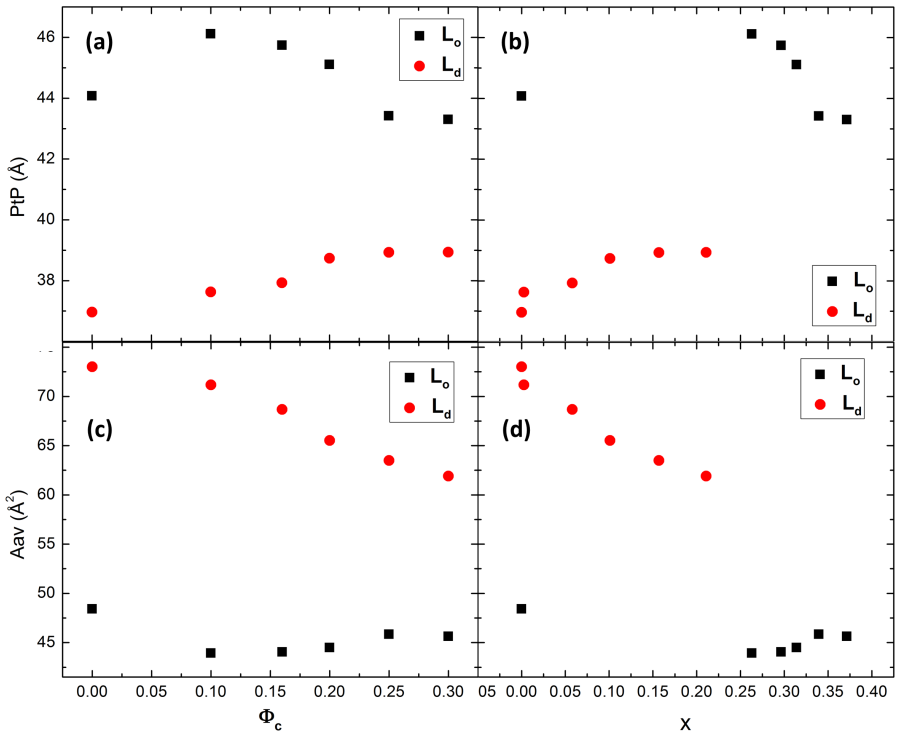

Figure 3.6: (a) PtP vs. Φ_c, the total cholesterol content in the sample. (b) PtP vs. x, the cholesterol concentration in the respective phase. (c) the average molecular area vs. Φ_c. (d) the average molecular area vs. x. The error bars are smaller than the symbol sizes.

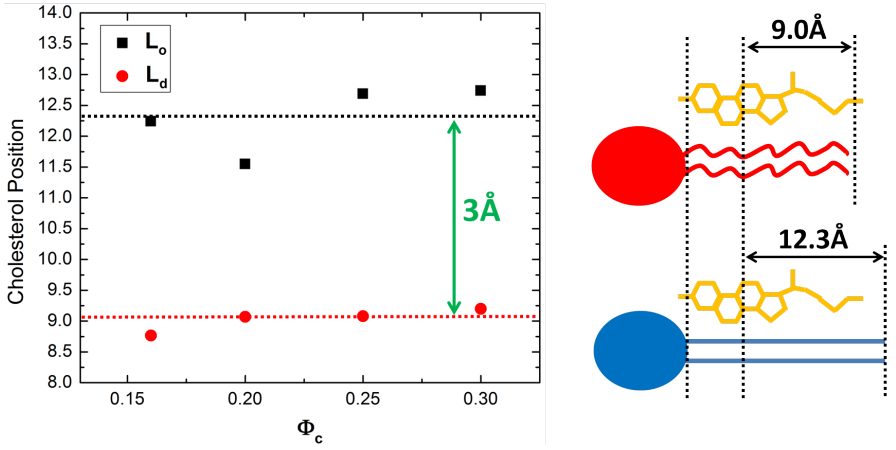

Figure 3.7: Cholesterol position plot agrees with the cholesterol packing along the hydrophobic surface of lipids, as shown in the cartoon on the right.

both the L_o and the L_d phase: the cholesterol ring structure are mostly concentrated at 12.3Å for the L_o phase and 9Å for the L_d phase from the bilayer center. While the difference of PtP between the two phases is around $2 \sim 4$Å, if one aligns the electron density profiles of the two with the headgroups, one can see that the cholesterol sits roughly at the same position, as shown in the cartoon on the right side in Figure 3.7. This result agrees with the previous study of McIntosh on cholesterol packing of saturated lipids with different chain lengths [46]. Several other studies [47, 48, 56] have also indicated that the hydroxyl group of cholesterol must be in very close proximity to the carbonyl group of the lipids.

3.4.7 Change of lipid packing

The change of packing is reflected in the two scaling factors: C_1 which reflects the overall density change in the lipid packing; while C_2 reflects the smearing of the EDP, which might be due to increased fluctuation or roughness. C_2 will be referred to as the disorder parameter.

From the plot showing the variation of C_1 with initial cholesterol content in Figure 3.8 (a), we can see that the overall packing density decreases for the L_o phase, while it increases for the L_d phase as a function of Φ_c. This is mostly due to the change of PtP: in the DPPC-rich L_o phase with a decreased bilayer

thickness, the lipids are squeezed so that they have a lower packing density per unit area; on the other hand, in the DOPC-rich L_d phase which has an increased bilayer thickness, the lipids are stretched so the packing density increases.

The plot showing the variation of C_2 with initial cholesterol content Φ_c in Figure 3.8 (b) gives additional information. The smearing of the EDP while maintaining its integrated area means increased fluctuation or roughness (disorder). It has been known since Levine and Wilkins [57] that the EDPs of cholesterol-containing membranes are independent of the hydration condition, which means that the cholesterol will stiffen the bilayers and thus suppress the fluctuations. Therefore, this smearing of EDP which we observe must come from the increased roughness resulted from the disordering effect of adding cholesterol. While $C_2 = 1$ for the cholesterol free samples, after adding cholesterol, the averaged lipid bilayer roughness for the DOPC-rich L_d phase changes very little, while the DPPC-rich L_o phase increases by more than 30% for $\Phi_c = 10 \sim 20\%$, and increases by another 15% for $\Phi_c = 25\%$ and 23% for $\Phi_c = 30\%$. The initial increase at $\Phi_c = 10\%$ from $C_2 = 1$ to $C_2 = 1.36$ is due to the gel-fluid phase transition. The second increase at $\Phi_c = 20\%$ appears to indicate some further major change in the packing of the lipid molecules. At $\Phi_c = 20\%$, the cholesterol concentration in the L_o phase is around 30%, as shown in Figure 3.5 (c). This may be correlated with the sudden increase in the inter-chain spacing after $x = 30\%$, as indicated by Wide angle X-ray scattering measurement by Mills et al. [58]. As noted by Hung et al. [45], after cholesterol complexing saturates after 38% cholesterol, more cholesterol would still go into the sample as 'free cholesterol'. This sudden change in chain packing after 30% cholesterol can be caused by the increased number of 'free' cholesterol when the number of 'complexing cholesterol' close to saturation. The saturation of the 'complexing cholesterol' is also indicated by the PtP measurement in Figure 3.6.

3.5 Summary and Discussions

In summary, the newly developed BLP scaling method is shown to be useful in the quantitative analysis of the relatively subtle changes in the EDPs of the L_o

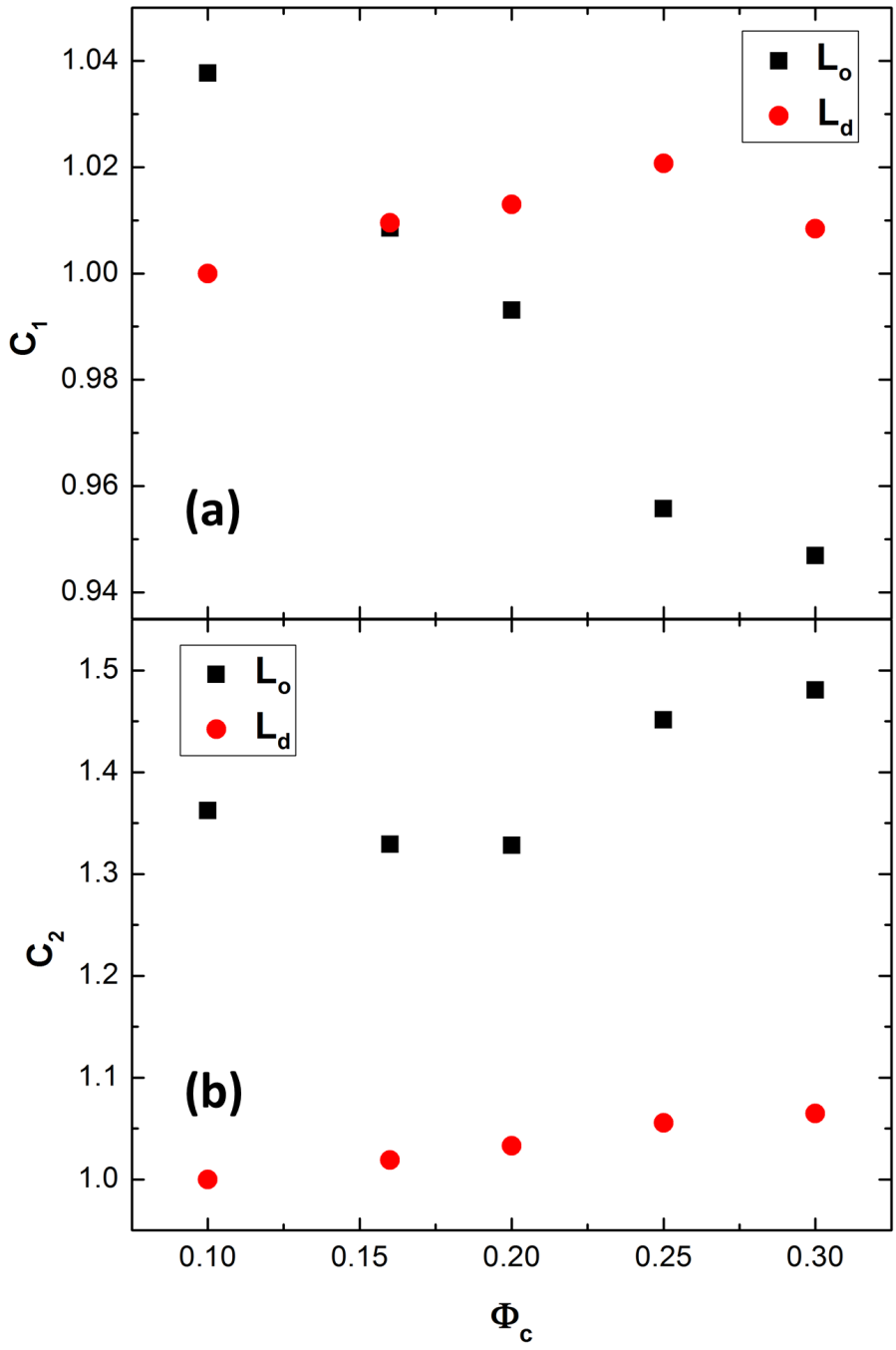

Figure 3.8: (a) The scaling factor for the overall electron density amplitude C_1 plotted vs. Φ_c. (b) the scaling factor of Gaussian width C_2 vs. Φ_c. The error bars are comparable to the symbol sizes.

and L_d phases with increasing cholesterol content. With this analysis method, we can localize the added component (in this case cholesterol) with high accuracy and quantify the resulting increase of electron density, as well as the changes in lipid packing, as well as quantify the partition of cholesterol into the two phases, as we hope we have demonstrated in this paper.

We have determined the cholesterol concentrations x in each of the L_o and L_d phases as a function of the initial cholesterol concentration Φ_c. Cholesterol starts to partition into the L_d phase only after adding more than 10% cholesterol into the sample ($\Phi_c = 10\%$). The cholesterol distribution coefficient is found to obey a simple relation to Φ_c as shown in Eq. 3.11. In our studies of the 10% and 16% cholesterol samples, we did not observe any 3 phase coexistence over repeated experiments. This result disagrees with results by Chen et al. [44] obtained for multi-lamellar vesicles using a synchrotron source. We postulate that it might be due to the non-homogeneous or non-equilibrium conditions of their vesicle samples.

The measured phosphate-to-phosphate distances (PtP) show that the condensing effect for the DPPC-rich L_o phase is stronger than for the DOPC-rich L_d phase, which supports previous studies of the condensing effect by Hung et al. [45]. The average molecular area is calculated according to the measured PtP values from Eq. 3.12 and 3.13.

The position of the maximum in the electron density in the cholesterol ring was measured for both the L_o and L_d phases to be around 12Å and 9Å from the bilayer center. These numbers support the previous studies of the cholesterol packing behavior, which show that the cholesterol molecules align themselves with the interface between the hydrophilic headgroups and hydrophobic tailgroups of the lipids.

The disorder of the lipid packing as a function of initial cholesterol concentration is quantified for both phases. The disorder increases by 36% upon adding 10% cholesterol to the sample (for the DPPC-rich L_o phase, while no change is found for the DOPC-rich L_d phase. This significant increase of disorder in the DPPC-rich phase is mainly due to a change from the gel phase to the liquid ordered phase. For Φ_c larger than 10%, the disorder of the L_o phase stays roughly

the same (decreasing by 3%) until $\Phi_c = 20\%$, after which the disorder increases again by another 12 15% for $\Phi_c = 25\%$ and $\Phi_c = 30\%$. This indicates that another major change in packing occurs in the L_o phase around $\Phi_c = 20\%$, which may be due to a dramatic increase in the inter-chain spacings. For the L_d phase, the total increase of the disorder parameter is around 6%.

3.6 Acknowledgement

I would like to acknowledge my co-authors Sajal K. Ghosh, David A. DiLena, Sambhunath Bera, Laurence B. Lurio, Atul N. Parikh and Sunil K. Sinha for the work in this chapter.

4 Accurate Calibration and Control of Relative Humidity Close to 100% by X-raying a DOPC Multilayer

4.1 Overview

In this study, we have designed a compact sample chamber that can achieve accurate and continuous control of the relative humidity (RH) in the vicinity of 100%. A $1,2-dioleoyl-sn-glycero-3-phosphocholine$ (DOPC) multilayer can be used as a humidity sensor by measuring its inter-layer repeat distance (d-spacing) via X-ray diffraction. We convert from DOPC d-spacing to RH according to a theory given in the literature and previously measured data of DOPC multilamellar vesicles in Polyvinylpyrrolidone (PVP) solutions. This curve can be used for calibration of RH close to 100%, a regime where conventional sensors do not have sufficient accuracy. We demonstrate that this control method can provide RH accuracies of 0.1 to 0.01%, which is a factor of 10-100 improvement compared to existing methods of humidity control. Our method provides fine tuning capability of RH continuously for a single sample, whereas the PVP solution method requires new samples to be made for each PVP concentration. The use of this cell also potentially removes the need for an X-ray or neutron beam to pass through bulk water if one wishes to work close to biologically relevant conditions of nearly 100%

RH.

4.2 Introduction

There are currently two commonly used methods for relative humidity (RH) control. One utilizes air/water vapor flow, for which the accuracy is usually $\pm 1 \sim 2\%$ for the RH range from 0% to 95%. The second method involves placing a reservoir with saturated salt solution in the chamber, which gives a discrete number of values of the RH, depending on the kind of salt used, e.g., $NaCl$ for 75% RH and K_2SO_4 for 97% RH. Both methods require a uniform temperature environment. A small temperature fluctuation or a temperature gradient would easily result in $\pm 1\% \sim \pm 2\%$ error in RH. To our knowledge, accurate and continuous humidity control with an error of less than $\pm 0.1\%$ for high humidity values ($95\% \sim 100\%$ RH) has not been shown with these methods. To achieve high accuracy humidity control close to 100% RH, one must control the temperature gradient and have an accurate measure of the RH. No existing RH sensor in the market can measure with accuracy close to or better than 0.1%. To design such accurate RH control, one needs to address both issues carefully.

Temperature uniformity and stability throughout the whole sample chamber is very difficult to control within such a small tolerance. This is exactly the cause of the widely debated vapor pressure paradox for lipid membranes [59], where better than 99% RH was not achieved. It has been experimentally proved by Katsaras that once the temperature gradient is eliminated, 100% RH can be achieved and no paradox exists [60, 61]. The Nagle group has also designed a chamber to achieve 100% RH for lipid bilayer X-ray measurements [62, 63], and neutron measurements (see www.humidity.frank-heinrich.net).

In order to achieve not only 100% RH, but also accurate and continuous control for a range of high relative humidities close to 100%, we have developed a chamber which controls a temperature differential. This method has been used previously for surface wetting studies [64, 65, 66].

In order to obtain an accurate measurement of RH, we need to use a calibra-

tion sample that responds very sensitively to RH changes close to 100%. We have chosen to use the lamellar repeat spacing of a $1,2-dioleoyl-sn-glycero-3-phosphocholine$ (DOPC) multilayer as a calibrant. It is well known that the water uptake of lipids responds very sensitively when the RH gets close to 100%. Although the possibility of using a supported lipid multilayer to measure RH has been previously mentioned in the literature [67], no rigorous calibration of the d-spacing vs. RH curve has been carried out directly with vapor chambers. This is mainly due to the lack of RH sensors with sufficient accuracy. In this study, we will try to establish this calibration standard by consolidating the theory given in the literature with the published data of DOPC multi-lamellar vesicles in Polyvinylpyrrolidone (PVP) solution, and use this curve as the calibration curve for our data with supported DOPC multilayers in a vapor chamber.

4.3 Chamber design

There are two main parts in our chamber design: the reservoir and the sample. A reservoir consisting of a 1% (mole fraction) K_2SO_4 solution serves as the humidity source which generates a constant water vapor pressure (we call this relative humidity the Reference RH). The sample is located where the desired RH is created. There are two independent temperature control loops: temperature control for the reservoir and temperature control for the sample. The two parts are connected via a weak thermal link. A schematic of the temperature control setup is given in Figure 4.1.

By controlling the temperature of the reservoir, T_{res}, and the temperature of the sample, T_{sam}, we can control the temperature difference $\Delta T = T_{res} - T_{sam}$. The distribution of water molecules in the water vapor will re-arrange according to the temperature gradient, which results in a re-distribution of relative humidity. As demonstrated in Figure 4.2 when $\Delta T = 0$ the sample is at the reference RH for 1% K_2SO_4 solution. Note that the use of an unsaturated salt solution produces an approximately temperature independent RH. When $\Delta T < 0$, RH of the sample is lower than the reference RH (Figure 4.2 (c)); similarly when $\Delta T > 0$, it is higher

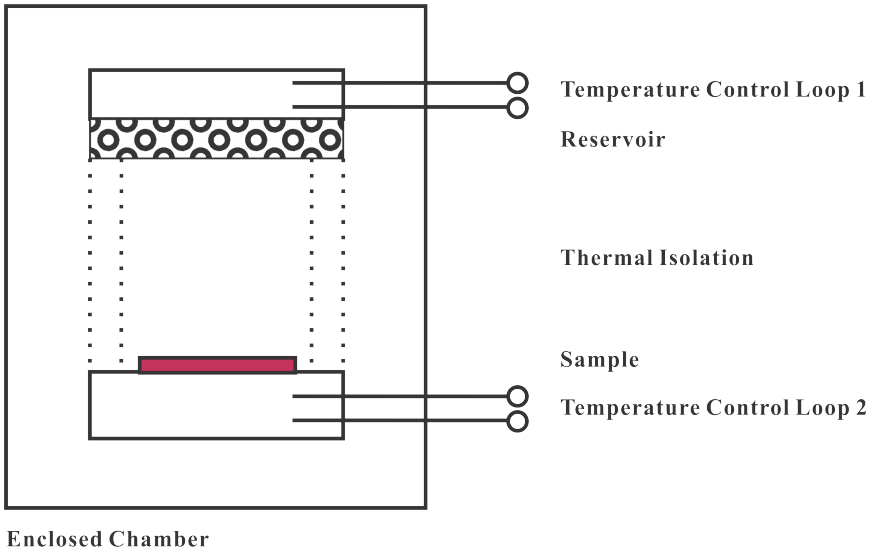

Figure 4.1: Schematic diagram of humidity control design. Inside the enclosed chamber, two independent temperature control loops are set up for the reservoir and the sample. Thermal isolation material is required in between to isolate the two temperature control loops.

(Figure 4.2 (a)).

Figure 4.3 shows pictures of our humidity controlled sample chamber used as a cell for X-ray diffraction and optical microscopy measurements. The chamber consists of two parts: The top (Figure 4.3 (b)) with reservoir and the bottom (Figure 4.3 (c)) with sample. The two parts have independent temperature control loops, and are thermally separated by a Teflon ring. The reservoir solution is contained in a sponge. The sponge and the sample are kept in close contact with the respective part of the sample chamber to favor temperature equilibration. The sample chamber is constructed with copper to ensure good thermal uniformity. A Lakeshore temperature controller with two control loops is used for the temperature control.

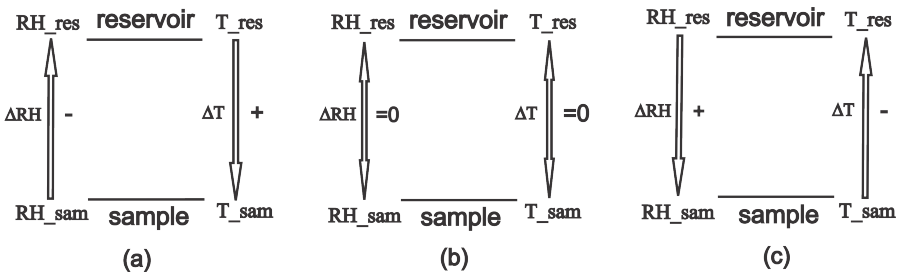

Figure 4.2: Schematics of the principle of temperature differential method applied to relative humidity control. By controlling the temperature differential between the reservoir and the sample (shown as arrows on the right side of each diagram), a relative humidity differential will be generated (shown as arrows on the left of each diagram). As demonstrated by the arrow directions, the relative humidity differential generated is in the opposite direction to the temperature differential.

4.4 Calibration of the DOPC d-spacing vs. relative humidity curve

Measurements of a DOPC multilayer as a standard sample were carried out to measure the RH of the sample environment. X-ray diffraction measurements of the lamellar repeat distance or d-spacing of the DOPC multilayer sample are a sensitive measure of the RH of the sample environment, since the uptake of water between the bilayers depends sensitively on RH particularly as the RH tends to 100%. In our experiments, the sample temperature is kept constant at $31°C$ while the reservoir temperature is raised to increase the RH at the sample. The DOPC multilayers are deposited using spreading method developed by Li et al. [18] and were annealed at $50°C$ for 1-2 days in a humidity chamber after taking out from the vacuum.

The X-ray measurements were taken on the diffractometer at sector 33 BM at the Advanced Photon Source, Argonne National Laboratory with a $20keV$ X-ray beam. Figure 4.4 shows one set of diffraction measurements of a typical DOPC sample over a range of temperature gradient. The RH ranges from 97.1% to 100.000% if converted from measured d-spacing with the standard curve discussed below. As RH increases the diffraction peaks shift to lower q_z, which means the d-spacing is increasing. The gradual distortion and disappearance of higher orders

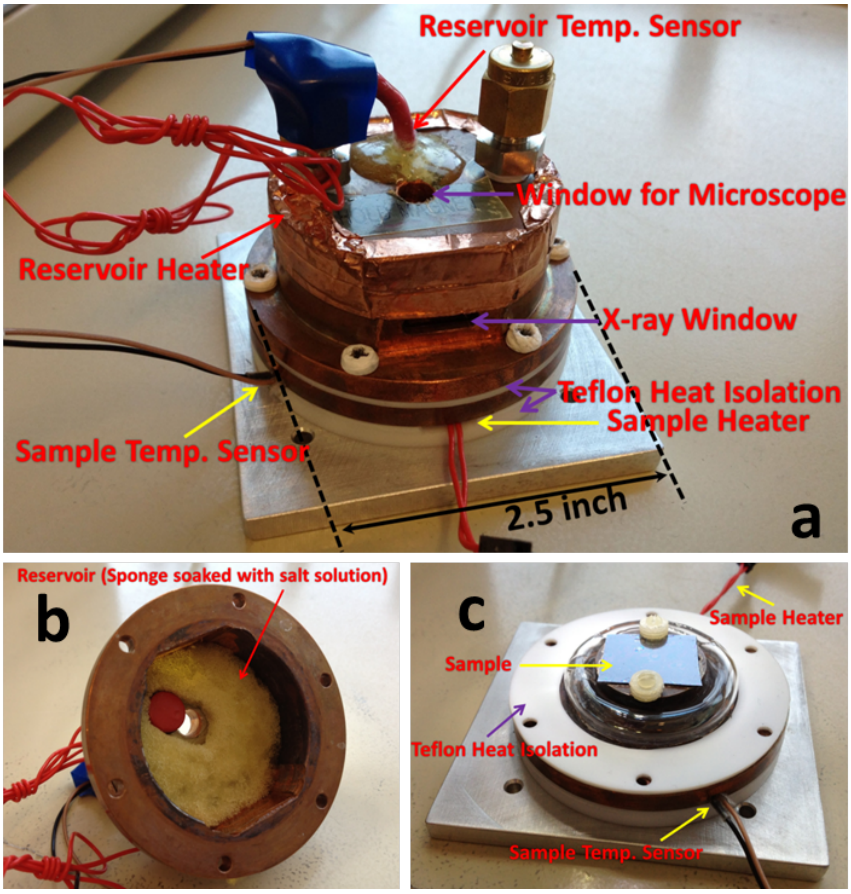

Figure 4.3: Pictures of our RH control chamber for X-ray scattering and optical microscopy measurements. (a) shows the assembled view, where the arrows mark all the functioning parts. The outer diameter of the chamber is 2.5 inch. The sponge sits inside the top to soak reservoir solution, as shown in opened view (b). The sample mounts on top of the bottom part, as shown in (c).

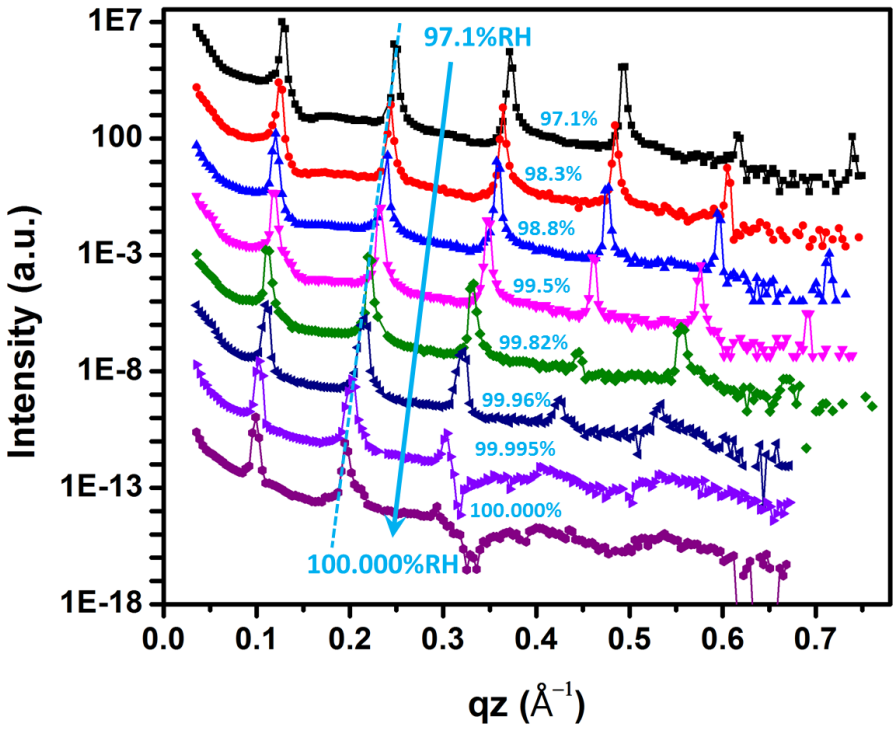

Figure 4.4: X-ray diffraction measurements of a DOPC multilayer sample with different RH. From top to bottom curve, the RH is increased from 97.1% to 100.000%. The RH values corresponding to each curve are indicated to the precision warranted by the percentage accuracy of the calibration. The dashed line marks the peak shifts to lower q_z values with increase of relative humidity.

of Bragg peaks is due to the increased undulations due to increased hydration, as explained by Nagle and Tristram-Nagle [2, 68, 69], as well as by Salditt [70].

There is no obvious standard established in the literature for converting from d-spacing to RH. The data which do exist contradict each other [5, 1]. We have resolved this conflict by using a theoretical model combined with existing experimental measurements.

4.4.1 Derivation of osmotic pressure

In order to calibrate our data for d-spacing as a function of RH, we will compare our results with measurements of the d-spacing of DOPC multi-lamellar vesicles in solution, where the osmotic pressure of the solution has been modified by the addition of PVP, a high molecular weight polymer. These measurements

should be comparable, since the osmotic pressure in solution, and the RH in vapor should have identical effects on the chemical potential of water in the multilayers. According to Petrache et al. [4], the osmotic pressure of the multilayer, P_{osm}, can be decomposed into three contributions, a Helfrich fluctuation pressure, P_{fl}, a hydration pressure, P_h, and a van der Waals pressure P_{vdw}:

$$P_{osm} = P_{fl} + P_h + P_{vdw}. \tag{4.1}$$

The fluctuation pressure, P_{fl}, depends on the thickness of the water layer, a, and can be approximated with an exponential function with a decay length λ_{fl} of the form,

$$P_{fl} = A_{fl}\mathrm{e}^{-a/\lambda_{fl}}. \tag{4.2}$$

The hydration pressure, P_h can be written in a similar fashion in terms of a decay length λ_h,

$$P_h = A_h\mathrm{e}^{-a/\lambda_h}. \tag{4.3}$$

The van der Waals pressure [71], P_{vdw} has the form,

$$P_{vdw} = -\frac{H}{6\pi}\left(-\frac{2}{(D_B^{'}+a)^3} + \frac{1}{(2D_B^{'}+a)^3} + \frac{1}{a^3}\right). \tag{4.4}$$

Here, H is a Hamaker constant, $D_B^{'}$ is the bilayer thickness and a the water thickness. $D_B^{'} + a = d$, is the d-spacing of the multilayer.

In order to determine the values for the parameters $A_{fl}, \lambda_{fl}, A_h, \lambda_h, H$ and $D_B^{'}$ for DOPC, we need to fit this expression for P_{osm} to the experimental data.

4.4.2 Fitting data from Hristova and White [1] and Tristram-Nagle et al. [2]

In the paper by Hristova and White published in 1998 [1], a list of d-spacings vs. RH from 34% to 93% and PVP weight fractions from nominal 60% to 5% is given, as well as the number of water molecules per lipid n_w. In order to get a

calibration curve for RH> 95%, we took the 60% to 5% weight fraction PVP data and translated it into osmotic pressure.

To convert PVP concentration to osmotic pressure, we use the method described by Vink [72] in 1971. The concentration c can be calculated from the PVP weight fraction w,

$$c = \frac{w}{wv_2 + (1-w)v_1}. \tag{4.5}$$

Osmotic pressure can then be calculated using the relation:

$$P = A_1 c + A_2 c^2 + A_3 c^3. \tag{4.6}$$

The values of v_1, v_2, A_1, A_2, A_3 are taken from the same paper [72]. The PVP weight fractions are taken with values that are determined via refractive index measurements by Hristova and White [1]. The calculation results are listed in Table 4.1.

To calculate $D_B^{'}$, we used the method described by Nagle and Tristram-Nagle [68],

$$D_B^{'} = 2D_C + 2D_H \tag{4.7}$$

$$D_C = \frac{V_C}{A} \tag{4.8}$$

$$V_C = V_L + V_H \tag{4.9}$$

$$n_w = \frac{\frac{Ad}{2} - V_L}{v_w} \tag{4.10}$$

here D_C is the lipid tail group thickness and D_H is the lipid head group thickness. V_C is the lipid tailgroup volume, V_H is the lipid headgroup volume and V_L is the total volume of one lipid molecule. A is the lipid cross sectional area, v˙w is the volume of one water molecule and n_w is the number of water molecules per lipid.

One can solve for A and feed into the expression for $D_B^{'}$ and get

Table 4.1: Calculated values for $D_B^{'}$ and a according to Hristova and Whites data [1].

PVP %	$ln(P)$ (dyn/cm^2)	$D_B^{'}$ (Å)	a (Å)	d (Å)
58.54	17.7682	48.0	2.5	50.5
46.71	17.0538	48.2	4.3	52.5
42.97	16.7977	48.3	5.0	53.3
33.63	16.0689	47.6	5.9	53.5
23.42	15.0553	47.7	8.1	55.8
19.53	14.5723	47.8	9.2	57.0
14.39	13.8049	47.3	10.3	57.6
8.69	12.6616	47.5	12.7	60.2
5.09	11.6200	47.4	14.9	62.3

$$D_B^{'} = \frac{V_C d}{n_w v_w + V_L} + 2D_H \tag{4.11}$$

Put in values for $D_H = 9$Å obtained by Büldt et al. with neutron diffraction [73], $V_H = 319$Å^3 by Sun et al. with X-ray diffraction [74], $V_L = 1303.3$Å^3 by Tristram-Nagle et al. [2] with X-ray neutral flotation measurements, $v_w = 30$Å^3, n_w and d data given by Hristova and White [1], we get values for $D_B^{'}$ and a. These are given in Table 4.1.

Tristram-Nagle et al. [2] also have done detailed studies of DOPC swelling with osmotic pressure and published data of osmotic pressure vs. DOPC multilayer water spacing a, and osmotic pressure vs d-spacing [6]. When we compare the results of Tristram-Nagle and Hristova, we found that there is a discrepancy in the number of water molecules per lipid, which leads to a discrepancy in the calculated $D_B^{'}$. As listed in Table 4.1, $D_B^{'}$ is between $47.7 \sim 48.3$Å, while $D_B^{'}$ from reference [2] is between $45.3 \sim 46.5$Å in the same hydration range. This ~ 2Å discrepancy in bilayer spacing would lead to a shift of plots of osmotic pressure vs. water spacing a for the two published data sources.

However, when plotting the two data sources of osmotic pressure vs. d-spacing of DOPC, they agree very well, as shown in Figure 4.5. So we decided to combine the two published data of osmotic pressure vs. d-spacing, and fit with the function 4.4 by making $D_B^{'}$ a fitting parameter together with $A_{fl}, \lambda_{fl}, A_h, \lambda_h, H$.

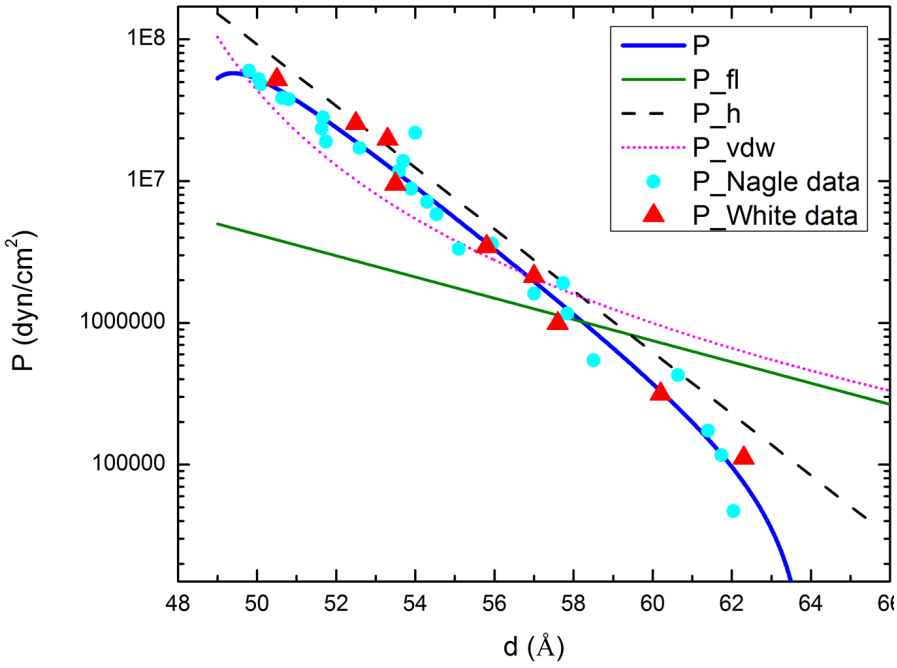

Figure 4.5: Simulation of osmotic pressure vs d-spacing curve fits to Hristova and Whites data16 and Tristram-Nagles data11 combined according to method used by Petrache et al. [4]. The red triangles mark Hristova and Whites data, the blue dots mark Tristram-Nagles data, the curved solid blue line shows the fit to log(osmotic pressure) vs. d-spacing. The straight solid green line shows the fluctuation pressure, the straight dashed black line shows the hydration pressure, and the curved dotted pink line shows the van der Waals pressure. Parameter values are given in Table 4.2.

The combined data set should give better accuracy than fitting either data alone.

There are multiple sets of parameters which can fit the data equally well if all the parameters are allowed to vary. We have chosen to fix the values of $lambda_{fl}$ and A_h at the values obtained by Tristram-Nagle et al.11. Since our purpose is to obtain a calibration curve for the d-spacing vs. osmotic pressure, we do not concern ourselves with the significance of the actual values of the fitted parameters. The result of the fitting is shown in Figure 4.5 and Table 4.2. The fitted $D_B^{'}$ value is close to reference [2].

With this calculated standard curve of P˙osm vs d-spacing, we can convert to RH vs. d-spacing using the relation between osmotic pressure and relative humidity [59]

Table 4.2: Parameter values for the fit to lnP data. The parameters in bold are the ones being varied.

A_{fl} $(10^6 dyn/cm^2)$	λ_{fl} Å	A_h $(10^9 dyn/cm^2)$	λ_h Å	H $(10^{-14} erg)$	$D_B^{'}$ Å
8.37	5.8	0.68	2.0	5.28	46.0

$$P_{osm} = -(\frac{kT}{v_w})\ln(RH). \tag{4.12}$$

The fitted curve of d-spacing vs. RH is plotted in Figure 4.6 together with the data of Hristova and White [1] and Tristram-Nagle et al. [2]. Also shown are our measured values of the DOPC d-spacing at various values of ΔT. The measured DOPC d-spacings vs. ΔT are plotted in Figure 4.7 (a). By putting these measured d-spacings onto the standard curve, we can establish the RH vs. ΔT plot for our chamber environment (see Figure 4.7 (b)) which we shall now discuss in the next section.

4.4.3 Direct calculation of RH vs. ΔT using thermodynamic theory

Besides the experimental approach, we can also directly calculate the RH vs. ΔT from thermodynamic theory. This can serve as a reliability check for our experimental calibration.

Assuming ideal behavior, the RH at the reservoir is

$$r_{reservoir} = \frac{P}{P^*_{H20}} = x^{vapor}_{H20} = x^{liquid}_{H20} = 1 - \phi \tag{4.13}$$

Here, P is the partial pressure of water vapor at the reservoir, P^*_{H2O} is the saturated water vapor pressure, x^{vapor}_{H2O} is the mole fraction of water in vapor and x^{liquid}_{H2O} is the mole fraction of water in liquid and ϕ is the mole fraction of solute in the reservoir.

According to the Clausius-Clapeyron equation for a liquid-gas equilibrium,

$$\frac{dln(P)}{dT} \approx \frac{\Delta H_m}{RT^2} \tag{4.14}$$

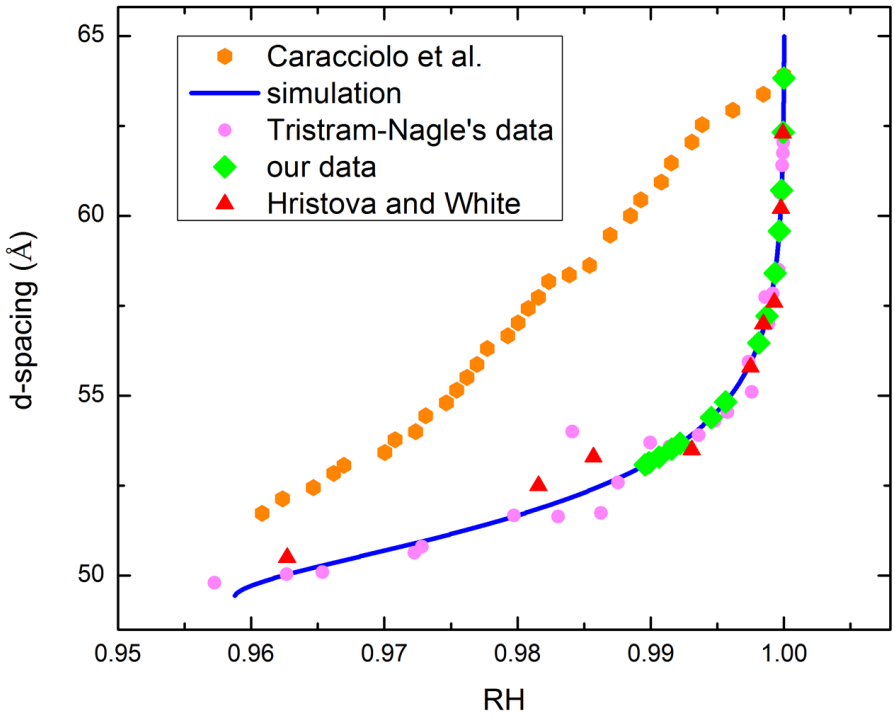

Figure 4.6: Comparison of DOPC d-spacing vs. humidity plots from different sources. Orange hexagonal are data published by Caracciolo et al. [5] . Red triangles are the data published by Hristova and White [1], translated from PVP to RH using the method described in the text. Pink dots are by Tristram-Nagle [2, 6], translated from osmotic pressure to RH. The blue line is our simulation shown in Figure 4.5 translated from osmotic pressure to RH with the same method. The green diamonds are our data translated according to the standard curve.

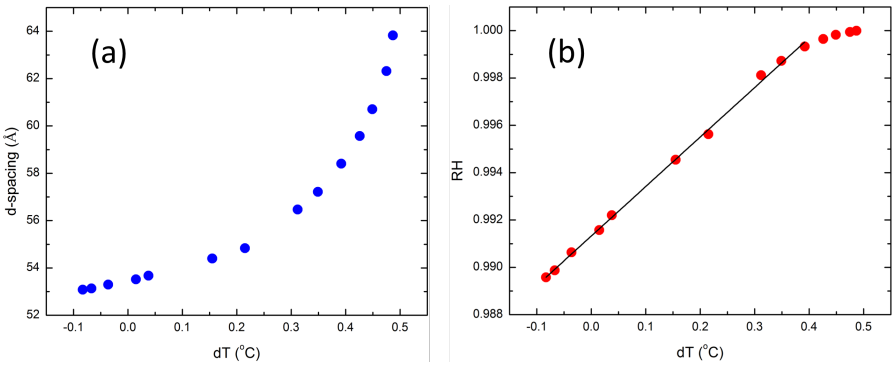

Figure 4.7: Plots of DOPC d-spacing (a) and relative humidity (b) vs temperature differential. Relative humidity values in (b) are mapped from DOPC d-spacings according to our simulation as shown with blue line in Figure 4.6. The temperature differentials plotted are nominal values, since we were not able to directly measure the temperature at the sponge.

where ΔH_m is the enthalpy of vaporization of water and T is the sample temperature which is not near the critical temperature T_c. The equation can be re-written as

$$ln\left(1+\frac{\Delta P}{P}\right) \approx \frac{\Delta P}{P} \approx -\frac{\Delta H_m \Delta T}{RT^2} \tag{4.15}$$

where ΔT and ΔP are respectively the temperature difference and the difference in partial pressure of water vapor between the sample and the reservoir.

Thus we have

$$r_{sample} \approx r_{reservoir} - \frac{\Delta H_m \Delta T}{RT^2} \tag{4.16}$$

where r_{sample} and $r_{reservoir}$ are RH at the sample and the reservoir respectively. This shows that to first order, the change in RH is proportional to the change in temperature ΔT. By putting in numbers of $\Delta H_m = 40.68kJ/mol$, $RT = 25.249J/mol$ and $T = 304K$, we obtain $\frac{\Delta H_m}{RT^2} = 0.0530$. Comparing this result to our experimental result in Figure 4.7 (b), our experimental result also shows a linear relation except for the last 4 points at $RH > 0.9995$. The linear fit of this data gives a slope of 0.0209, which is less than half of the theory predicted value.

After careful examination of the d-spacing equilibration time, we hypothesize that the reason for the last four points falling off the straight in Figure 4.7 (b) is that we did not allow enough time for the d-spacing to equilibrate. The waiting time at each temperature before measurement was around $20 \sim 25min$, which is not enough when RH gets very close to 100%.

We also carefully examined the temperature gradient in our chamber, and concluded that the discrepancy in the slope of linear fit is caused by a small temperature gradient between the sponge and the copper top. The temperature sensor for the reservoir is embedded in the copper top for good thermal contact. When heating up the reservoir relative to the sample, the temperature gradient is always negative from the copper to the sponge, which means the sponge is a little cooler than the sensor reading. This leads to a smaller experimental slope than the theoretically predicted value. In conclusion, the temperature differentials plotted are nominal temperature differentials, not the actual temperature between the

sample and reservoir. The fact that our data fall onto a linear relation predicted by thermodynamic theory when translated to RH vs. dT plot provides further support for the RH vs. d-spacing standard.

Detailed analysis of more lipid multilayer data using this humidity control setup will be presented separately in other papers by Y. Ma et al.(in preparation).

4.5 Discussion

4.5.1 Comparison with other literature

There are other papers in the literature reporting the evolution of the d-spacing of DOPC with RH, such as the paper by Caracciolo et al. [5]. We make a comparison of our simulations according to Petraches method, Hristova and Whites data, Tristram-Nagles data with Caracciolo et al.s data for the range of RH very close to 100% (Fig. 4.6). As can be seen, there is a significant discrepancy in Caracciolos data compared to the rest. The theory used by Petrache et al. from literature predicts a non-linear and diverging behavior of lipid d-spacing with change in RH at high RH range, and Hristova and White and Tristram Nagles data also suggest that, while Caracciolo et al.s data shows an almost linear relation at the same range.

We think that the discrepancy can come from 2 sources. Firstly, Caracciolo et al.s study was time dependent. The measurement of d-spacing was done while the humid air was continuously flowing into the chamber and increased RH in real time. At lower humidities, the d-spacing changes slowly with RH, so it can still catch up and be close to equilibrium; however, at high RH values close to 1, the d-spacing changes are much larger for the same amount of change in RH due to the divergent behavior, and thus in real-time the d-spacing no longer catches up with the change of RH therefore the measurements on the fly are not under equilibrium conditions. For example, measurements by Servantes [75] show that it can take up to several hours for a multilayer to equilibrate for RH near 100%.

A second possibility is the non-accurate reading from the RH sensor. The humidity is measured with a humidity sensor in Caracciolo et al.s study while

Hristova and Whites data are PVP weight fraction calculated from refraction index measurements on the sample. It is well known that for the current humidity sensors on the market, the accuracy is around $\pm 1\%$, and would not be able to determine changes on the order of 0.1% or less. So in this case, it is quite possible that the RH sensor is already saturated when RH is close to 1 and yields readings larger than the actual humidity in the chamber. On the other hand, the refraction index measurements can be more accurate for determining the PVP weight concentration and thus give a more accurate measure when converted to RH.

4.5.2 Discussion of errors

To estimate the error of RH, we need the error of d-spacing measurements, and also the error in the standard conversion curve. The error bars for the d-spacing measurements in Figure 4.7 (a) are between 0.014Å to 0.031Å, which are $0.02\% \sim 0.05\%$ errors, much smaller than the symbol size to plot. We can estimate the errors of the standard conversion curve from the reduced Chi-square of the fitting. The reduced Chi-square is 0.10 in the $ln(P)$ fit, so the dP/P is approximately $\sqrt{0.10} = 0.32$. From the differential of equation 4.12, we can get the error of RH between 0.32% to 0.00047% in the RH range 99% to 99.999%.

4.5.3 Advantages of the present method

We believe that our compact and economic chamber design together with using a calibration standard would be helpful for future studies of soft materials and bio materials which rely on a high humidity environment. In our own experiments we put a standard DOPC sample with an actual sample side by side. By switching the two in and out of the X-ray beam, one can get the RH value from measuring the d-spacing of the DOPC multilayer and also get real measurements from the actual sample under the same conditions. If one is confident about the thermal contact between the sponge and the cell, as well as the accuracy of salt solution, one can also use the calibration curve to control ΔT without using a DOPC sample once the cell is calibrated.

There are three main advantages of this method. Firstly, it is clear that in the multilayer case, compared to measurements in solution with PVP, our results using a vapor chamber have better accuracy (smooth curve) and stronger signal (we can still see the third order diffraction peak at 100% RH). Secondly, our method makes it possible to change the RH of the environment by simply tuning the temperature differential, which enables measurements under different conditions on the same piece of sample. In the PVP method, one has to make a different sample for each PVP concentration. For experiments with large sample-to-sample variance but looking for subtle changes in a given sample under different conditions (which might be true for a lot of soft matter experiments), this can be a big advantage. Finally, samples under saturated vapor pressure are more amenable to studies using x-rays and neutrons since problems associated with absorption and scattering in the water overlayer are not present.

4.5.4 Further discussion

There are some points to be noted for designing and using such a chamber. First of all, using a non-saturated salt reservoir instead of pure water can help because it lowers the reference RH, at the same time increasing the required temperature differential. Secondly, the extremely compact design of the sample chamber makes a difference. As demonstrated, our chamber is 2.5 inch in outer diameter, which can fit in ones palm. The small volume makes temperature control much easier–less non-uniformity and faster equilibration. The parts are easy to make, assemble, maintain and transport. It is also worth noting that this chamber design works best at temperatures a few degrees above ambient temperature. With only heating elements, the chamber will not operate below ambient temperature; on the other hand, if the temperature is set too far above from ambient temperature, water condensation on the inner window can create problems and frequent wiping is required. For lower and higher temperatures (such as $10°C$ and $50°C$), an additional temperature regulated layer of enclosure outside our described cell is recommended to raise or lower the ambient temperature.

Last but not least, the chamber can be equipped and used for a wide range

of non-contact measurements. For example, our chamber can do X-ray experiments at the same time as optical microscopy. For contact experiments, similar principles apply, one simply has to pay special attention to the sealing of the chamber and avoidance of cold spots.

4.6 Acknowledgements

X-ray data were collected on beamline 33BM at the Advanced Photon Source, Argonne National Laboratory. The authors would like to thank beamline scientists Evguenia Karapetrova and Christian Schlepuetz for their great help. Use of the Advanced Photon Source was supported by the U. S. Department of Energy, Office of Science, Office of Basic Energy Sciences, under Contract No. DE-AC02-06CH11357.

This work was supported by the Office of Basic Energy Sciences, U.S. Dept. of Energy under DOE Grant number: DE-FG02-04ER46173.

I would like to acknowledge my co-authors Sajal K. Ghosh, Sambhunath Bera, Zhang Jiang, Stephanie Tristram-Nagle, Laurence B. Lurio, and Sunil K. Sinha for the work in this chapter.

5 Anomalous Swelling Type II in Phase Separated Ternary mixture Lipid multilayers

5.1 Overview

X-ray diffraction is used to determine the hydration dependence of a ternary mixture lipid multilayer structure which has phase separated into liquid-ordered (L_o) and liquid-disordered (L_d) phases. An anomaly is observed in the swelling behavior of the L_d phase at a relative humidity (RH) close to 100%, which is different from the anomalous swelling that happens close to the main lipid gel-fluid transition. The lamellar repeat distance of the L_d phase swells by an extra 4Å, well beyond the equilibrium spacing predicted by the inter-bilayer forces. This anomalous swelling is caused by the hydrophobic mismatch energy at the domain boundaries, which produces a surprisingly long-range effect.

5.2 Significance Statement

A novel kind of anomalous swelling behavior is discovered in the phase separated ternary mixture lipid multilayers by X-ray diffraction. Different from the well-known anomalous swelling close to the main lipid gel-fluid transition, the anomalous swelling reported here occurs close to 100% hydration due to the hydrophobic mismatch energy at the domain boundaries. An extra swelling of 4Å

is discovered, which is a comparatively stronger unbinding-effect compared to the thermal anomalous swelling. This phenomenon is an interesting example of the energetics of domain boundaries exerting long range effects on the inter-lamellar behavior. This effect may also be present in other similar smectic systems with accumulated domain boundary energies.

5.3 Introduction

As model systems of biological membranes, lipid multilayers exhibit a rich variety of structures and phase equilibria due to an intricate interplay between different intrabilayer and interbilayer forces. Lipid multilayers are commonly used as model systems for X-ray and neutron scattering structural studies. A repeated lamellar spacing (d-spacing) is usually measured. For lipid bilayers with neutral charge, the water layer thickness between the bilayers is decided mainly by the van der Waals interaction, hydration forces and Helfrich repulsion [4]. There are different ways of changing the water content by manipulating the repulsive undulation force [76], such as adding salt to the aqueous solution [77, 78] and changing bilayer material to change the curvature elasticity [79, 80]. The substrate effects also suppress the undulation for several bilayers close to the solid support [81].

Since Hnger et al. reported the phenomenon of anomalous swelling of lipid bilayers near the main transition temperature in 1994 [82], there has been much attention paid to this phenomenon [83, 63, 84, 85, 86, 87, 88]. This extra swelling is explained by the sudden softening of the membrane when crossing the main transition temperature, which increased the undulation and Helfrich repulsion. The effect is lipid dependent, e.g., a typical anomalous swelling for $1,2-dimyristoyl-sn-glycero-3-phosphocholine$ (DMPC) is about an extra 2Å increase in the water thickness at the main transition [88].

In this article, we report another type of anomalous swelling, which is not related to the phase transition, but rather due to the pure geometrical effect of domain boundaries. This novel phenomenon is discovered in phase-separated mixed lipid multilayers, in which the interlayer coupling plays an important role in the

columnar order of registered domains as reported in our earlier research [25]. The phase separation in model ternary mixture lipid systems has been studied extensively following the work of Veatch and Keller on phase diagrams [10, 9, 11, 13]. In previous work [25], we have shown that when the ternary mixture is made into a multilayer, the phase separated domains in each bilayer would couple with domains of the same phase in neighboring bilayers through the interlayer coupling interactions. This coupling is a long range effect, which leads to columnar order crossing hundreds of bilayers, basically across the whole sample.

To interpret those results, we postulated a layered structure according to the deduced electron density profiles from the X-ray measurements of the multilayers under partial hydration (a relative humidity (RH) around $96 \sim 98\%$), where the water layer thicknesses in the different phases are very similar, therefore the hydrophobic mismatch energy is accumulated at the domain boundaries. In this study, we demonstrate that when the system gradually approaches full hydration, a super swelling state, or a pseudo-unbinding state of the L_d phase occurs in order to adjust for the boundary mismatch energy (as depicted in Figure 5.1).

5.4 Results

5.4.1 I. X-ray diffraction experiment

The multilayer being studied here was composed of 1:1 DOPC:DPPC with 16% cholesterol. At $28°C$, the system is phase separated into a liquid-ordered (L_o) phase and a liquid-disordered (L_d) phase and forms columnar order across the sample. Using the accurate humidity control setup we developed in previous studies [53] which controls the sample RH via tuning the temperature differential between the sample and the reservoir (which we denote by dT), we measured the hydration response of the multilayer using X-ray diffraction. The sample temperature was kept constant at $28°C$, while the reservoir temperature was raised to provide dT. The data are shown in the Figure 5.2 as a 3D waterfall plot.

In Figure 5.2, we can see that with RH increasing from 98.96% (top curve in black) to 100% RH (bottom curve in teal), the two sets of distinct Bragg peaks

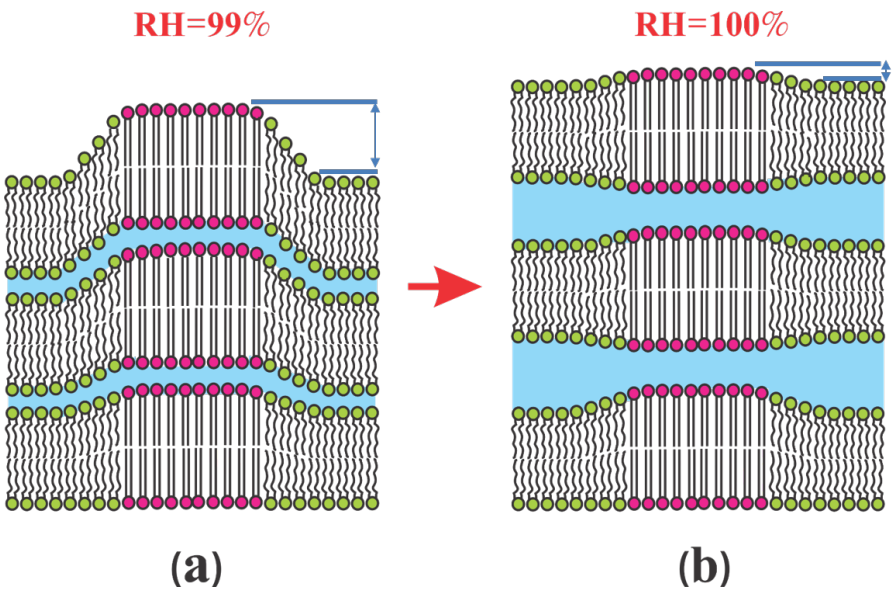

Figure 5.1: Schematic drawing of the lipid multilayer structure at partial hydration (a) and full hydration (b). At 99% RH, the system stacks up with similar water layer thickness (blue) for the L_o phase (red) and L_d phase (green), while at 100% hydration, the water in the L_d phase swells to make up for the lipid length difference, therefore a pearl-shaped water layer structure forms across domains.

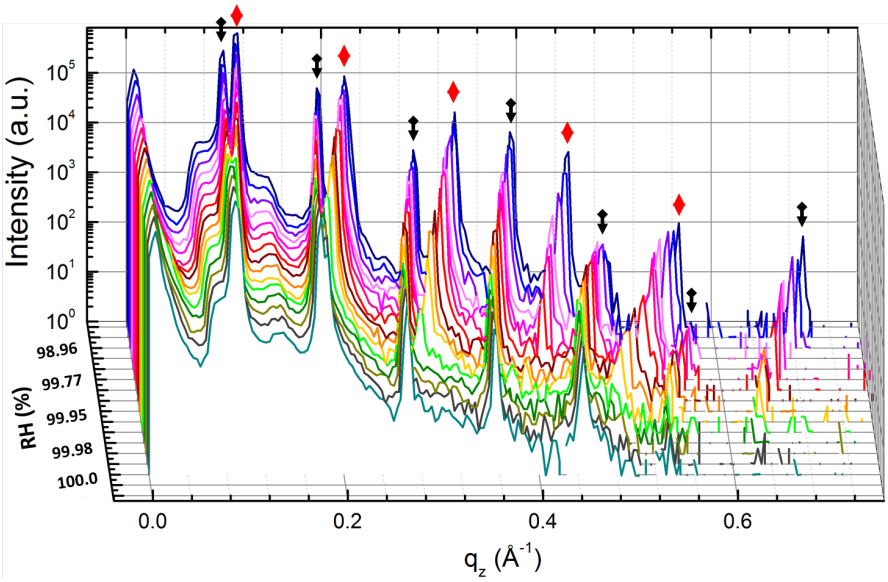

Figure 5.2: X-ray diffraction data of a multilayer consisting of 1:1 DOPC:DPPC with 16% cholesterol for different RH. The RH increases from 98.96% for the top curve in black, to 100% for the bottom curve in teal. The red diamond arrows mark the diffraction peaks associated with L_d phase, while the black double arrows mark the L_o phase.

gradually merge together. The lamellar spacing is calculated as $2\pi n/q_B$, where n is the order number of the Bragg peak and q_B is the Bragg peak position. As the Bragg peaks of the two phases start merging together, the d-spacings get closer to one another.

An optical microscope was mounted in the sample chamber to monitor the sample surface morphology during the X-ray diffraction experiment. As shown in Figure 5.3, the vertical yellow lines on the optical images marks the X-ray beam illuminated area (the footprint), while the yellow cross in the middle marks the X-ray beam center. Optical images (a) $\sim$ (h) were taken at the same time while the d-spacings (a) $\sim$ (h) were measured individually between 98.96% RH to 100% RH. The highly accurate high humidity control worked extremely well: as the d-spacing saturates and indicates 100% RH, the optical image shows small water droplets condensing on the sample surface at the same time (h). After which, we continue to increase the temperature differential to condense more water on the sample surface, which can be visualized in optical images (i) $\sim$ (k), when (k) shows the whole sample is covered by water. During the process of more than 10 hours, the sample was stable the whole time.

The circular features shown on the sample surface (Figure 5.3 (a) $\sim$ (g)) were identified as L_o phase domains from our fluorescence microscopy measurements (see Supplementary material Figure 5.8). The contrast in the optical images is the result of the sample surface morphology, in other words, the surface height differences between the L_o and L_d phases. Also the color contrast (light pink vs. green) comes from the Newton ring effect on different film thicknesses. When comparing image (a) to image (g), one can see that the height difference between the two phases decreases dramatically from (a) to (g), while the sudden change happens around (e), which can be traced back to the accelerated rate of increase of the d-spacing around (e) in the center plot. Somewhere between (d) and (e), the d-spacing of the L_d phase starts to swell anomalously.

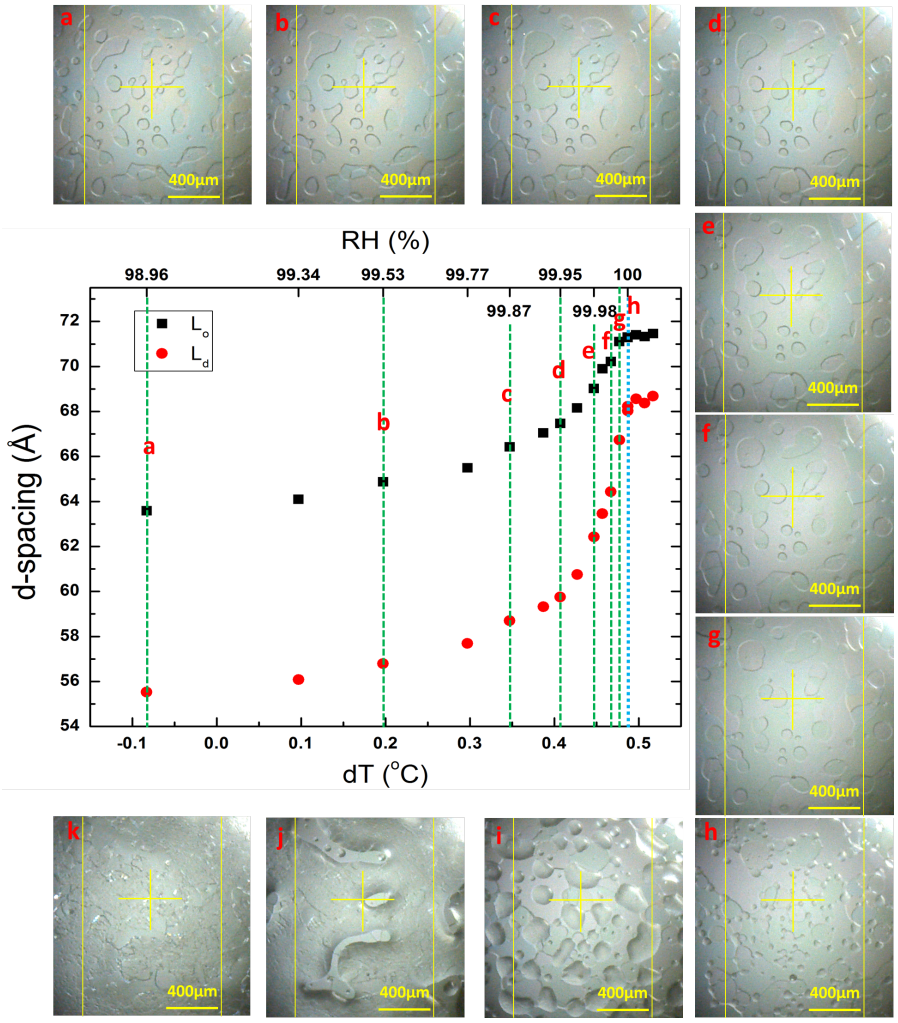

Figure 5.3: d-spacing vs. temperature differential (bottom axis) and RH (top axis) plot of both L_o and L_d phase (middle plot) and optical microscopic pictures of the sample surface morphology (surrounding pictures). The RH increases from (a) 98.96% to (h) 100%, and stays 100% while increasing the temperature differential to continue condensing water on the sample (i), (j), and finally the sample is all covered with water (k).

5.4.2 II. Electron density profile (EDP) construction

In order to understand the change in d-spacing, we need to construct the relative electron density profile (EDP) for each hydration condition. EDPs are constructed from the integrated intensities of the Bragg peaks with the following equation [33]:

$$\rho_{relative}(z) = \frac{2}{d}\sum_{n}\nu(n)\sqrt{nI_n}cos\left(\frac{2\pi nz}{d}\right), \tag{5.1}$$

where d is the lamellar spacing, $\nu(n)$ is the phase factor for the $n-th$ order reflection, I_n is the integrated intensity of the $n-th$ order Bragg peak. The factor $\sqrt{n}$ arises from the Lorentz correction of q_z^{-1} applied to the raw intensities I_n.

The correct choice for the combination of phase factor $\nu(n)$ is essential for the correct EDP construction. The swelling method [35] is the most commonly used method to determine the phases. Normally, diffraction data from 3 or 4 different but closely spaced hydration conditions are used to determine the phases accurately assuming the bilayer structure remains constant while swelling at partial hydration [45, 55]. In our case, measurements were carried out under a range of conditions close to full hydration, and the changes with d-spacing are dramatic. When plotting the scattering amplitudes (Figure 5.4), we can see that they do not fall on a single smooth curve of the Fourier transform of the bilayer EDP relative to water. Thus the bilayer structure must have changed during the swelling process [56]. However, the structure change must be continuous, so that the scattering amplitudes can be fitted with slightly shifted form factors for each of the several continuous conditions. The change in form factor is due to the increased fluctuations of the bilayers [2, 68, 69, 70]. The hydration increase close to 100% RH increases the fluctuations in the membrane, and therefore smears the form factor of the bilayer. When comparing between the L_d phase (Figure 5.4 (b)) and the L_o phase (Figure 5.4 (a)), we can see that the form factor shift in the L_d phase (3 fitting curves) is more than in the L_o phase (2 fitting curves), which agrees with the fact that the L_d phase membrane (DOPC-rich) is much softer than that of the L_o phase (DPPC-rich). The phase factor choice for each order is +1 if above zero

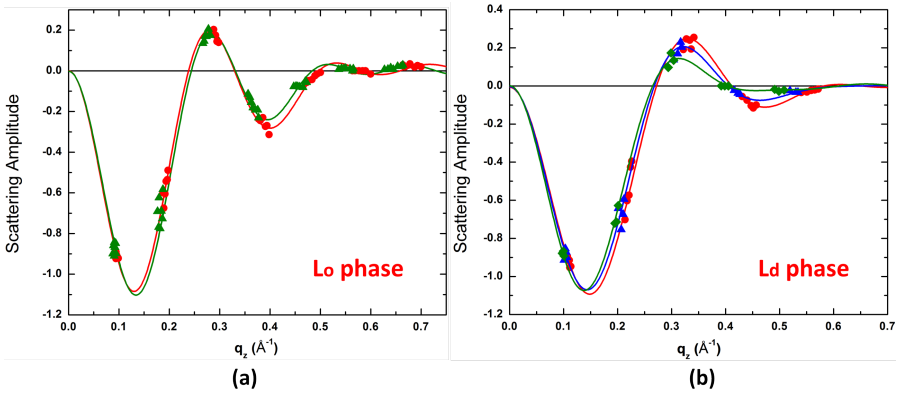

Figure 5.4: Phasing diagram for L_o phase (a) and L_d phase (b). The scattering amplitudes are sampling the slightly shifted Fourier transform of the bilayer EDPs relative to water due to the bilayer form factor changes resulted from the increased fluctuations in the membrane. The increase in fluctuation is greater in the L_d phase (b) than in the L_o phase (a), as DOPC has a smaller bending modulus than DPPC.

or -1 if below zero, as can be read out from Figure 5.4.

After the correct choices for the phase factors are made, we can construct the EDPs for each phase. Figure 5.5 shows the constructed EDPs for L_o (a) and L_d (b) phases, with RH increasing from the bottom curve to the top. The L_o phase EDPs are all reconstructed from 7 orders of Bragg peaks, while the L_d phase EDPs are constructed from 5 orders of Bragg peaks, except the top two dotted curves close to full hydration where only 3 orders of Bragg peaks are left present. The loss of the higher order peaks for the DOPC rich phase due to fluctuations at full hydration agrees with our previous result on pure DOPC [53]. It is evident that although the EDPs continue to smear out with increasing hydration, the bilayer thicknesses stay the same: the phosphate-to-phosphate distances (PtP) do not change during swelling, as marked with the vertical dotted green line.

5.4.3 III. Anomalous swelling type II

As shown in Figure 5.6 (a), the PtP distances for each phase are fairly constant with some small variations. Taking the average values of 44.8Å and 38.4Å for the PtP distances of the L_o phase and the L_d phase respectively, we can calculate the water layer thickness from the measured d-spacings:

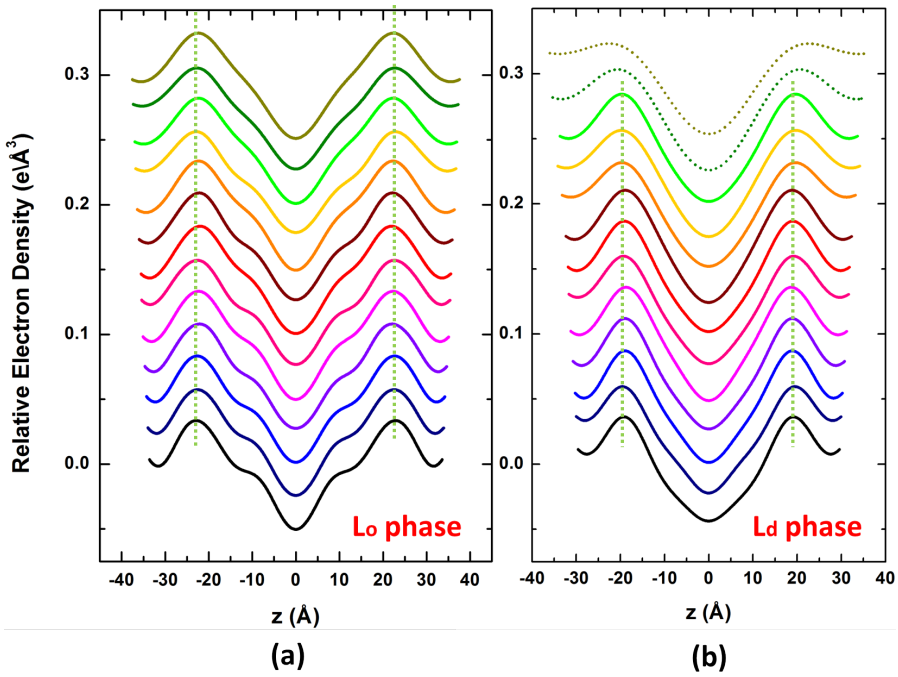

Figure 5.5: Relative EDPs of L_o phase (a) and L_d phase (b), shifted for clarity. RH ranges from 98.96% for the bottom curve to 100% for the top curve. The vertical green dotted lines mark the center of the headgroup positions, which do not change with hydration. The top 2 dotted EDP curves of (b) are constructed with 3 orders of Bragg peaks, which give less resolution for the bilayer structure.

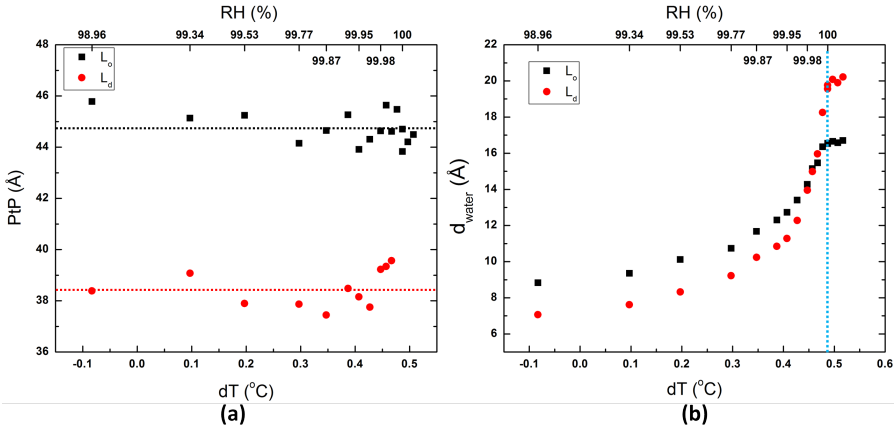

Figure 5.6: (a) PtP distance of the L_o phase (black squares) and the L_d phase (red dots) vs. RH (dT). The dotted horizontal line marks the average value. (b) Calculated water thickness vs. RH (upper scale) and dT (lower scale). The black squares represent the L_o phase while the red dots represent the L_d phase. The vertical blue dotted line marks the 100% RH point, where the d-spacings for both phases saturate at the maximum value.

$$d_{water} = d - PtP - 10, \tag{5.2}$$

where 10Å is a good estimate of the headgroup size [45]. The resulting water layer thicknesses d_{water} are plotted in Figure 5.6 (b).

From the plot, we can see that at partial hydration of 98.96% RH, the water layer thickness of the L_d phase is about 1Å smaller than that of the L_o phase, while somewhere close to 99.95% RH, the water spacing of the L_d phase starts to increase faster, and catches up with that of the L_o phase at around 99.98% RH, and continues to swell well beyond the water thickness of the L_o phase at 100% RH by 4Å.

To quantitatively understand this anomalous swelling phenomenon, we employed the theoretical model by Petrache et al. [4] and the fitting method used in our previous study [53] to simulate a normal swelling curve to compare with our data. In a pure lipid multilayer, the water thickness between bilayers is a result of balance between the osmotic pressure of the multilayer, which is the effective combination of the Helfrich fluctuation pressure, the hydration pressure, and the van der Waals pressure:

$$P_{osm} = P_{fl} + P_h + P_{vdw}. \tag{5.3}$$

While the fluctuation pressure and the hydration pressure can be both approximated with exponential functions with decay length λ_{fl}, λ_h [89]

$$P_{fl} = A_{fl}\mathrm{e}^{-a/\lambda_{fl}} \tag{5.4}$$

$$P_h = A_h\mathrm{e}^{-a/\lambda_h} \tag{5.5}$$

The van der Waals pressure has the form

$$P_{vdw} = -\frac{H}{6\pi}\left(-\frac{2}{(D_B^{'}+a)^3} + \frac{1}{(2D_B^{'}+a)^3} + \frac{1}{a^3}\right). \tag{5.6}$$

Here, H is the Hamaker constant, $D_B^{'}$ is the bilayer thickness and a the water thickness. $D_B^{'} + a = d$, is the d-spacing of the multilayer.

The osmotic pressure can be converted to relative humidity using the following expression [59]

$$P_{osm} = -\left(\frac{kT}{\nu_w}\right)\ln(RH) \tag{5.7}$$

In which $\nu_w = 30\text{Å}^3$ is the volume of a water molecule. The simulated normal swelling curves are plotted against our data in Figure 5.7, and the parameters used are shown in supplementary materials Table 5.1. In Figure 5.7 (a), the d-spacing vs. RH (dT) is plotted. The black dotted line represents the simulated curve of normal swelling for the L_o phase, while the red dashed line represents that of L_d phase. The anomalous swelling amount is marked by the green double arrow. Because the change in d-spacing at close to 100% RH is very steep, we convert the RH to the osmotic pressure and plot ln$P$ vs. d-spacing in Figure 5.7 (b) for better visualization and analysis. The blue dots represent the data for the L_d phase, while the black squares represent the data of the L_o phase. The normal swelling simulation curve is represented by the corresponding solid lines. The vertical blue dashed line marks the saturation d-spacing of the L_d phase, while the black dashed line marks the saturation d-spacing of the L_o phase, which actually

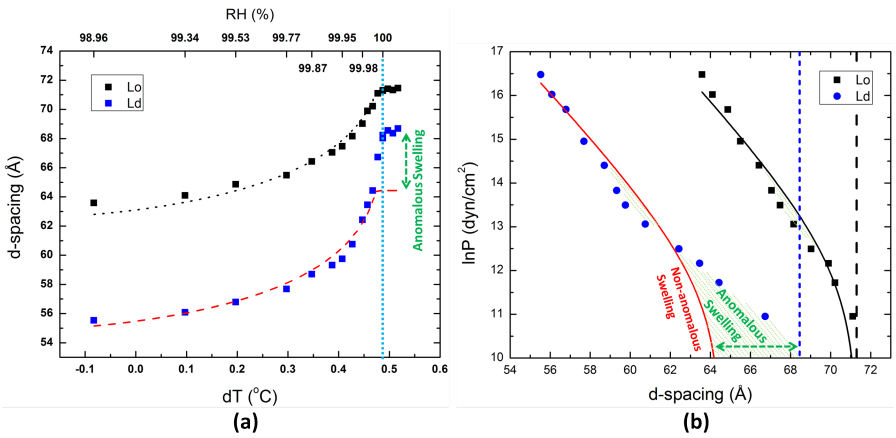

Figure 5.7: The simulated normal swelling curves plotted together with anomalous swelling data. (a) The d-spacing vs. RH (dT) plot. The bottom red dashed curve represents the normal swelling curve for the L_d phase, while the top black dotted curve represents the normal swelling curve for the L_o phase. The 100% RH is marked by the vertical blue dotted line. (b) The natural log of the osmotic pressure is plotted vs. d-spacing for the same simulated normal swelling curve and anomalous swelling data. The vertical blue short dashed line marks the saturation d-spacing of the L_d phase, while the black dashed line marks the saturation d-spacing of the L_o phase.

is not displayed on the plot because of the divergent behavior of ln$P$ at 100% RH. It shows clearly how the data of the L_d phase deviates from the normal swelling curve when the system approaches full hydration.

In order to differentiate from the thermal anomalous swelling discovered by Hønger et al. [82] the gel-fluid phase transition, we may call this phenomenon anomalous swelling type II. This swelling only occurs with phase separated mixture multilayers which have hydrophobic mismatches at the domain boundaries. Comparing with normal swelling, the difference in the d-spacings between the two phases is reduced from 7Å to 3Å with anomalous swelling type II.

5.5 Discussion

To better visualize the anomalous swelling type II, we look back to the schematic drawing in Figure 5.1. Figure 5.1 (a) represents the 99% humidity structure when the water layer thicknesses for both phases are $\sim$ 8Å. The water

forms a continuous layer between the two phases to eliminate the hydrophobic mismatch energy, but the two phases will go out of phase fairly quickly, and the domain boundary has to re-adjust itself in the form of defects or extra bending with associated lipid tilt. In either form, this costs energy. The cost of energy is directly proportional to the thickness of the water layer: as RH increases, the water layer swells, therefore more mismatch energy builds up. This would explain the deviation of data from the simulation curve at $\ln P = 13.5 dyne/cm^2$ in Figure 5.7 (b) in both the L_d and the L_o phase, as the system is trying to reduce the free energy by suppressing the swelling. After a certain point, the mismatch energy is too big and the swelling cannot be suppressed further, the system has to restructure to reduce the free energy, and thus the anomalous swelling in the L_d phase appears. We can see that in Figure 5.1 (b), the excess swelling of the L_d phase would close the gap between the d-spacing differences, therefore effectively reducing the mismatch energy at the domain boundary. (A brief calculation of the boundary hydrophobic mismatch energy as a function of d-spacing difference is included in the supplementary material.)

As shown in the microscope pictures in Figure 5.3, the in-plane domain sizes are on the order of $100\mu m$, which are very large domain areas. The fact that we observe only a single value of the d-spacing for each phase in the anomalous swelling state rather than a super-position of a range of d-spacings shows that the boundary effects on the swelling are quite long-range.

5.6 Materials and Methods

5.6.1 I. Materials

$1,2-dipalmitoyl-sn-glycero-3-phosphocholine$ (DPPC), $1,2-dioleoyl-sn-glycero-3-phosphocholine$ (DOPC) were purchased from Avanti Polar Lipids, Inc. (Alabaster, AL, USA). Cholesterol was purchased from Sigma Chemicals (St. Louis, MO, USA). The chemicals were used without further purification. The phospholipids and cholesterol were mixed in the desired proportions (1:1 DOPC:DPPC with 16% cholesterol) dissolved in chloroform and Tetrafluo-

roethylene (TFE) 1:1 mixture solvent [18], with a final concentration of $8mg/mL$.

Silicon substrates were cut to 17 mm by 20 mm wafers, sonicated for 15 min in methanol, 15 min in miliQ water, nitrogen dried, followed by 15 min UV cleaning under a UV lamp to make the surface hydrophilic. The prepared substrates were placed on a carefully leveled platform for lipid deposition. $150\mu L$ of lipid solution were deposited on each substrate and immediately covered by a large Petri dish for slow evaporation in the fume hood. $3 \sim 4$ hours later, the samples were transferred to a vacuum chamber for 36 hours to remove any remaining traces of solvent. After removing from the vacuum, the samples were placed in humidity chambers with 96% relative humidity (RH) at $50°C$ to incubate for 2 days.

After they had cooled down to room temperature, the samples would phase separate into 2 different phases and interlayer domains would register across bilayers [25]. This registering process takes a few days to complete under partial hydration, but is much faster at 100% RH. The diffraction measurements were taken after the registering process was mostly complete.

5.6.2 II. X-ray diffraction and humidity control

The X-ray measurements were taken on the diffractometer at sector 33 BM at the Advanced Photon Source, Argonne National Laboratory with a 20 keV X-ray beam. Data were taken with a Pilatus 100K photon-counting area detector, which was kept at a fixed position while the sample was rotated for diffraction measurements.

The humidity chamber used was described in our previous research [53]. The chamber uses fine control of the temperature between the reservoir and the sample to control sample humidity. The chamber is extremely accurate at close to 100% RH, as demonstrated in our previous paper and also in this work. By translating the calibrated temperature differential dT to RH, we get the RH reading for our work here. Microscope measurements and d-spacing measurements at RH saturation both prove the accuracy of the method.

Table 5.1: Simulation parameters of the non-anomalous swelling curves of L_d phase and L_o phase.

	A_{fl} $(10^6 dyn/cm^2)$	λ_{fl} (Å)	A_h $(10^9 dyn/cm^2)$	λ_h (Å)	H $(10^{-14} erg)$	$D_B^{'}$ (Å)
L_d	6.46	5.8	0.67	2.0	4.82	48.0
L_o	0.25	6.0	0.69	2.0	2.03	55.4

5.7 Supplementary Materials

5.7.1 Simulation parameters of the non-anomalous swelling curves

See Table 5.1.

5.7.2 Optical, bright field and fluorescence microscopy pictures of domains

See Figure 5.8.

5.7.3 Calculation of the mismatch energy

The following amounts to a simplified model to account semi-quantitatively for the effects of domain wall mismatch.

1. Approximate the hydrophilic-hydrophobic periods as rectangular waves, as shown in Figure 5.9. Give hydrophilic part (head + water + head) the value one, and the hydrophobic part (tail) value zero. The blue rectangular wave fd simulates the periods for L_d phase, while the red dotted rectangular wave f_o simulates the periods for the L_o phase, which has slightly longer chains. We assume that there is a constant mismatch energy of λ per unit length when the hydrophilic regions of one phase overlap with hydrophobic regions of the other phase, and zero otherwise.

Define d as the d-spacing, dt as the tail region thickness, dw as the hydrophilic region thickness (head + water + head), so that $d_w + d_t = d$. The numbers taken for Figure 5.9 are from 99% RH, where $d = 55.5$Å is the d-spacing

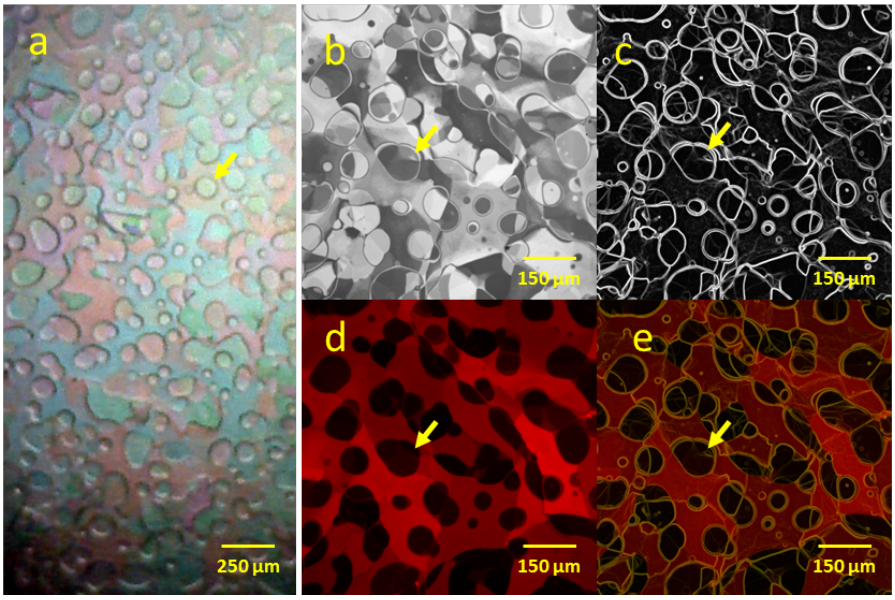

Figure 5.8: The correlation between optical microscopy, bright field microscopy and fluorescence microscopy pictures of phase separated ternary mixture lipid multilayer domains. After analyzing a large number of fluorescence microscopy images and bright field images, we found that the surface morphology, e.g., edges and heights, had a strong correlation with the domain distribution. DiI16 fluorescence dye was used in the fluorescence microscopy sample in the above image (d), which preferentially partitions into the L_d phase. DiIC18 and β-BODIPY fluorescence dyes were also used in our fluorescence microscopy studies to confirm the identification of phases. The edges in the bright field images are mainly correlated with the phase boundaries of the L_o and L_d domains; furthermore, the higher height regions of the sample surface are mostly correlated with the L_o rich regions and the lower height regions (concaves) are mostly correlated with the L_d rich regions. Figure shows optical microscope image (a), bright field image (b) and fluorescence microscope image (d) of the same sample with 16% cholesterol. (c) is the differential calculation of (b), which shows the edges of surface morphology. Overlapping (c) with the fluorescence image from (d), we obtain the image shown in (e). In this overlapped image, we can clearly see this strong correlation.

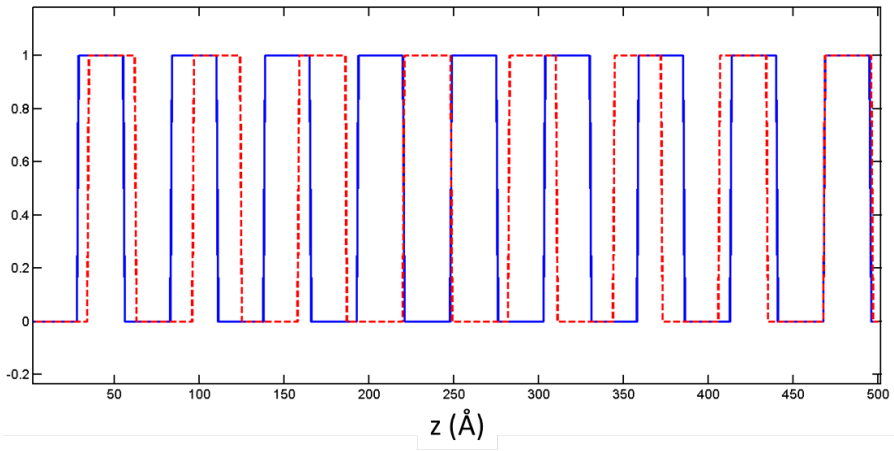

Figure 5.9: Rectangular wave simulation of hydrophilic-hydrophobic periods of both the L_d phase (blue) and the L_o phase (red). Value one represents hydrophilic, while value zero represents hydrophobic.

for the L_d phase, $d = 63.6$Å is the d-spacing for the L_o phase. $d_t = 28.5$Å is the tail region thickness for the L_d phase, $d_t = 34.7$Å is the tail region thickness of the L_o phase. These parameters remain constants with RH.

2. Calculation of mismatch energy:

$$\Delta E = \lambda \int_0^L dz \, [f_d(1 - f_o) + f_o(1 - f_d)] = \lambda \int_0^L dz \, [f_d + f_o - 2f_d f_o] \tag{5.8}$$

Fourier expand f_d, f_o as

$$f = \frac{1}{2}a_o + \sum_{n=1}^{\infty} a_n cos\left(\frac{2\pi}{d} nz\right) \tag{5.9}$$

where

$$a_o = \frac{4d_w}{d}, \tag{5.10}$$

$$a_n = \frac{2}{d} \int_{-d/2}^{d/2} f(z) cos\left(\frac{2\pi}{d} nz\right) dz. \tag{5.11}$$

So the mismatch free energy can be calculated as

$$\Delta E = \lambda \Bigg\{ L\left[\frac{2d_w}{d} + \frac{2d_w^{'}}{d^{'}} - \frac{8d_w d_w^{'}}{dd^{'}}\right] - \frac{2}{\pi^3}\sum_{n,n^{'}=1}^{\infty} \frac{(-1)^{n+n^{'}}}{nn^{'}} sin\left(\frac{2\pi n}{d}d_w\right) sin\left(\frac{2\pi n^{'}}{d^{'}}d_w^{'}\right) \left[\frac{sin\left(2\pi\left(\frac{n}{d}+\frac{n^{'}}{d^{'}}\right)L\right)}{\left(\frac{n}{d}+\frac{n^{'}}{d^{'}}\right)} + \frac{sin\left(2\pi\left(\frac{n}{d}-\frac{n^{'}}{d^{'}}\right)L\right)}{\left(\frac{n}{d}-\frac{n^{'}}{d^{'}}\right)}\right]\Bigg\} = \lambda\{f_1 + f_2\} \tag{5.12}$$

where

$$f_1 = L\left[\frac{2d_w}{d} + \frac{2d_w^{'}}{d^{'}} - \frac{8d_w d_w^{'}}{dd^{'}}\right] \tag{5.13}$$

$$f_2 = -\frac{2}{\pi^3}\sum_{n,n^{'}=1}^{\infty} \frac{(-1)^{n+n^{'}}}{nn^{'}} sin\left(\frac{2\pi n}{d}d_w\right) sin\left(\frac{2\pi n^{'}}{d^{'}}d_w^{'}\right) \left[\frac{sin\left(2\pi\left(\frac{n}{d}+\frac{n^{'}}{d^{'}}\right)L\right)}{\left(\frac{n}{d}+\frac{n^{'}}{d^{'}}\right)} + \frac{sin\left(2\pi\left(\frac{n}{d}-\frac{n^{'}}{d^{'}}\right)L\right)}{\left(\frac{n}{d}-\frac{n^{'}}{d^{'}}\right)}\right] \tag{5.14}$$

According to the above equations, we can simulate the mismatch free energy for $L = nd \approx n^{'}d^{'}$. See Figure 5.10 for $n = 10$ and 7.

Note that the relative humidity increases from right to left of x-axis, as $\ln P$ decreases. The data for $\ln P < 10$ are really the data for 100% RH, where $\ln P$ goes to negative infinity, therefore these $\ln P$ are nominal labels just for plotting. In the simulation, we can see that the oscillation term f_2 contributes in the overall mismatch energy, and lowers the anomalous swelling mismatch energy. In the 7 bilayer case (Figure 5.10 (b, d)), the energy of the anomalous swelling is mostly lower than the normal swelling. This because with low number of bilayers, the anomalous swelling caused the two periods to go out of phase slower (takes more

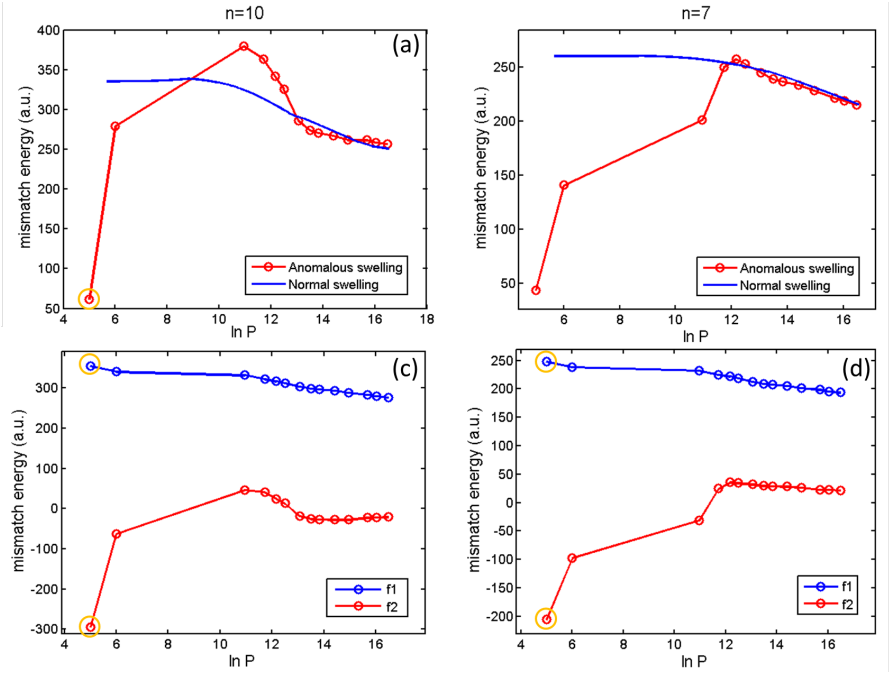

Figure 5.10: Simulated mismatch energy with 10 bilayers (a, c) and 7 bilayers (b, d). (a, b) are plotting $(f_1 + f_2)$ vs. $\ln P$ for anomalous swelling (red) and normal swelling (blue). The normal swelling curve is simulated with the normal swelling d-spacings as shown solid curve in Figure 5.7 (b). The anomalous swelling curve is simulated with the anomalous swelling experimental d-spacings shown as the data points in Figure 5.7 (b). (b, d) are plotting the breakdown of f_1 and f_2 for the anomalous swelling in (a, b). The left most point circled in yellow is again the simulated data of $d = d^{'} = 71.5$Å, which is not an actual data point.

bilayers) than the normal swelling case, therefore lowers the energy. The simulation suggests that system needs to re-adjust its periods every 7 layers or so to lower the energy.

5.8 Acknowledgments

X-ray data were collected on beamline 33BM at the Advanced Photon Source, Argonne National Laboratory. Use of the Advanced Photon Source was supported by the U. S. Department of Energy, Office of Science, Office of Basic Energy Sciences, under Contract No. DE-AC02-06CH11357.

This work was supported by the Office of Basic Energy Sciences, U.S. Dept.

of Energy under DOE Grant number: DE-FG02-04ER46173.

I would like to acknowledge my co-authors Sajal K. Ghosh, Sambhunath Bera, Zhang Jiang, Christian M. Schleptz, Evguenia Karapetrova, Laurence B. Lurio and Sunil K. Sinha for the work in this chapter.

6 X-ray Studies of Domain Growth Kinetics

6.1 Overview

Phase separated mixture lipid multilayers form domains registering across multiple bilayers via interlayer coupling. In this study, we investigated the kinetics of domain growth of supported multilayers consisting of 1:1 $1,2-dipalmitoyl-sn-glycero-3-phosphocholine$ (DPPC): $1,2-dioleoyl-sn-glycero-3-phosphocholine$ (DOPC) with different cholesterol concentrations under partial hydration using X-ray diffraction and diffuse scattering. Domains appear after a rapid temperature quench, when the multilayers are cooled through a miscibility phase transition such that coexisting phases form. From our X-ray rocking curve patterns, we identified two separate components representing the registered domain and the domain boundary respectively. After nucleation, the domains would progress into a coarsening stage that follows logarithmic growth rather than the commonly seen power law growth, which is both evident in diffraction measurements and diffuse measurements. This logarithmic growth we observed can be related to domain interfacial energy under partial hydration conditions.

6.2 Introduction

Lipid membranes present rich dynamics in water environments. The domain growth kinetics of liquid domains has been measured using giant unilamellar vesicles (GUVs) by Stanich et al. [90] and also compared with both established

and recent predictions [91, 92, 93, 94, 95, 96, 97]. In their study, after a quench to constant temperature, the domain coarsening process was recorded with florescence microscopy. For samples far away from critical composition, a power law with a growth exponent 1/3 is obtained for non-critical compositions, which agrees well with theoretical predictions for domain growth via collision and coalescence for 2-dimentional (2D) diffusion. They also obtained a growth exponent 1/2 for critical composition samples, which is also consistent with theories of critical phenomena and simulation. Due to the bulk water environment, the kinetics is fairly fast with a time scale of hundreds of seconds.

In our previous study of supported multilayer domain registration [25], we also observed power law growth with a growth exponent of 0.46 for submerged supported multilayer samples under water, observed with fluorescence microscopy. The time scale of hundreds of seconds was comparable to the vesicle studies by Stanich et al. [90] due to the bulk water environment.

Different from the domain growth in a GUV, the domains in a supported multilayer grow 3-dimentionally (3D), both in-plane and out-of-plane due to interlayer coupling. Due to the added interaction in the third dimension, it is possible that the growth law can be different from the 2D diffusion case. In order to investigate the kinetics of domain growth in multilayer systems with detailed measurements using X-ray scattering technique, we kept the samples under partial hydration conditions to slow down the kinetics. By using by a saturated salt solution as the reservoir, the samples were partially hydrated with $\sim 96\%$ relative humidity (RH). The kinetics were dramatically slowed down compared to the bulk water condition, resulting in a time scale of hours to several days, which enable a detailed measurement of X-ray diffraction and diffuse scattering at each state.

Contrary to all literature on lipid domain dynamics, we discovered a logarithmic growth for our partially hydrated multilayer domains after the domains nucleate. The discovery is consistent for different cholesterol concentration samples, with a consistently shifting time scale window due to added cholesterol. Although not as commonly seen in biomaterials, the logarithmic growth has been both theoretically predicted, simulated and experimentally verified in ferromagnetic systems

with degenerate phases [98, 99, 100, 101, 102, 103, 104, 105]. The predictions were made using scaling arguments based on the energetics of a single interface, where scale-dependence of energy barriers and interfacial roughening due to the disorder were considered [100]. In our system, we certainly have energy barriers and disorder at the domain interface. The X-ray diffuse scattering results which reveal the disorder in the domain boundaries will be presented in the results section. Hopefully the experimental evidence presented in this work would be helpful for detailed model development in the future for soft matter systems.

6.3 3. Materials and Methods

6.3.1 Sample preparation

$1,2-dipalmitoyl-sn-glycero-3-phosphocholine$ (DPPC) and $1,2-dioleoyl-sn-glycero-3-phosphocholine$ (DOPC) solutions were purchased from Avanti Polar Lipids, Inc. (Alabaster, AL, USA) with accurate concentrations of the lipids specified. Cholesterol was purchased from Sigma Chemicals (St. Louis, MO, USA). All the purchased chemicals were used without further purification. The phospholipids and cholesterol were mixed in the desired proportions and dissolved in a chloroform and Tetrafluoroethylene (TFE) 1:1 mixture solvent [18], to yield a final concentration 8 mg/mL.

Silicon substrates, cut to 17 mm by 20 mm wafers, were first sonicated for 15 min in methanol followed by another 15 min in deionized water (miliQ, 18 $MOhmcm^{-1}$). Substrates were then nitrogen-dried, and exposed to short-wavelength UV radiation for $\sim$ 15 min to make the surface hydrophilic. The prepared substrates were then placed on a carefully leveled platform for lipid deposition. 150 μL of lipid solution were deposited on each substrate and covered by a large Petri dish for slow evaporation in the fume hood. After $3 \sim 4$ hrs, the samples were transferred to a vacuum chamber for 36 hrs to remove remaining traces of solvent. After removing from the vacuum, the samples were placed in humidity chambers maintained at 96% relative humidity (RH) at $50°C$ and incubated for 48 hrs.

Subsequently, the samples are cooled to room temperature at the ambient rate. Consistent with our earlier findings, equilibration of phase separating lipid mixtures involves thickness-dependent lateral coarsening of the domains and interlayer domain registration producing a columnar mesophase [25]. Although elaborate, the procedure above ensures reproducibility producing high quality of samples as reflected by the observations of up to the 9th order of diffraction peaks with an in-house X-ray tube source. A sample set consisting of a fixed 1:1 DPPC: DOPC ratio containing systematically varied molar fraction cholesterol (0%, 10%, 16%, 20%, 25%, 30%) were prepared (e.g., for the 16% cholesterol sample, the composition is 42% : 42% : 16% DPPC : DOPC : cholesterol in molar ratio) and characterized. The structural studies of the same sample set has been reported in our previous work [106].

6.3.2 Temperature quenches and repeatability

The sample temperature control system contains a heating element and a Julabo water circulation system to ensure both fast heating up and cooling down. A temperature change of $25 \sim 30^{\circ}C$ typically takes $10 \sim 15$ min including temperature equilibration. This temperature quench rate is adequate comparing to the time scale of domain coarsening, which is on the order of hours to days. An in-house X-ray spectrometer with a $Cu-K_{\alpha}$ tube source is used for all the measurements. Before the X-ray measurements, each sample was loaded and equilibrated at $50^{\circ}C$ (homogenous phase) for the 96% RH measurement chamber for more than 5 hours to ensure sample homogeneity. The homogenous phase was measured with X-rays as the reference during this time. After equilibration, the set temperature was dropped to bellow the sample phase transition temperature, typically $25^{\circ}C$, and continuous X-ray measurements were carried out from the time of temperature change until the domain growth finished. Each experimental sequence took about a week, and both diffraction and diffuse scattering (rocking curves) were measured for each time point. All samples were quenched to room temperature ($\sim 25^{\circ}C$), except for the sample containing 30% cholesterol, which was quenched to $11^{\circ}C$ due to a much lower phase transition temperature of this specific mixture ($\sim 20^{\circ}C$) ,

as shown by Mills et al. [52].

Both temperature cycle repeatability and sample dependency repeatability were tested using samples with 16% cholesterol before doing the whole concentration set: for temperature cycle repeatability, 3 runs with the same piece of sample were tested; for sample dependence repeatability, 3 runs with 3 different pieces of sample were tested. All results were reproducible.

6.4 Results

6.4.1 Decomposition of X-ray diffuse scattering

Rocking curves were measured for all samples at regular time intervals. Figure 6.1 shows a typical example of set of rocking curves for a sample with 16% cholesterol at different stages of domain growth for both the liquid ordered phase (L_o) and the liquid disordered phase (L_d). The rocking curve intensities can be well fitted by the sum of two Lorentzians to the 3/2 power: I_1 one for the center sharp peak, and I_2 for the board background:

$$I = I_1 + I_2 \tag{6.1}$$

where

$$I_1 = \frac{A_1}{\left(1 + (q - qc_1)^2 \left(\frac{2\pi}{w_1}\right)^2\right)^{3/2}} \tag{6.2}$$

$$I_2 = \frac{A_2}{\left(1 + (q - qc_2)^2 \left(\frac{2\pi}{w_2}\right)^2\right)^{3/2}} \tag{6.3}$$

where the power of 3/2 comes from the dimentionality of domains in 3D [107].

From the figure we can see that with time (from top to bottom), the center sharp peak in red grows while the broad green peak decreases for both of the phases. By fitting rocking curves for the whole time sequence, we can extract

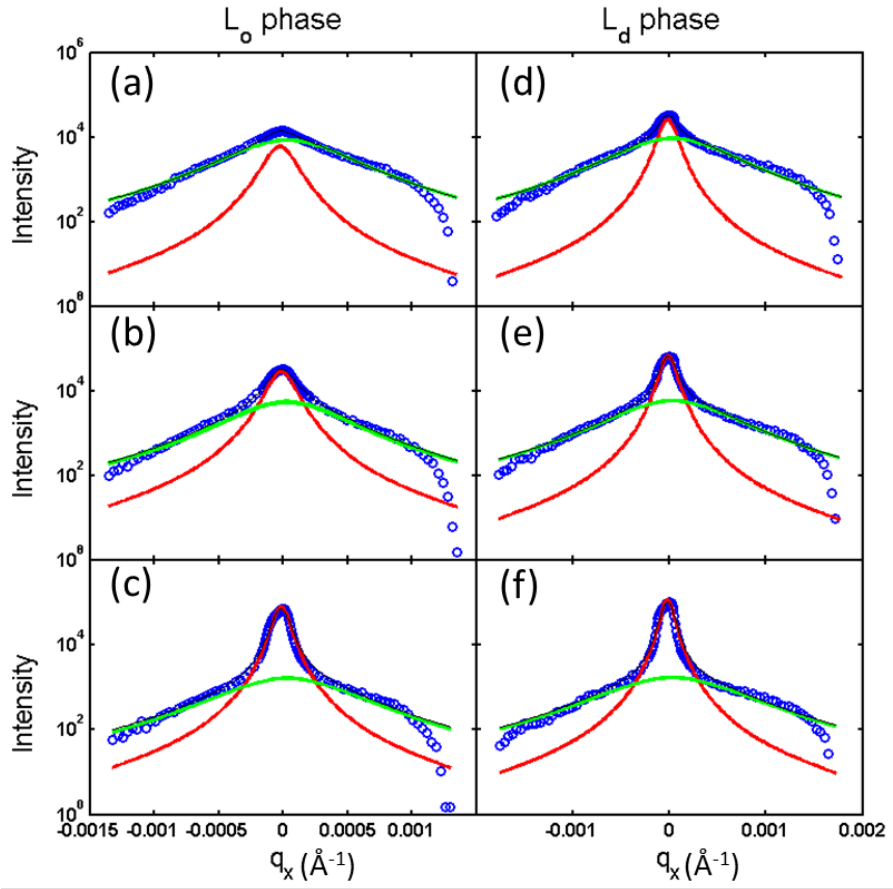

Figure 6.1: Rocking curves of 16% cholesterol for both liquid phases at different stages of domain growth. Left column (a, b, c) are rocking curves measured when 2θ angle fixed on the Bragg condition of the d-spacing corresponding to the L_o phase, while the right column (d, e, f) are for the L_d phase. Top two plots (a,d) are rocking curves at the beginning stage of domain growth ($\sim$ 30 min after the temperature quench), middle two plots (b, e) are the middle stage ($\sim$ 12 hrs after the temperature quench), while the bottom two plots (c, f) are the finishing stage when domain growth mostly completed after $\sim$ 100 hrs. The rocking curves are fitted with the sum of two Lorentzians to the 3/2: a sharp peak in the center in red and a broad peak in green. The sum is the thin black line across the data points.

quantitative parameters of peak height and width of the two components. Figure 6.2 plots the A_1 and A_2 vs. time.

After temperature quench at time zero, the system breaks off from the homogenous phase and phase separates into two co-existing liquid phases. In both phases, the amplitude for the center sharp peak A_1 exponentially saturating according to the form $b[1 - exp(-at)]$ with time, while the amplitude for the broad background peak A_2 exponentially decreases. The green arrow points to a discontinuity corresponding to the green arrows in Figure 6.3, which will be discussed in details later. It is essential to understand the origin for the two peaks in order to understand the domain growth kinetics. The center sharp peak is essentially the multilayer Bragg peak, which reflects the portion of the registered domains. The width of the peak is a measure of the in-plane domain size, as the domain size is proportional to the inverse of the peak width. After quenching, the registered domains increase in number and also grow larger, so the peak grows taller and narrower. On the other hand, the broad background peak can come from various sources, such as interfacial roughness, mosaic or defects. By looking at the time dependence of this peak, we think it is very much likely related to the domain boundary. We will come back to this point shortly when showing the peak widths change with time.

The exponential fit was adequate to describe the overall trend of the intensity change, but does not fit well for the intermediate time range (eg. 1000 min $\sim$ 3000 min). We will demonstrate that a logarithmic time fit yields much better and consistent fitting for all parameters. Figure 6.3 shows logarithmic plots of both peak height A and peak width w for both phases.

In linear vs. log(t) plots in Figure 6.3, we can clearly see two time regimes: one immediately following the temperature quench, most likely exponential as suggested in Figure 6.2 linear plot, and transition into the logarithmic growth regime after $\sim$ 400 min. This transition is both evident as a sudden slope change in A_1 and w_1 in Figure 6.3 (a, c). We will call this transition time T_a. The transition time of the L_o phase is marked by the vertical dotted yellow line and the green arrow. Before the transition time T_a, the peak intensity A_1 increases while the

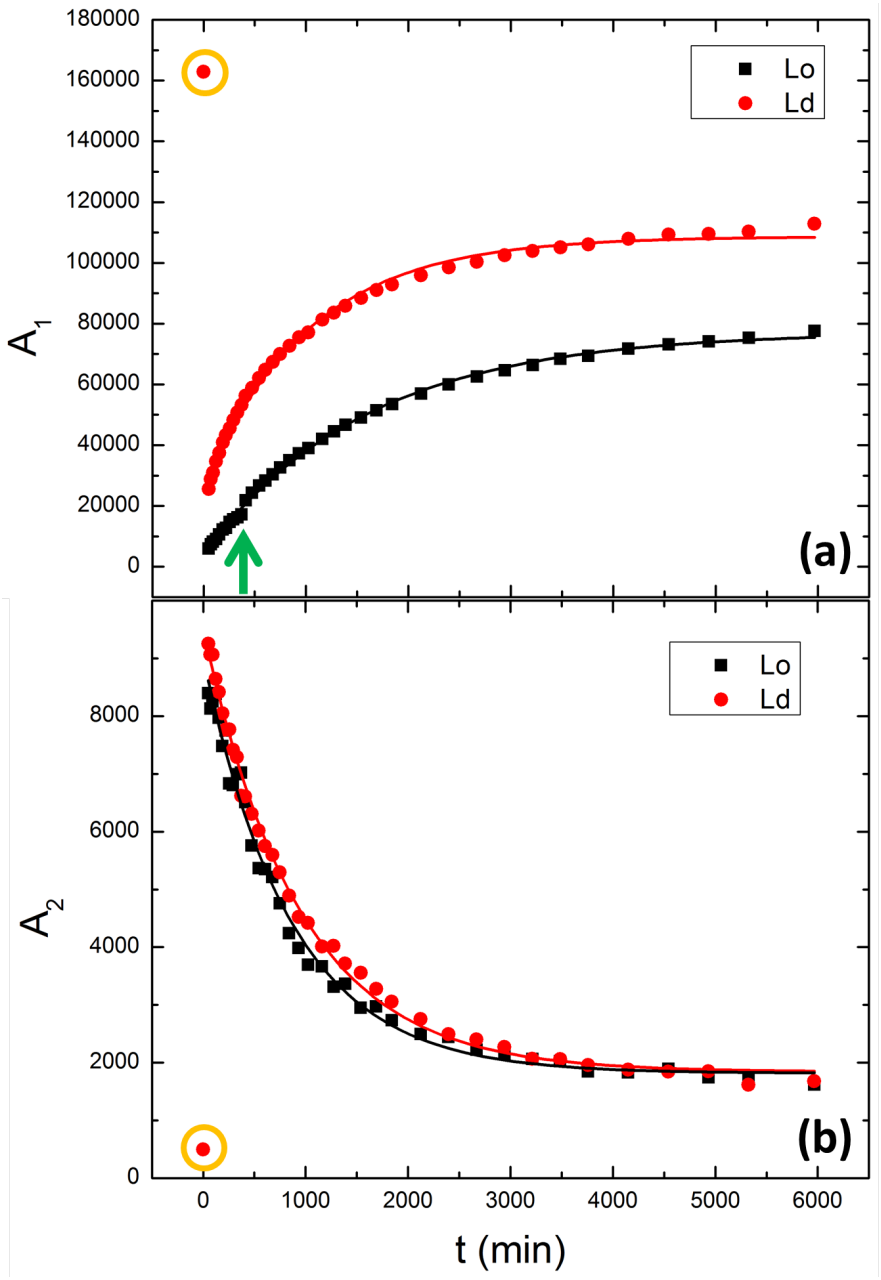

Figure 6.2: Rocking curve component A_1 (a) and A_2 (b) vs. time linear plot for 16% cholesterol sample. L_o phase is marked by the black squares, while the L_d phase is marked by the red circles. The data is fitted with exponentials, as marked by the solid curve across the points. The first dot at time zero circled with yellow is the fitted amplitude for the homogenous phase at $50°C$ for comparison.

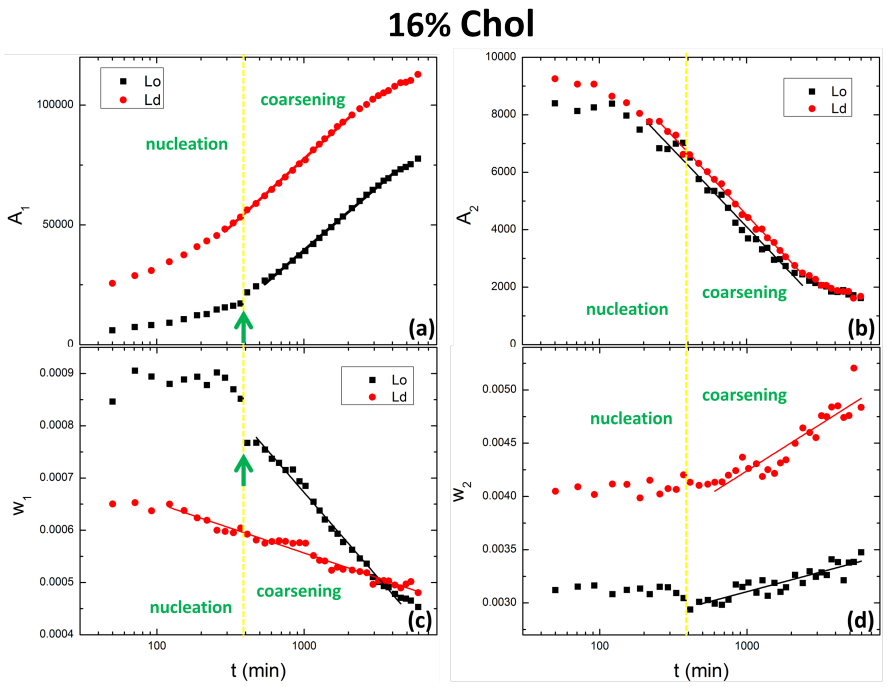

Figure 6.3: Fitted peak amplitude and width vs. log(t) for rocking curves of 16% cholesterol sample n=1 Bragg peaks. A_1, w_1 (a, c) are amplitude and width for the strong sharp peak, while A_2, w_2 (b, d) are amplitude and width for the broad background peak. The vertical dotted line marks the time when domain growth transition from nucleation stage to coarsening stage. Logarithmic fits are shown as the solid straight lines across data points.

peak width w_1 changes very little. Since this main peak reflects the registered domains, we can infer that during this time, the domains are in a nucleating stage, while domains form locally, and the number of domains increases. After T_a, the small local domains are already formed, and domains start to coarsen by collision and coalesce. This coarsening stage can be fitted very well by a logarithmic time fit for both peak intensity and width.

In plots for the broad peak, Figure 6.3 (b, d), the same transition time T_a is marked with a yellow line for reference. We can see the logarithmic growth regime starts roughly around the same T_a as well for A_2 and w_2. The intensity of the peak decreases in both nucleation and coarsening stage, while the width of the peak stays the same for the nucleation stage and increases in the coarsening stage. This means the origin of the broad peak mainly gets fewer in the nucleation stage, while also getting smaller during domain coarsen. This behavior suggests that the origin might be associated with the domain boundary curvature or defects, since the total domain boundary decreases with domain growth, and also the domain boundary can become sharper as domains register better.

Other possible sources of a broad background peak, like mosaic, do not really change the width with time. Also, it is more common for the sample mosaic to decrease by repeated temperature cycles rather than with constant temperature. Interfacial roughness, on the other hand, would result in q-dependent power law tails, which is certainly not the line shape we observed.

6.4.2 X-ray diffraction measurements of growth kinetics

X-ray diffraction measurements are also taken for the same conditions. Because of a much stronger scattering signal, diffraction data can be taken at smaller time scale than diffuse scattering measurements. So besides the nucleation stage and the logarithmic coarsening stage as observed in the rocking curves, we also observed a breaking-order stage close to time zero. See Figure 6.4. After the temperature quench at time zero, the diffraction peak intensity immediately drops as the registration order of the homogenous phase is breaking off by the phase separation, and new phase registration order starts to establish at the same time.

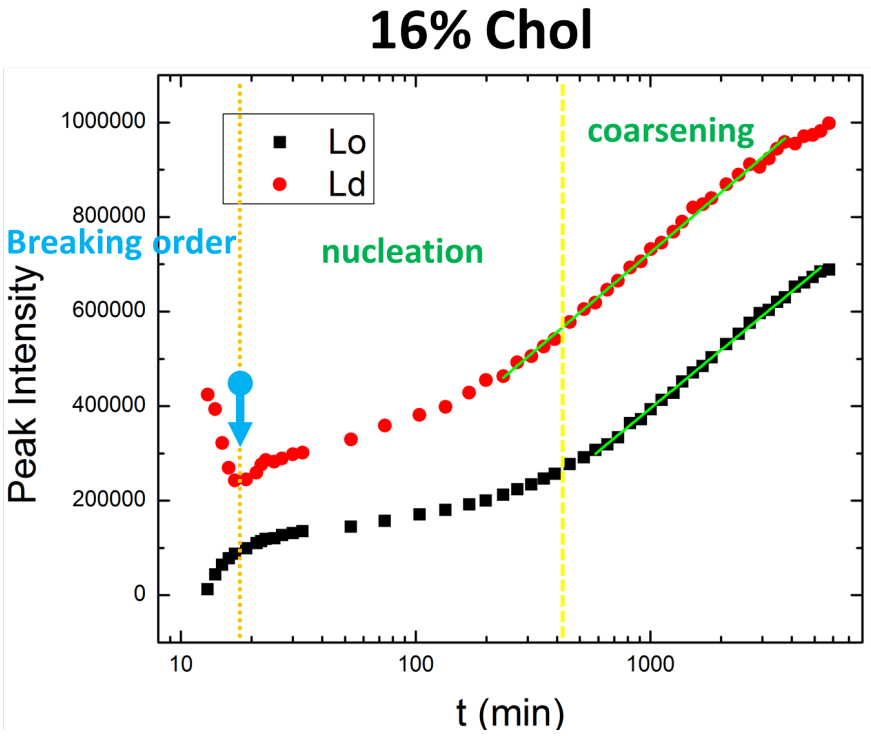

Figure 6.4: X-ray diffraction peak intensity of n = 1 order for 16% cholesterol sample. The vertical orange dotted line and blue arrow marks the transition point between breaking order and re-establishing order immediately after temperature quenching. The vertical yellow dotted line marks the transition time between nucleation stage and coarsening stage. Logarithmic fits for the coarsening phase are represented with the solid lines across data points.

As marked by the orange dotted vertical line and a blue arrow, the L_d phase experiences a turning point as the multilamellar order of the homogeneous phase is destroyed and new order builds up. At the same time, the L_o phase just develops as a new phase.

The transition time T_a as determined from the rocking curve main peak height and width slope in-continuity is also consistent with the time at which the diffraction peak intensity slope changes. In summary, we have observed 3 different stages in domain growth kinetic process for 16% cholesterol: the breaking-order stage, the nucleation stage, and the coarsening stage. The coarsening stage is characterized by logarithmic growth. There is actually a fourth stage, the saturation stage after the coarsening stage, when the process is close to completion. We will

see this stage more clearly in samples with higher cholesterol concentration in the following section.

6.4.3 Cholesterol dependence of the domain growth kinetics

It would be interesting to see how changing in cholesterol content affects the kinetics of domain growth for the phase separated multilayer system, since cholesterol is known to change membrane fluidity [108]. Here we present results for 0%, 10%, 20%, 25% and 30% cholesterol samples, which together with the above reported 16% cholesterol sample, provide us with a nice full picture of how the domain growth kinetics is changed, with the observation time window shifting from earlier stage to later stage with increasing cholesterol content.

0% cholesterol

With 0% cholesterol, the system phase separates into a DPPC-rich gel phase and a DOPC-rich fluid phase. The volume fraction for the gel phase is less than the fluid phase, which can be determined from the late stage peak intensity ratio. The kinetics for the gel phase is very slow, as it enters the coarsening phase ∼17 hrs after the temperature quench (Figure 6.5 (a, c)). From peak width in (c), we see that the domain size for the gel phase is significantly larger after entering the coarsening phase.

At transition time T_a, a discontinuous change in the center peak width w_1 is obvious for both phases. It is interesting to see that without cholesterol, the peak intensity from domain boundary curvature/defects follows a logarithmic growth during the entire time window. There can be an indication of a difference made with gel phase comparing to L_o phase for the domain boundary behavior.

Figure 6.6 shows the diffraction peak intensity vs. time. We can see the breaking-order turning point very obviously, as the system is developing very slowly. The logarithmic growth starts much earlier ($\sim$ 400 min) than in the rocking curve width. This could indicate a broad transition range from $\sim$ 400 to 1000 min.

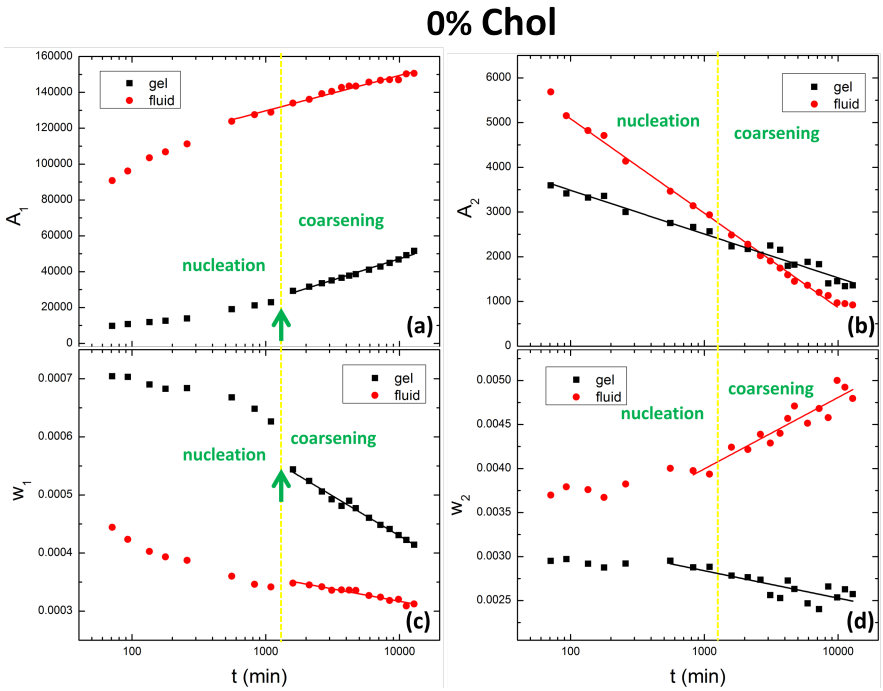

Figure 6.5: Fitted peak amplitude and width vs. log(t) for rocking curves of 0% cholesterol sample n = 1 Bragg peaks. A_1, w_1 (a, c) are amplitude and width for the strong sharp peak, while A_2, w_2 (b, d) are amplitude and width for the broad background peak. The vertical dotted line marks the time when domain growth transition from nucleation stage to coarsening stage. Logarithmic fits are shown as the solid straight lines across data points.

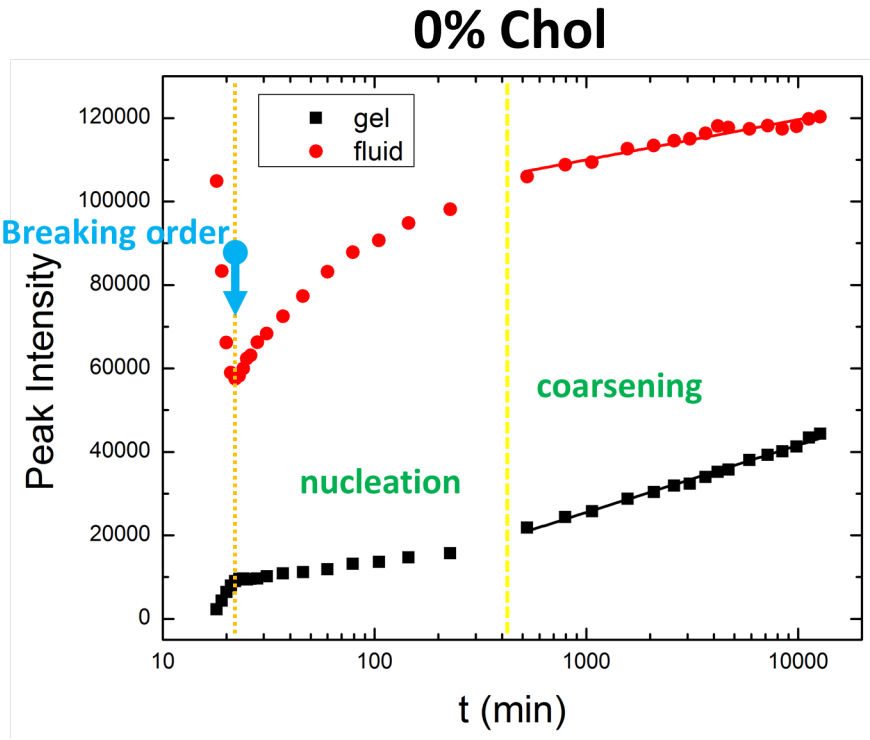

Figure 6.6: X-ray diffraction peak intensity of n = 1 order for 0% cholesterol sample. The vertical orange dotted line and blue arrow marks the transition point between breaking order and re-establishing order immediately after temperature quenching. The vertical yellow dotted line marks the transition time between nucleation stage and coarsening stage. Logarithmic fits for the coarsening phase are represented with the solid lines across data points.

We did not observe the saturation stage during our time window, as the system is so slow that it does not reach saturation even after 8 days.

10% cholesterol

With 10% cholesterol, the DPPC rich phase is right at the boundary of just entering the L_o phase from the gel phase. The Ta is smaller compared to 0% cholesterol, as the sample goes into the coarsening stage at around 600 min from temperature quench (Figure 6.7). The broad peak intensity for the L_o phase behaves unusually at the nucleation stage: instead of going down, it goes up and down again. This can be related to a frustration at the domain boundaries when

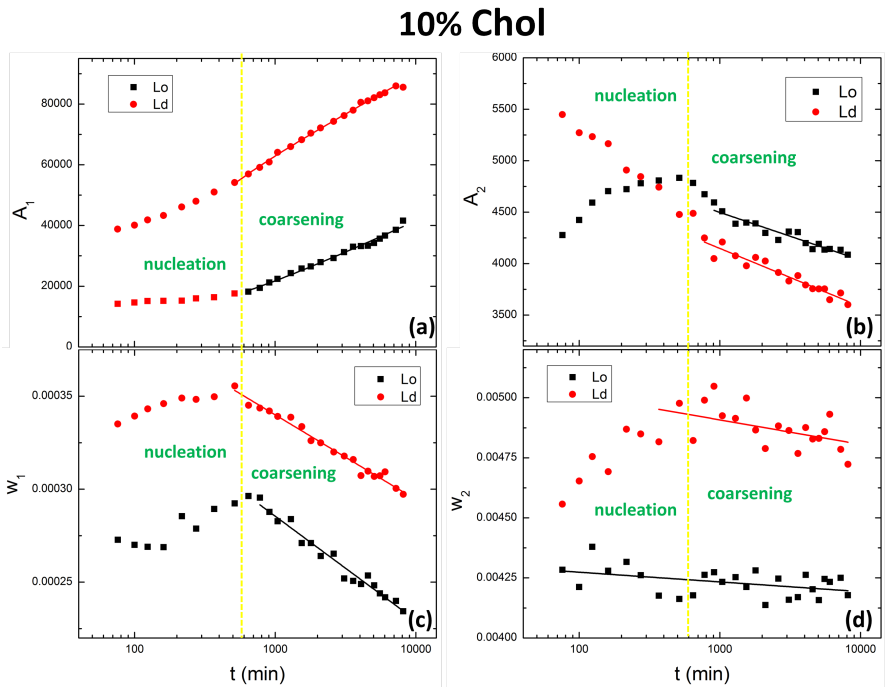

Figure 6.7: Fitted peak amplitude and width vs. log(t) for rocking curves of 10% cholesterol sample n=1 Bragg peaks. A_1, w_1 (a,c) are amplitude and width for the strong sharp peak, while A_2, w_2 (b, d) are amplitude and width for the broad background peak. The vertical dotted line marks the time when domain growth transition from nucleation stage to coarsening stage. Logarithmic fits are shown as the solid straight lines across data points.

sample composition is so close to the gel-L_o transition.

From the diffraction measurements (Figure 6.8) we can also see the breaking order stage, as indicated by the blue arrow. In this cholesterol concentration, the L_o phase also shows an oscillation around the turning point. This was only seen for this concentration.

20% cholesterol

At 20% cholesterol, we no longer see the nucleation phase (Figure 6.9). Due to the increased cholesterol concentration, the kinetics becomes much faster, and the system had already entered the coarsening phase in our time window for measuring the rocking curves. Note that the yellow line marks the stages for one

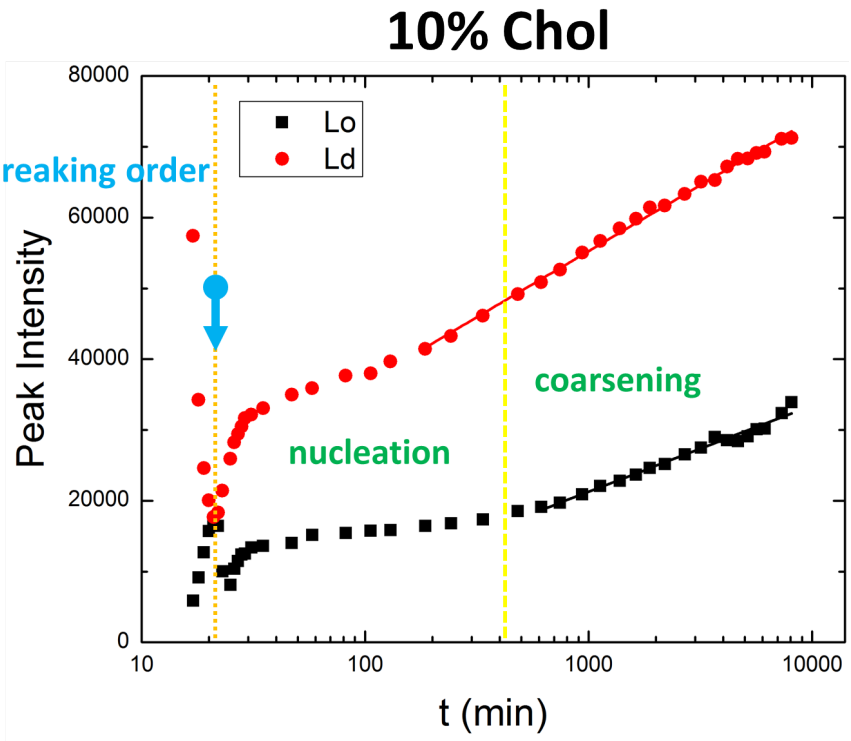

Figure 6.8: X-ray diffraction peak intensity of n = 1 order for 10% cholesterol sample. The vertical orange dotted line and blue arrow marks the transition point between breaking order and re-establishing order immediately after temperature quenching. The vertical yellow dotted line marks the transition time between the nucleation stage and the coarsening stage. Logarithmic fits for the coarsening phase are represented with the solid lines across data points.

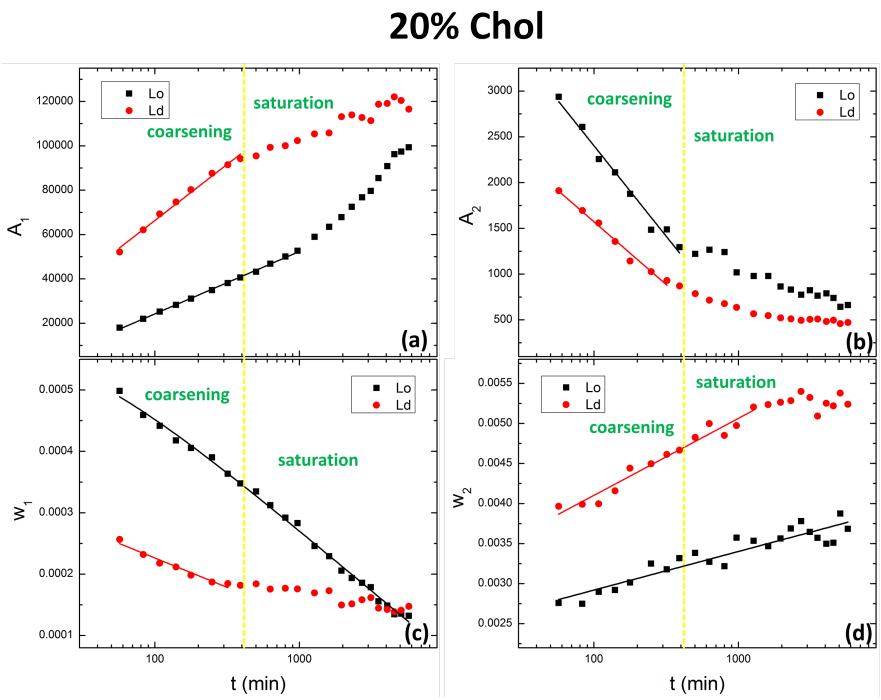

Figure 6.9: Fitted peak amplitude and width vs. log(t) for rocking curves of 20% cholesterol sample n=1 Bragg peaks. A_1, w_1 (a,c) are amplitude and width for the strong sharp peak, while A_2, w_2 (b,d) are amplitude and width for the broad background peak. The vertical yellow dotted line marks the time when domain growth transition from coarsening stage to saturation stage. Logarithmic fits are shown as the solid straight lines across data points.

of the phases when the two phases pace differently. Due to the faster kinetics, we observed the saturation stage, which happens after the coarsening. The transition from coarsening to saturation stage is marked by the vertical yellow dotted line. Well call this transition time T_b, which marks the end of the logarithmic growth. For 20% cholesterol sample, T_b is around 400 min for the L_d phase, and more than 1000 min for the L_o phase. The intensity from the domain boundaries, A_2, also saturates around the same time of T_b.

In the diffraction intensity measurements (Figure 6.10), we can still see the breaking order stage which happens within the first 20 min after the temperature quench. The nucleation stage is quickly passed, almost like it was skipped, and the phases directly go into coarsening. Saturation for the L_d phase is very obvious, while the L_o phase appears not to have saturated during the time window.

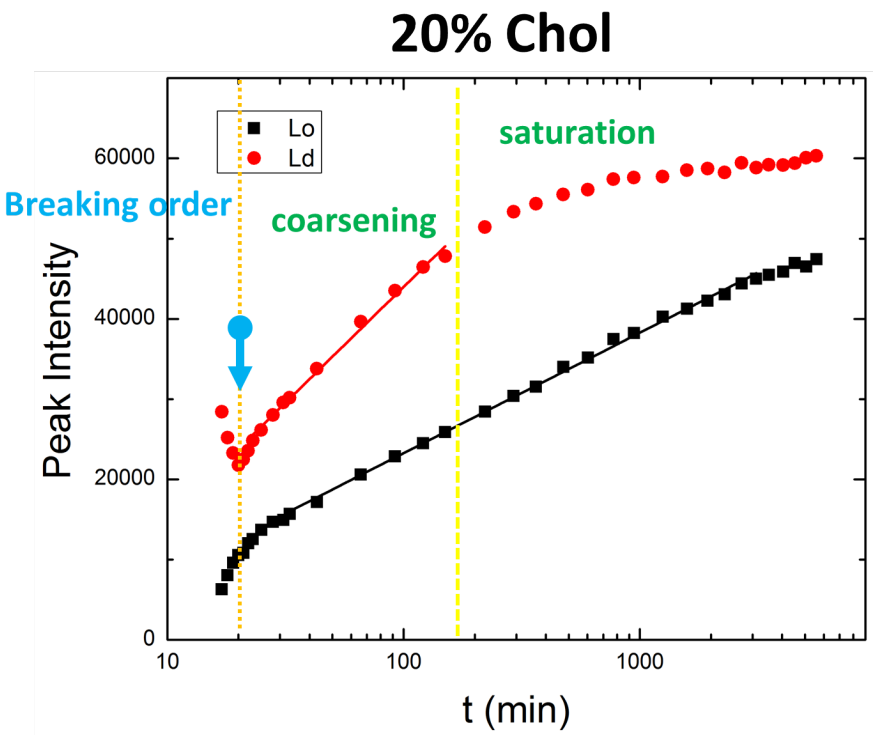

Figure 6.10: X-ray diffraction peak intensity of n = 1 order for 20% cholesterol sample. The vertical orange dotted line and blue arrow marks the transition point between breaking order and re-establishing order immediately after temperature quenching. The vertical yellow dotted line marks the transition time between nucleation stage and coarsening stage. Logarithmic fits for the coarsening phase are represented with the solid lines across data points.

25% cholesterol

At 25% cholesterol concentration, the two phases are behaving the most similar to each other. From Figure 6.11, we can see that the coarsening rates for the two phases are almost the same for the main peak intensities. In the diffraction measurement (Figure 6.12), it is even more obvious that the two curves almost overlap with each other. The phase volumes are mostly equal, so this concentration can be quite close to the critical composition. In rocking curve measurements, we can only see the coarsening and the saturation stage; while in the diffraction measurements we can also see the nucleation stage before 30 min.

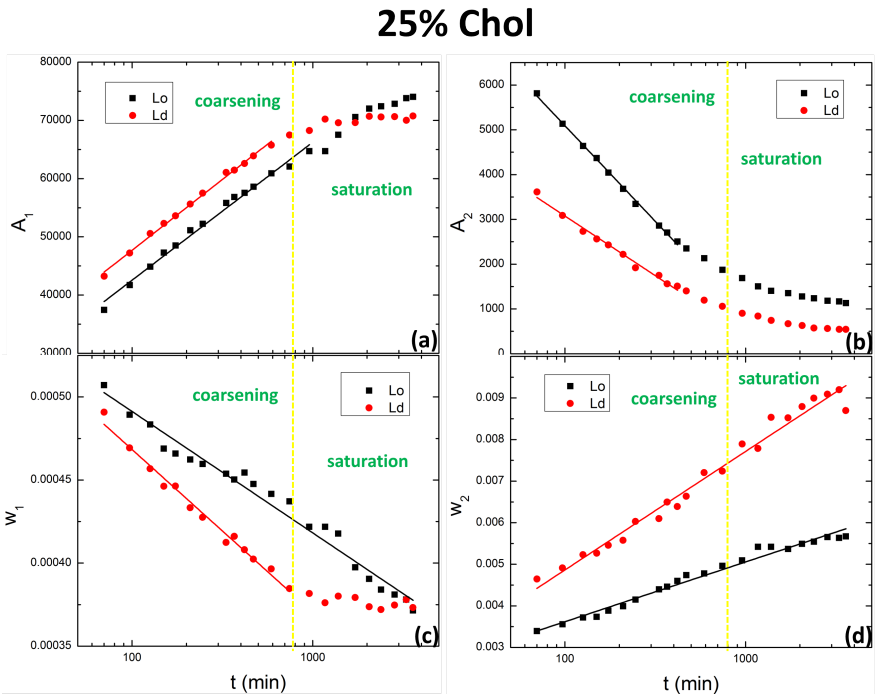

Figure 6.11: Fitted peak amplitude and width vs. log(t) for rocking curves of 25% cholesterol sample n=1 Bragg peaks. A_1, w_1 (a, c) are amplitude and width for the strong sharp peak, while A_2, w_2 (b, d) are amplitude and width for the broad background peak. The vertical yellow dotted line marks the time when domain growth transition from coarsening stage to saturation stage. Logarithmic fits are shown as the solid straight lines across data points.

30% cholesterol

At 30% cholesterol, the phase transition temperature is $\sim 20°C$, which is lower than $25°C$, so the temperature was quenched to $11°C$ for the sample to phase-separate. For this high concentration of cholesterol, the phase volume of L_o phase becomes larger than the L_d phase, as the L_o phase intensity curve is above the L_d (Figure 6.13 (a)). Also the speed of the kinetics is very fast, as the L_o phase saturates at ~ 500 min. The L_d phase become the slower phase, as it becomes the minority phase this time. Also the coarsening and saturation stages were observed in rocking curve measurement time window, while a short nucleation stage was captured with diffraction measurements.

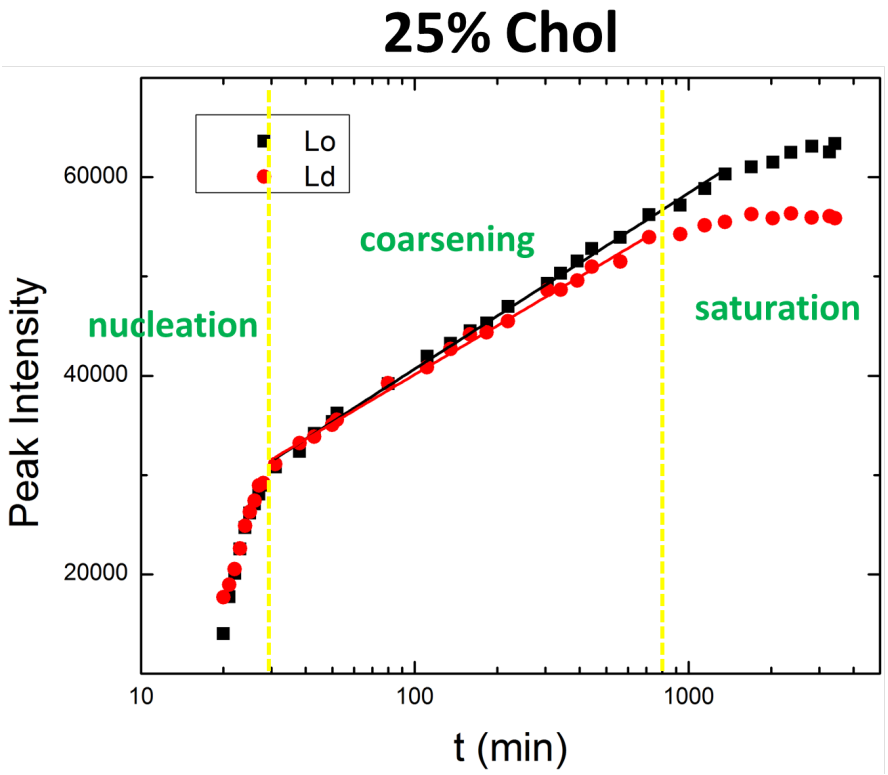

Figure 6.12: X-ray diffraction peak intensity of n = 1 order for 25% cholesterol sample. The vertical yellow dotted lines marks the transition time from nucleation stage to coarsening stage, and coarsening stage to saturation stage. Logarithmic fits for the coarsening phase are represented with the solid lines across data points.

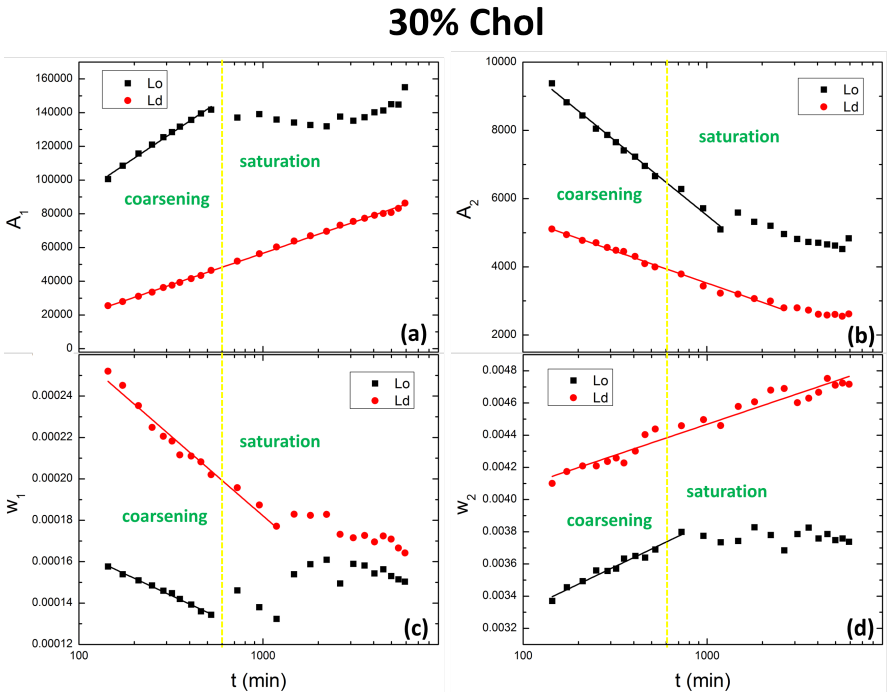

Figure 6.13: Fitted peak amplitude and width vs. log(t) for rocking curves of 30% cholesterol sample n = 1 Bragg peaks. A_1, w_1 (a, c) are amplitude and width for the strong sharp peak, while A_2, w2 (b,d) are amplitude and width for the broad background peak. The vertical yellow dotted line marks the time when domain growth transition from the coarsening stage to the saturation stage. Logarithmic fits are shown as the solid straight lines across data points.

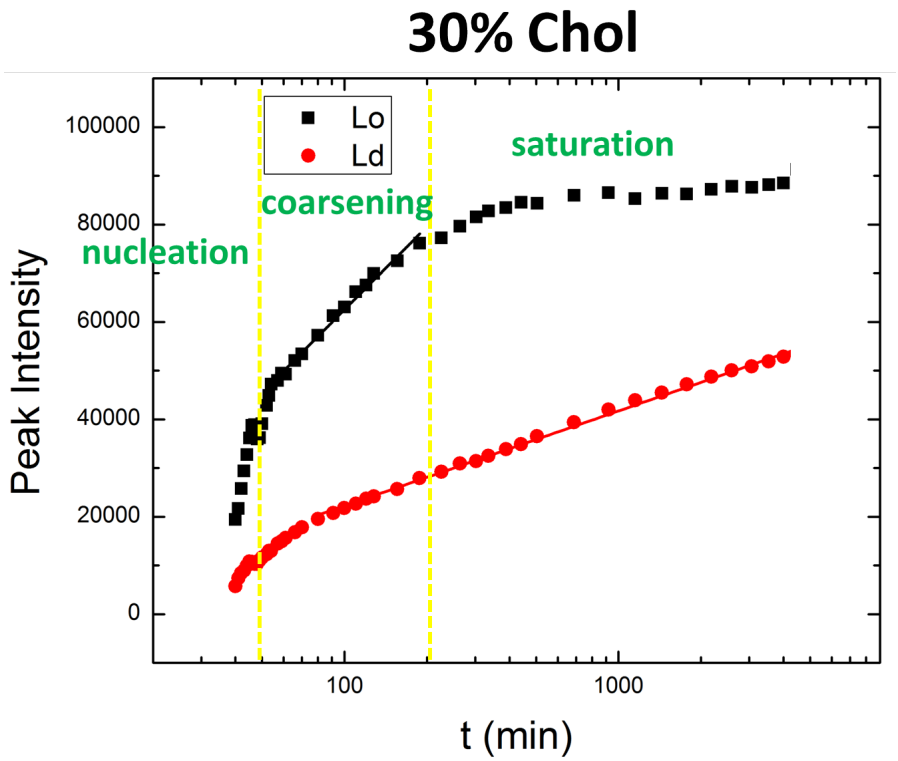

Figure 6.14: X-ray diffraction peak intensity of n = 1 order peak for 30% cholesterol sample. The vertical yellow dotted lines marks the transition time from nucleation stage to coarsening stage, and coarsening stage to saturation stage. Logarithmic fits for the coarsening phase are represented with the solid lines across data points.

6.5 Summary and Discussions

In this study, we mapped out the kinetics of domain growth of phase separated supported multilayer systems under 96% RH using both X-ray diffuse scattering and diffraction method. Different from the 2D domain growth in vesicles, the domains in multilayer systems have inter-layer coupling interaction, therefore undergo a 3D growth.

By decomposing the rocking curves into a sharp center component and a broad background component, we can simultaneously monitor the domain growth in volume, size and also the domain boundary change in volume and size with peak intensity and width. From the growth curve, we identified four stages for domain growth: breaking-order, nucleation, coarsening and saturation. A logarithmic growth is discovered in the coarsening stage, and is consistent across samples with different cholesterol concentration.

Results from samples with cholesterol concentration of 0%, 10%, 16%, 20%, 25% and 30% were reported. With increasing cholesterol concentration, the domain growth gets faster due to increased membrane fluidity. The transition between stages shifts to smaller time scales in our time window consistently when going from lower to higher cholesterol concentrations. During the transition from the gel phase with 0% cholesterol to the L_o phase with 10% cholesterol, we can see a difference in the domain boundary related peak during the nucleation stage. This may give some hint in the future studies of simulation to the structure of domain boundaries.

One thing worth point out is the strong dependence of domain growth kinetics on hydration. The observed logarithmic growth is heavily due to the partial hydration, while during full hydration it would change to a power law. Also the rate of growth can be sensitive to the particular hydration level as well, so we would expect different growth rates of logarithmic growth for different RH values lower than 98%. The small differences in RH between runs can potentially be a big source of error on accurately measuring the growth rate for that particular RH.

6.6 Acknowledgement

I would like to acknowledge my co-authors Sajal K. Ghosh, David A. DiLena and Sunil K. Sinha for the work in this chapter.

7 AFM, Optical and Fluorescence imaging studies on phase separated lipid multilayer surface morphology

7.1 Overview

Atomic Force Microscopy (AFM), optical and fluorescence microscopy are powerful ways to visualize the phase separated lipid domains on different length scales. By tuning temperature and sample thickness, we can control domain sizes for studies of different length scales. With AFM, submicron domain formation and melting close to phase transition temperature for thin samples were studied with fine control of temperature. A linear trend of domain size vs. domain height was discovered close to the phase transition temperature. Also, the melting of domains seems to follow a tiered size selection rule. The surface morphology change due to increased hydration introduced energy cost is also studied.

Optical and fluorescence microscopy observed domains in a much larger length scale of hundreds of microns with thick samples far away from phase transition temperature. The surface morphology can be easily observed with optical/bright field microscopy, which closely relates to the domain distribution observed by fluorescence microscopy. The edge adsorption effects observed with AFM at submicron length scale are also manifest in this much larger length scale. Some

beautiful rose-shaped phase morphology were recorded, which developed under the law of minimized free energy.

7.2 Materials and Methods

7.2.1 Sample preparation

There are three kinds of samples used for imaging studies. First are spin coated thin films for AFM studies. These thin samples are consist of only $10 \sim 20$ bilayers. Second is the film made by the spreading method for optical microscopy, same as the samples for X-ray studies. The third kind is the fluorescence dyed samples made by the spreading method used for fluorescence microscopy. The second and the third kind of samples were prepared with the same procedure which was already described in the previous chapters, only difference is the inclusion of the fluorescent dye as a fourth lipid component in the fluorescent samples. With the spreading method, the sample consists of several hundreds to thousand bilayers.

1:1 DOPC:DPPC with 16% cholesterol lipid composition was dissolved in 1:1 TFE: chloroform solvent, spread on 10 mm by 10 mm hydrophilic silicon substrate to spin coat into a thin film of $10 \sim 20$ bilayers. The procedure was developed based on Mennicke and Salditts method [109]. After spin coating, the film was left to dry for a few hours, then put into the vacuum for more than 24 hrs in order to evaporate any trace of organic solvent. Then, the film was re-hydrated in 98% RH humidity chamber under $50°C$ for less than 12 hrs, then cooled to room temperature and put under room RH. Note that the spin coated samples do not need as much time to anneal at high temperature under humidity as the thick samples do because they have many fewer bilayers and equilibrate quickly. If annealing for too long, the sample could de-wet from the substrate.

For fluorescent samples, DiI16, DiIC18 and β-BODIPY fluorescence dyes were used. DiI16 fluorescence dye, which preferably partitions into the L_d phase, was mainly used in the sample images presented in this chapter. DiIC18 and β-BODIPY fluorescence dyes were also used to confirm the identification of phases.

7.2.2 Experimental setup

We designed and custom made a small sample holder equipped with heater and temperature sensor for sample temperature control of AFM measurements. The humidity was maintained by sealing the AFM with a plastic bag, and placing a reservoir with saturated salt solution inside. The optical, bright field and fluorescence microscopy were taken with samples sealed inside humidity chambers with glass windows on the top, and saturated salt solution inside as reservoir.

7.3 Results

7.3.1 AFM studies of domain melting

A spin coated thin film of 1:1 DOPC: DPPC with 16% cholesterol was measured close to phase transition temperature with temperature control under $\sim$ 96% RH. The nominal phase transition temperature for the sample was around $47°C$. The sample was first cooled down to $45°C$, then slowly warmed up to $46°C$, $46.5°C$ and $47°C$. The phase transition temperature for this sample was $\sim$ 10 degrees higher than the real transition temperature of this composition, which might be due to the temperature gradient of the chamber plus the sensor offset. Therefore, they are denoted as the nominal temperatures. Figure 7.1 shows the AFM images of each temperature.

In the above figure, we can see relatively small closed domains, which are the L_o phase domains, and the rest is the L_d phase. The terraces are bilayer edges of the L_d phase. There is a lot of information we can obtain from these images. First of all, we can see that with the increase of temperature, the number density of the L_o phase domains decreases. Secondly, the domains size distribution also changes with temperature. Lastly, close to the terrace edges, the distribution of domains appears to be different from the domains far away from the terrace edges. In the following sections, we are going to discuss each point in detail. The edge effects will be described separately in section 3.2. In the following two subsections, we are going to focus on the domains away from the terrace edges to gain knowl-

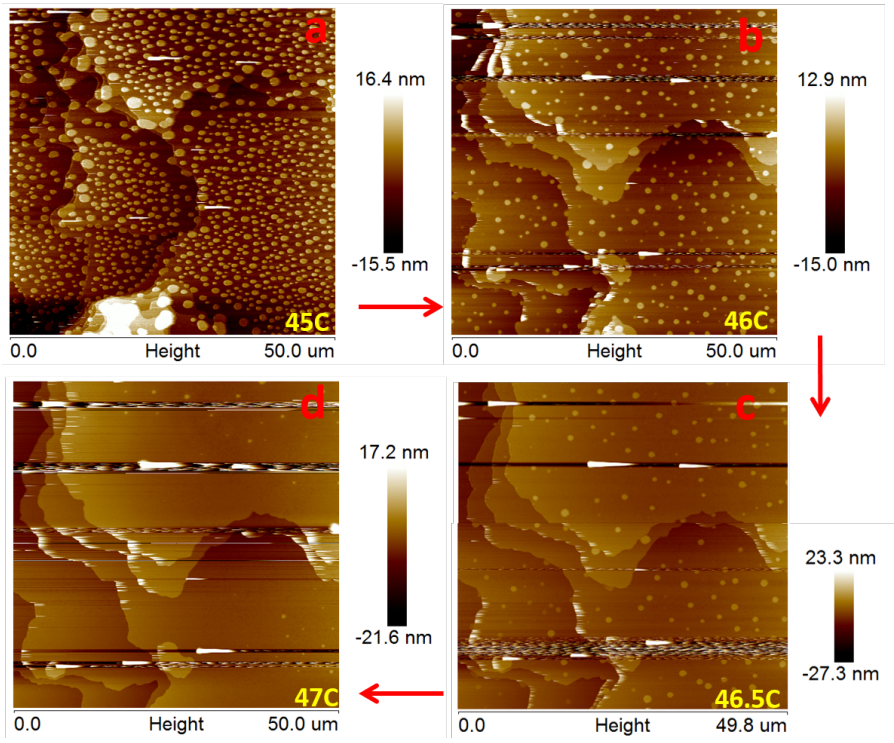

Figure 7.1: The AFM images of a spin coated 1:1 DOPC:DPPC with 16% cholesterol sample at $45°C$ (a), $46°C$ (b), $46.5°C$ (c) and $47°C$ (d). The arrows mark the direction of temperature increase. The round dotted figures in the images are L_o domains, where the terraces like figures are bilayers of L_d phase.

edge about domain melting in the bulk.

Statistical analysis

With particle analysis in the AFM image analysis program, we can get a statistical view of the distribution of L_o phase domain sizes, densities and heights for each temperature. Figure 7.2 shows the area we selected for the analysis, and the domains were highlighted with blue.

The domain sizes, heights, and number densities can be obtained from the particle analysis. The results are shown in Figure 7.3. Note that the domain heights are measured relative to the L_d phase surface, therefore not directly the domain size in the vertical direction (counting domain volume imbedded under the surface). The number of bilayers in the domain can be calculated with $N = h/0.7$, where 0.7 nm is the bilayer thickness difference between the L_o and L_d phases.

From the plots, we can see that with decreasing temperature, the domain number density, area fraction both decrease dramatically (more than 70% drop from first temperature), while domain height also decrease (about 50%), and average domain diameter remains the same (slight increase within 10%).

So on average, the domains remains the same sizes (diameter) while mainly reduce in number density and domain height to reduce the phase volume when raising temperature. Among which, the reduction in number density contributes more than 80% of the total phase volume reduction. In order to farther understand this melting behavior, we carried out the individual domain tracking between different temperatures to see what happened to each domain during melting.

Individual domain tracking

We indexed 76 domains at $46°C$ to observe the changes as the temperature was raised to $46.5°C$. Among the 76 indexed domains, 41 completely melted and 35 remained. The domain diameter vs. domain height are plotted in Figure 7.4.

The dark blue and light blue dots mark the domains at $46°C$, while the red

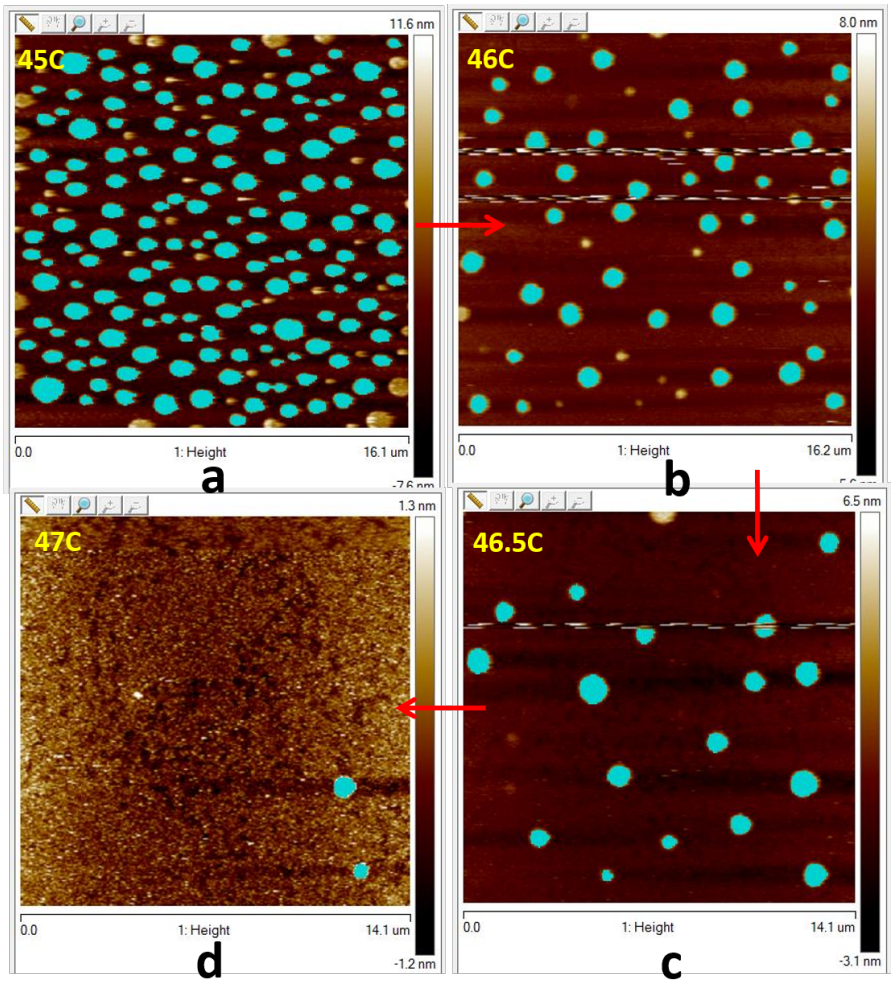

Figure 7.2: Selected AFM areas for particle analysis at $45°C$ (a), $46°C$ (b), $46.5°C$ (c) and $47°C$ (d). The L_o phase domains are highlighted with blue. The background is the L_d phase. The height measured from the domains are the relative heights from the L_d phase surface.

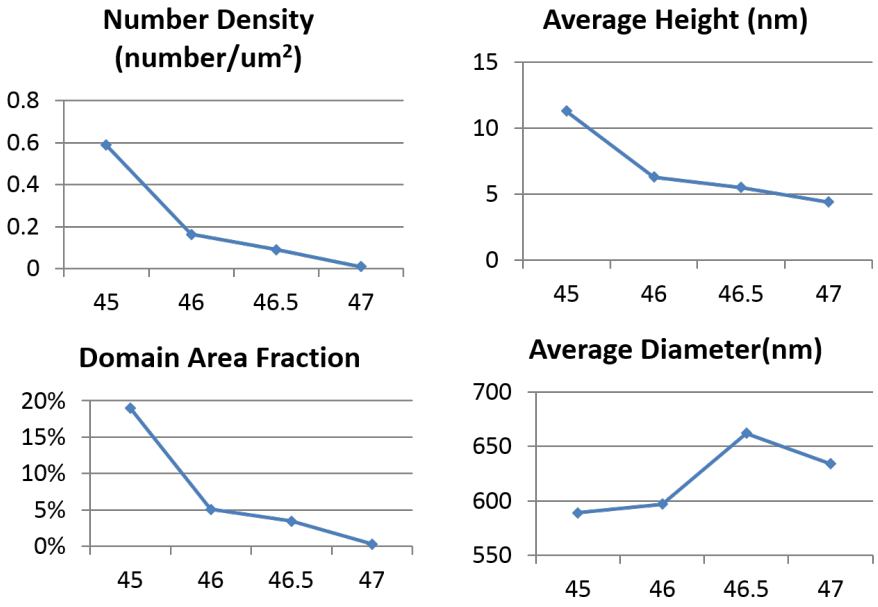

Figure 7.3: Plots of domain number density, average height, area fraction and average diameter vs. temperature (x-axis).

ones mark domains at $46.5°C$. Among the $46°C$ domains, the light blue ones are the domains completely melted after raising temperature to $46.5°C$, and the dark blue ones are the survived domains which turned into the red ones after raising temperature.

The melted domains (light blue) and the survivors (dark blue) are spatially well separated. It looks like there is a critical domain size of $\sim 0.68\ \mu m$ below which that all domains would melt completely. The survivors (dark blue) become the red dots which forms a new distribution which follows a linear relationship between the domain size and domain height. The red line shows the fit. In the following 3 figures, we are going to pair up the individual domains of the 2 temperatures to show the changes.

The mappings are grouped by the nominal changes in domain volumes. The nominal change in domain volume are calculated as $\Delta V = A'h' - Ah$, where A', h' are the domain area and height of the $46.5°C$, A, h are the domain area and height at $46°C$. The real change in domain volume can be calculated by $\Delta V/0.7$ in the unit of number of bilayers. Figure 7.5 shows the domains which volume changes

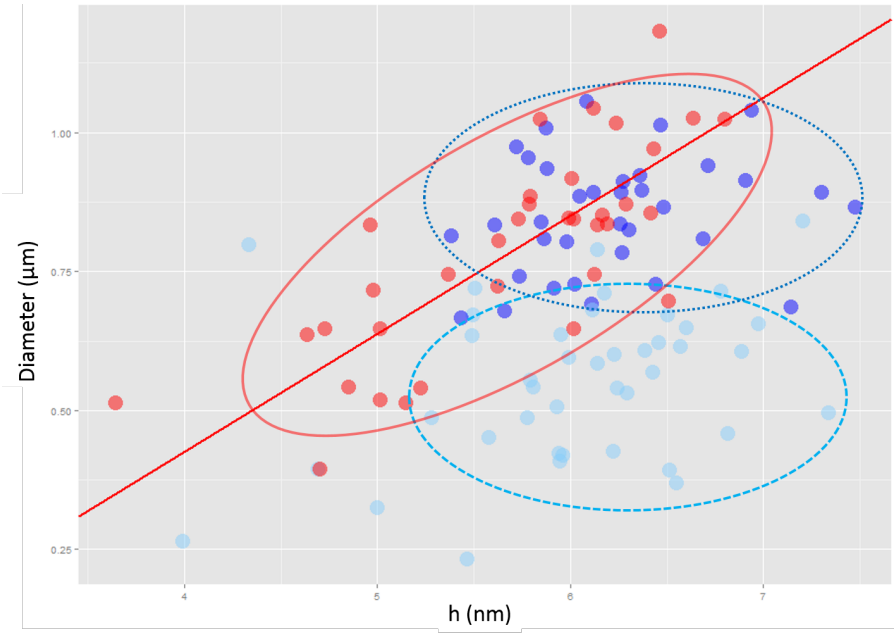

Figure 7.4: Domain diameter vs. domain height for $46°C$ (dark blue and light blue dots) and $46.5°C$ (red dots). Among domains at $46°C$, the light blue dots are the domains which completely melted when temperature is raised to $46.5°C$, and the dark blue ones are the survivors which become the red dots at $46.5°C$. The three colored dots can be grouped with circles with the respective colors. The red dots (domains at $46.5°C$) is fitted with a linear function, which is the red straight line.

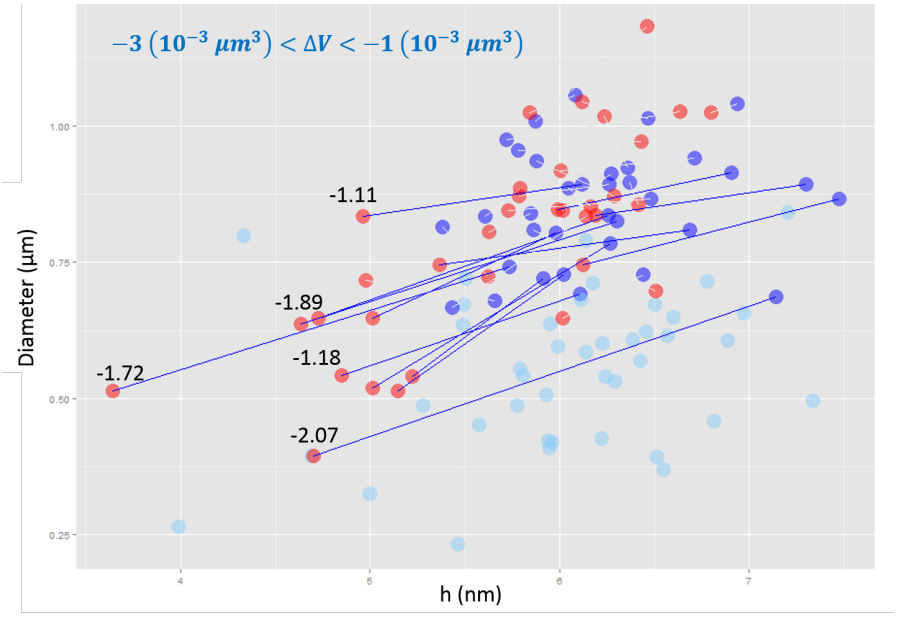

Figure 7.5: 7.5. Paired mapping of survival domains from dark blue at $46°C$ to the red at $46.5°C$ of domain volume change ΔV less than $-1 \times 10^{-3}\mu m^3$.

ΔV less than $-1 \times 10^{-3}\mu m^3$, Figure 7.6 shows domains which ΔV are between -1 and $0 \times -1 \times 10^{-3}\mu m^3$, while Figure 7.7 shows domains which $\Delta V > 0$.

In Figure 7.5, this group of domains travel far both in h and diameter on the diagram. The size of domains are relatively small among the whole "survival population". The domains lose whole bilayers from the bottom (from change of h), and also their diameters shrunk, to form the left most groups of the red dots at higher temperature. Because these domains lose both height and width, this group of domains have lost the most volume amongst the survivors.

This group of domains distributed more narrowly around 6nm of height, and the sizes distribution moved up a little comparing to the previous group. The change in ΔV is quite small, which means the domains does not melt much either in the height or width. The corresponding red dots are the ones in the middle range both in height and width in the red population.

This group of domains actually grow larger than before after melting, which is counter intuitive, although the number is very few. The height of the domain also concentrated around 6 nm, while the size of the domain is at the top of the

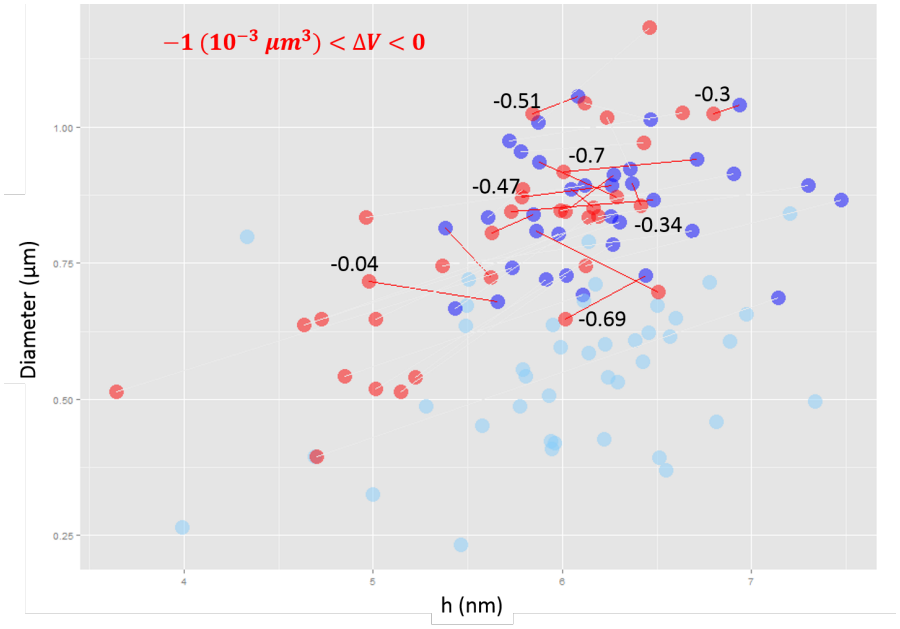

Figure 7.6: Paired mapping of survival domains from dark blue at $46°C$ to the red at $46.5°C$ of domain volume change ΔV more than $-1 \times 10^{-3}\mu m^3$ and less than 0.

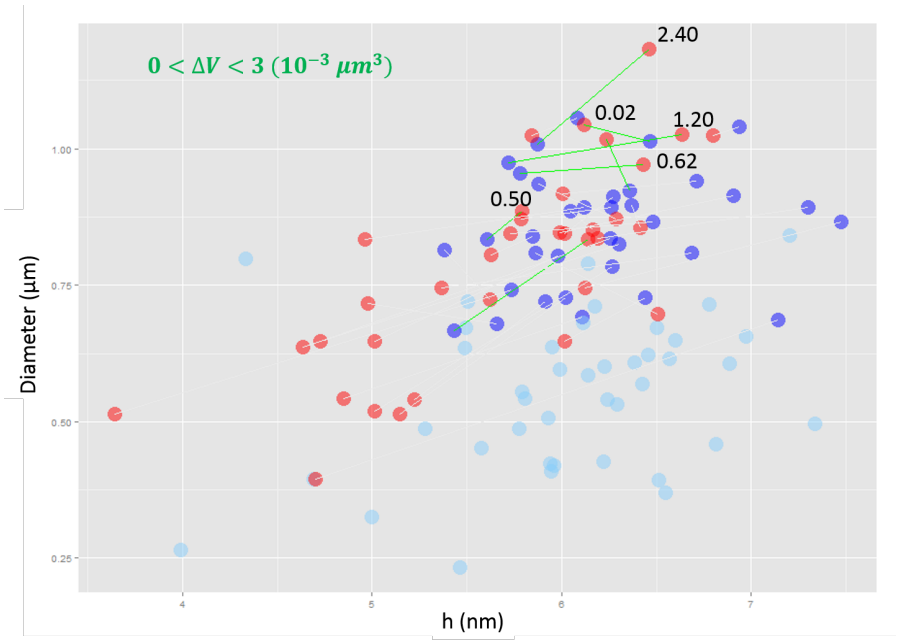

Figure 7.7: Paired mapping of survival domains from dark blue at $46°C$ to the red at $46.5°C$ of domain volume change ΔV larger than 0.

survivor population. The corresponding red dots are also the top population in size of the red population.

To summarize the above funding, we draw a schematic summary of the domain melting and its size/height dependence (Figure 7.8). First row of domains are the initial domain distribution at $46°C$, while the second row of domains are the corresponding domain at $46.5°C$. The domains of diameter less than 0.68 m are all melted, whereas the larger ones form a wider distribution of domains according to their sizes as well. The loss of domain volumes are not the same for the survivors: the larger the domain diameter, the less the loss is. So here are our two assumptions concluded from the summary:

Firstly, there is a critical domain size, below which all domains would melt;

Secondly, the survival domains all have a shape that abbeys certain linear relationship of diameter vs. h. In other words, the survival population has developed into shapes that are around a fixed aspect ratio, with some constant shift. In order to fulfill this requirement, the initial population has to lose different amount of volume depending on its initial size.

The most dramatic volume cut is through losing entire bilayers, where domain melt vertically from the bottom. As the domain reduce its height, it has to reduce its lateral size as well to meet the constant aspect ratio requirement. The reduction in lateral sizes are continuous, while the reduction in height is quantized, as it is counted by the number of whole bilayers that melt completely. To melt a whole bilayer of a smaller domain is relatively easy, while for a larger domain it might be too much volume to reduce. This can explain why mainly the smaller sized domains are losing its heights, while the larger ones does not change much.

We can also see this size-dependent melting in an area correlation plot. See Figure 7.9. The plot shows the domain areas of $46.5°C$ (A2) vs. the domain areas of $46°C$ (A1) for the same domain. The critical size is marked by the vertical blue dotted line, below which the domains all melted completely. The correlation of the survival domain sizes can be fitted with a straight line of slope 1.6. The slope of 1 with no intercept is marked by the green dotted line. Along this line, the domain area stays the same. So before the intercept of the green line and the red, the

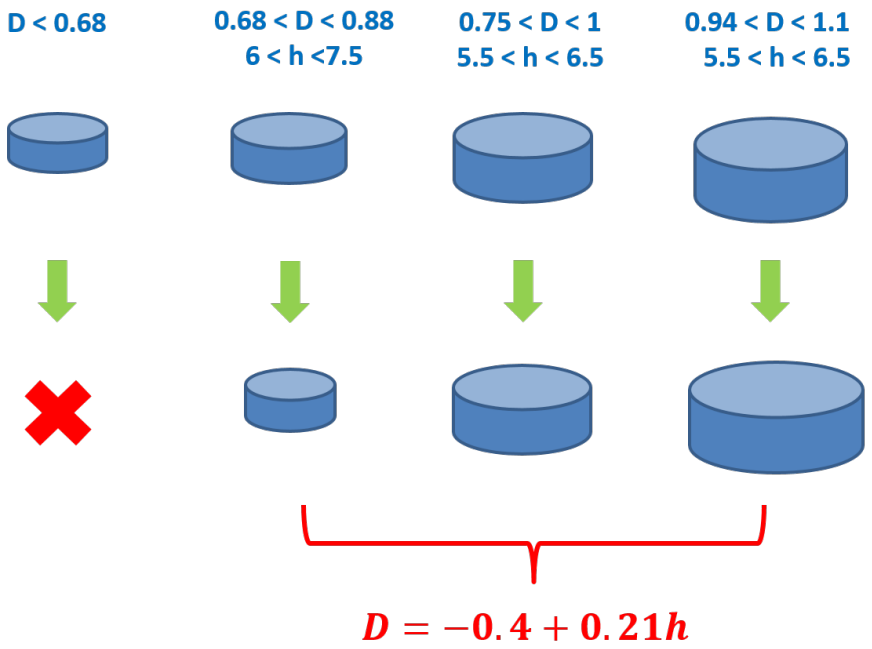

Figure 7.8: Schematics of the summary of domain size re-distribution during melting.

domains are becoming smaller, while after it the domains are getting larger in the area after raising the temperature from $46°C$ to $46.5°C$.

It is worth pointing out that the melting describing here is not melting like the melting of ice. The phase transition in the ternary lipid mixture system is a miscibility-immiscibility transition, which means that miscibility depends on the temperature. At each different temperature, the composition for each phase is different. So in the melting process, the domains are not only reducing their sizes, but also changing their all over composition. For example, at a higher temperature, the L_o domains become less rich in DPPC. The size re-distribution after melting is based on the initial distribution, but also has to obey the volume fraction and composition according to the phase diagram.

dge adsorption and hysteresis

Domains close to the terrace edges behave very differently from the domains in the bulk. From Figure 7.10, the multilayer terraces are easily seen. The domains

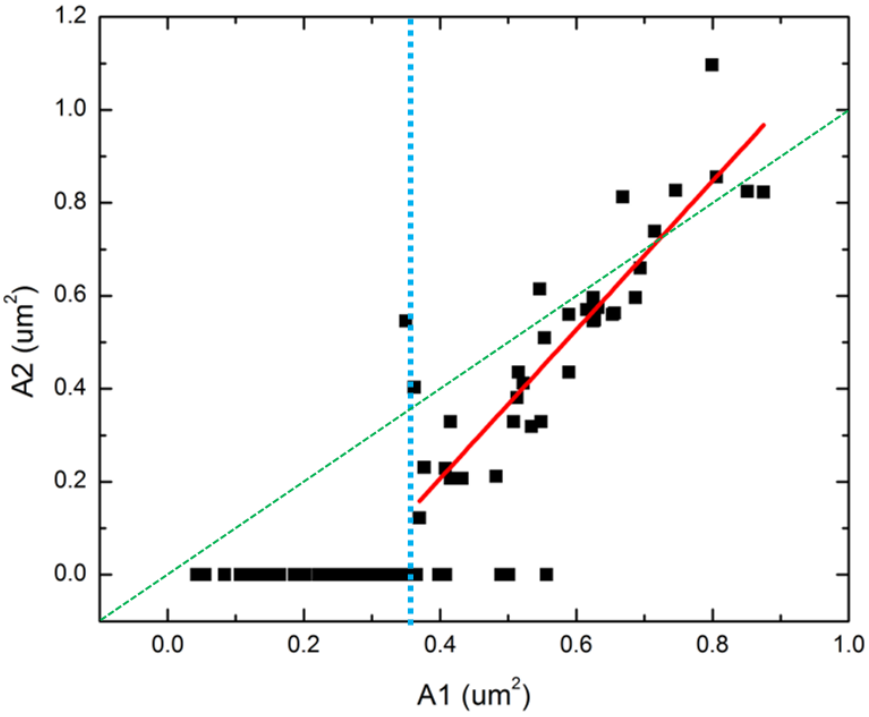

Figure 7.9: Domain area of 46.5°C vs. domain area of 46°C plot. The survival domains can be fitted with a straight line with slope 1.6, as shown by the red line. The green dashed line marks the slope of 1, along which the areas do not change. The critical area for complete melting is marked with the vertical blue dashed line. Below this area, the domains are completely melted.

adsorbed to the terrace edges are much larger on average than the domains away from the edges. Inside selected area a away from the terrace edge, the average domain diameter is 640 nm, while area b along the terrace edge, the average domain diameter is 1764 nm. As a result of larger domains forming along the terrace edge, a depletion region of L_d phase formed along the terrace edge, as marked by the yellow arrows. The width of the depletion region is around 3.8 m, as shown in the section measurement (b). The width of the depletion region is decided by the sizes of the domains adsorbed to the edge, which in turn strongly correlated with the local thickness of the film. This agrees with our previous founding of domain sizes related to multilayer thickness [25].

During temperature cycling, the L_o domains adsorbed to the terrace edges form first during cooling, and disappear first during heating (Figure 7.1). This demonstrates that along the terrace edges there is less hysteresis than in the bulk.

A closer look at the terrace edges are shown in the Figure 7.11. In this magnified scale, the domains merging along the edge (a) and layers of domains appearing during formation (c) can be seen. The phase images (b, d) shows large phase contrast between the different materials of L_o and L_d phase.

Apart from the AFM measurements, the domain adsorption along the terrace edges is also commonly seen in the fluorescence microscopy measurements. Figure 7.12 shows the combined bright field image and fluorescence image of a thick phase separated multilayer. The fluorescent dye Dil16 preferably partitions into the L_d phase, so the dark region along the terrace edge (as shown by contrast in bright field image a) are adsorbed L_o domains. Due to the surface in-homogeneity in thick multilayers, the domains would form interesting surface morphologies, such as rose shape features shown in Figure 7.13. The sharp edges pointed by the arrows are the results of balancing L_o-L_d domain boundary energy cost and domain-air interfacial energy cost.

Substrate effect on domain melting

Above the miscibility phase transition temperature ($50°C$), we discovered

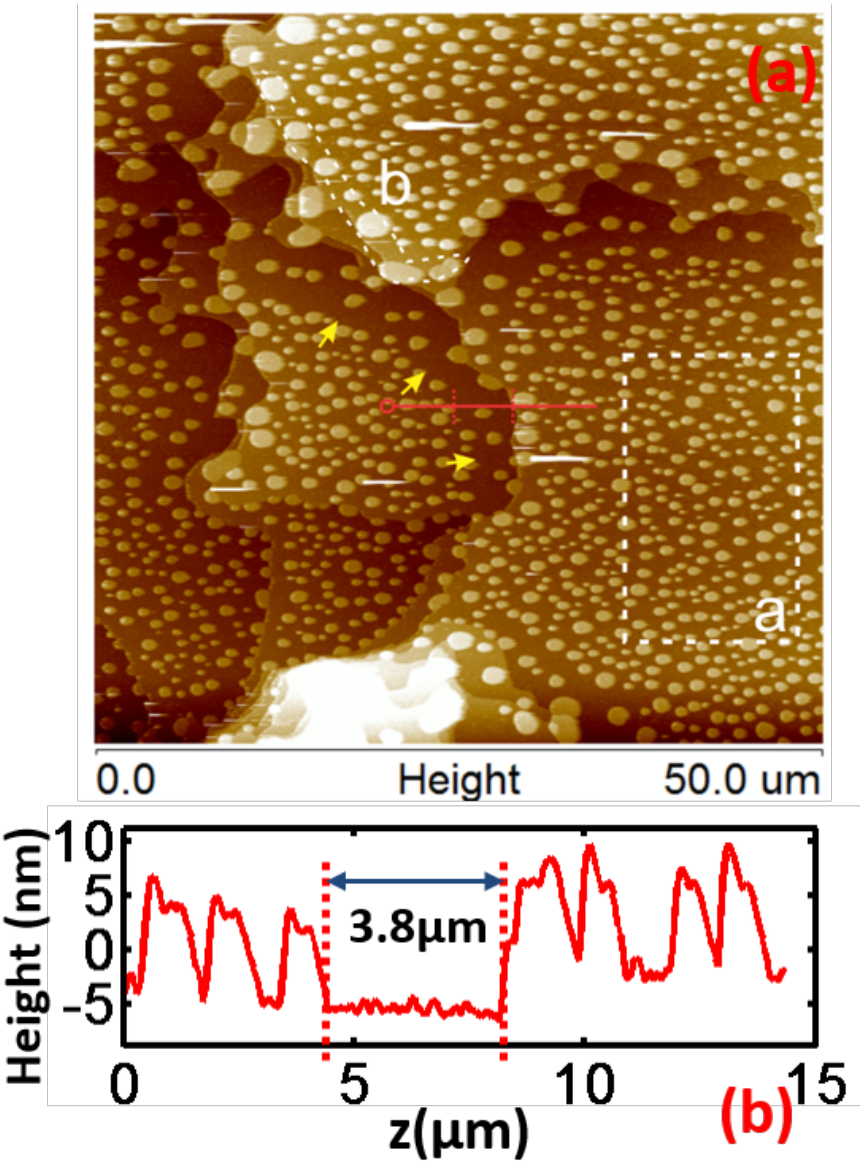

Figure 7.10: AFM image of $45°C$ (a) and a section measurement (line cut) along the horizontal red line (b). The area a is a typical area of bulk, where the average domain size is 640 nm in diameter, while the area b long the terrace edge the average domain size is 1764 nm in diameter. As a result of larger domains forming along the terrace edge, a depletion region of L_d phase formed along the terrace edge is marked by the yellow arrows. The width of the region is around 3.8 m.

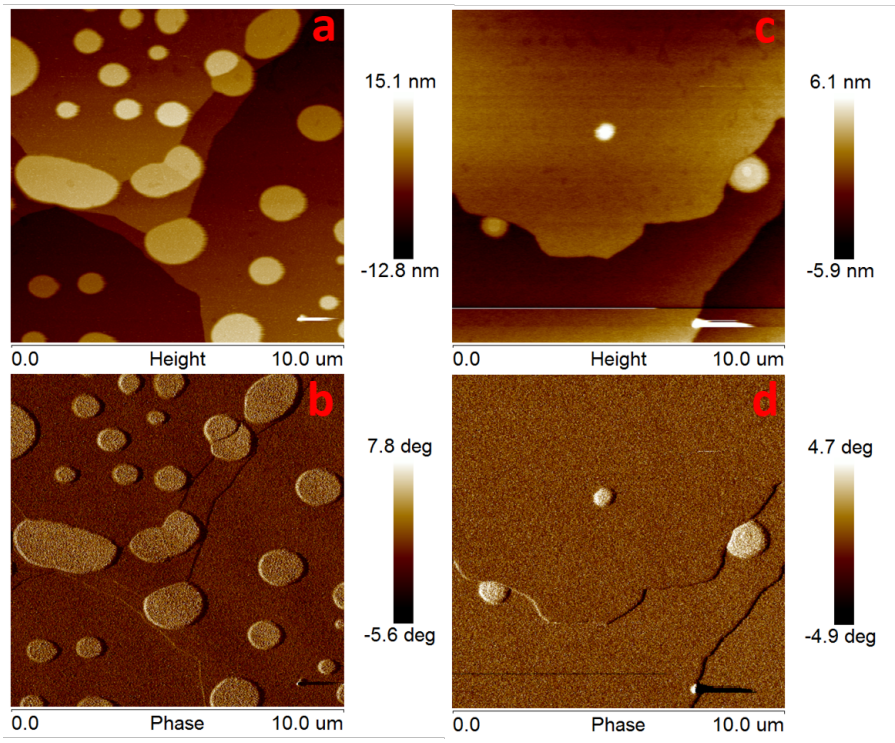

Figure 7.11: Detailed AFM images of the terrace edges. (a, c) are the height measurements, while (b, d) are phase measurement of (a, c) respectively. The phase contrast demonstrates that the L_o and L_d phase different materials are recognized by the phase measurement.

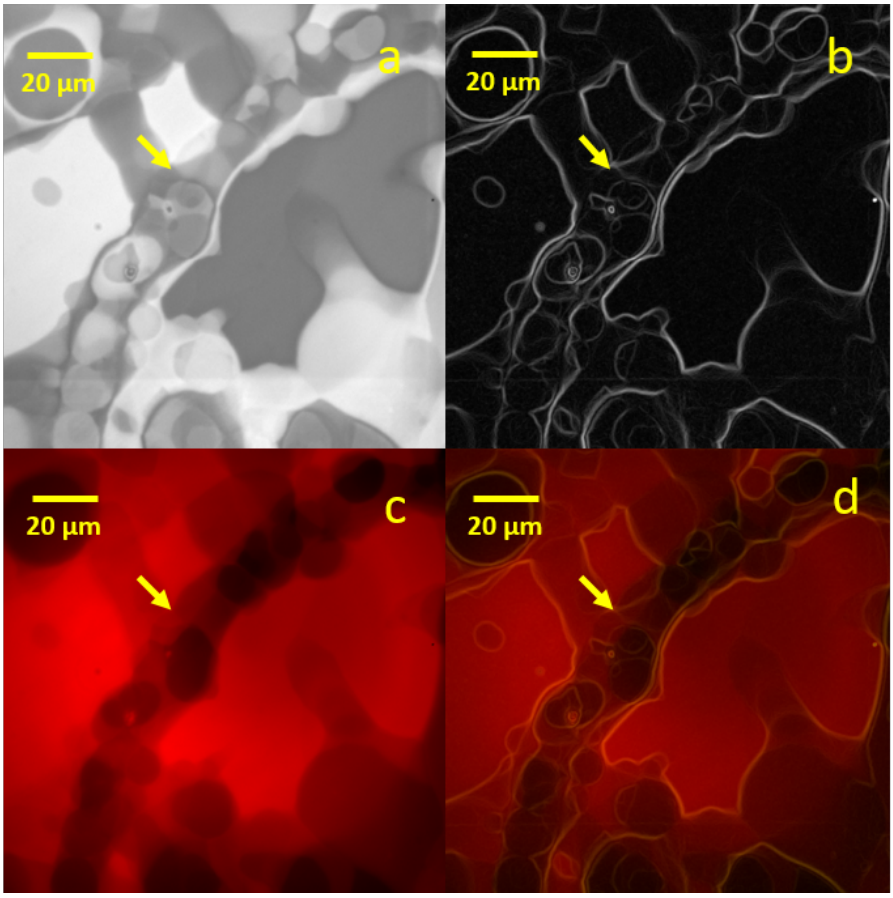

Figure 7.12: Bright field image (a) and fluorescence microscopy image (c) of L_o phase domains align along the terrace edge. (b) is the edge calculation of (a), which highlights the sharp height changes on the surface. (d) is the overlay of (b) and (c), which demonstrates the height change correlates with the phase formation. The width of the adsorbed domain region is around 20 m.

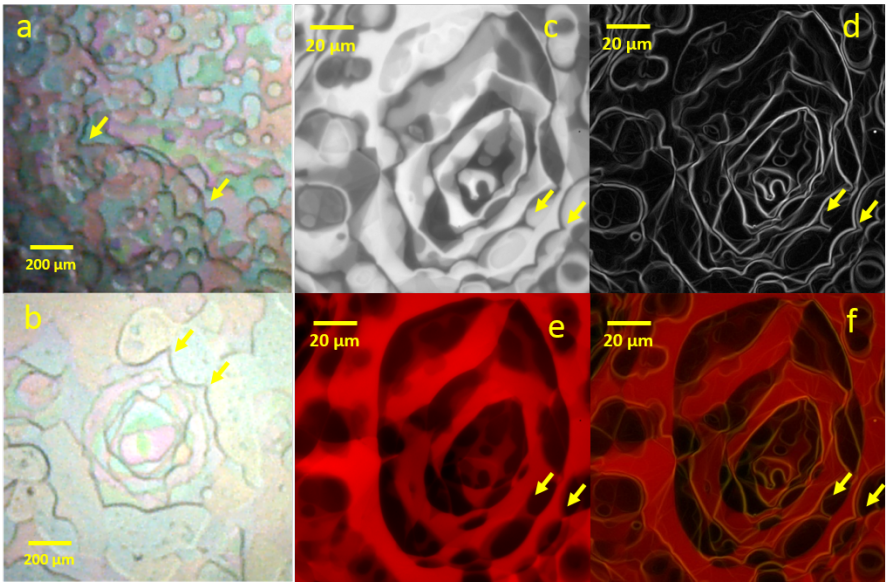

Figure 7.13: Rose-like structure observe under optical microcopy (a, b), bright field image (c), edge calculation of bright field image (d), fluorescence image (e), and overlay of (d, e), (f).

another interesting feature with AFM. See Figure 7.14. The sample surface we were looking at was in the homogenous phase. However, besides the multilayer steps pointed by the blue arrows, we also observed some small regions on each layer, such as the one pointed to by the red arrow (a). These small regions do not show contrast in the AFM phase measurement (b), which means that the top surface are all the same material, and the small regions are only the height differences. By doing line cut (c), we can see the heights of the small regions are around 7, while the multilayer steps are around 5 nm.

In the homogenous phase, there should not be any coexisting phases. However, this measurement of 7 Å corresponds so well with the bilayer thickness difference between the L_o and L_d phase. We postulate that there might be a substrate effect on the domain melting, while the one bilayer directly against the substrate stayed phase separated unlike all the other bilayers, which results in a height difference which propagated to the sample surface.

Hydration effect on surface morphology

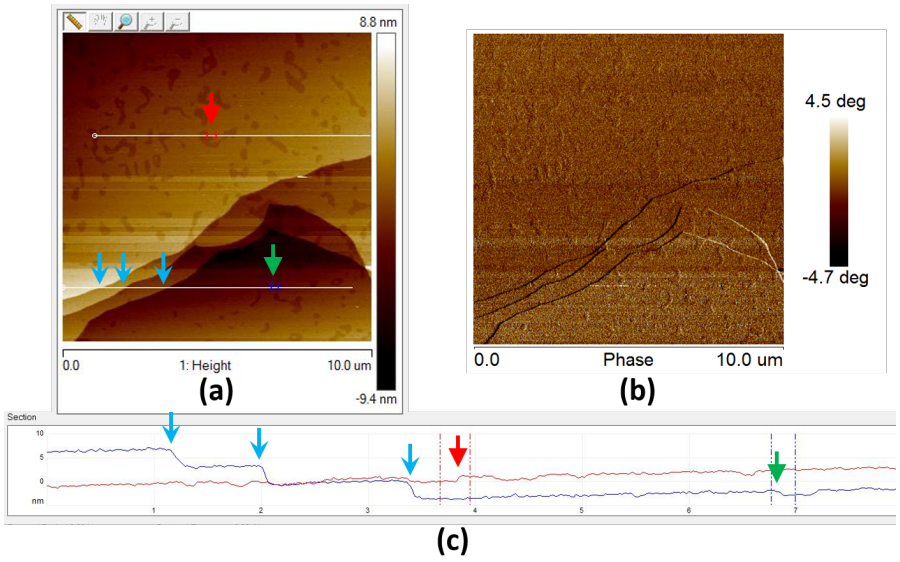

Figure 7.14: AFM image of sample above phase transition ($50°C$). (a) is the height measurement, (b) is the phase measurement, and (c) is the section measurement of (a), which are line cuts along the two horizontal lines. The bilayer edges are marked by blue arrows with a height difference of $\sim$ 5nm, while the small figures are marked by the red and green arrows with a height difference of $\sim$ 7 Å.

One other interesting experiment we did was to put a phase separated dry film into the humidity cell, and observe the sample surface morphology change during the process of hydration. The sample was kept at constant temperature of $46°C$. Figure 7.15 shows the series AFM images taken during the process. (a) shows the sample morphology when the sample was in the dry condition. We can see an elongated finger shape extends from the multilayer terrace. Because of the low environmental humidity, this morphology can exist because the open ends of bilayers at multilayer edges do not cost much energy. After we sealed the whole experimental setup with humidity inside, the system under went change as shown by images from (b) to (g). To guide the eye, the same region we are focusing on is cycled by yellow in each image, while a yellow arrow points to the tip of the 'finger'.

We can see that after humidity increased in the environment, the finger slowly retracts to decrease the length of the side. However, the two domains in (a)

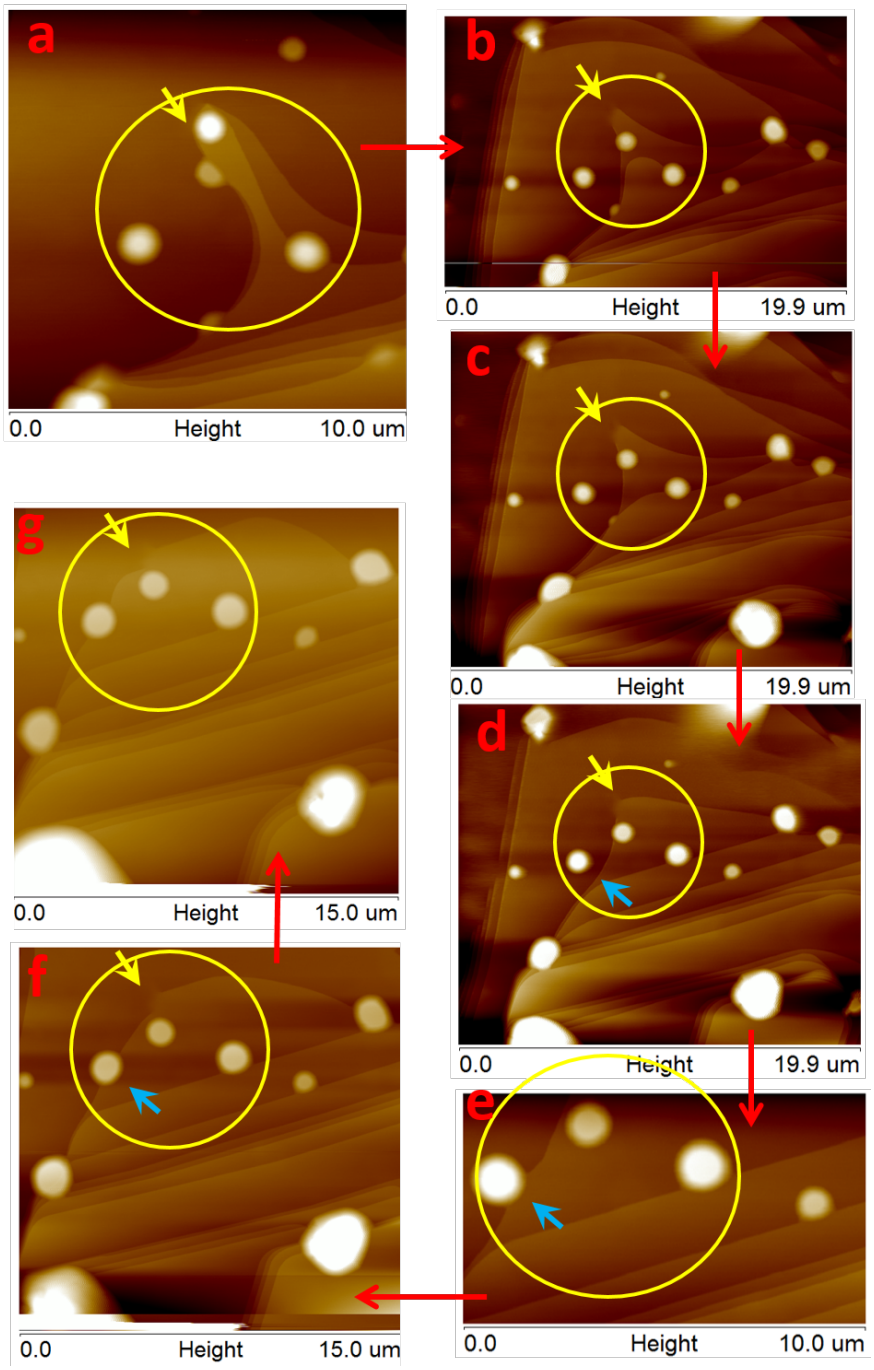

Figure 7.15: AFM image series of the hydration process of a phase separated thin multilayer morphology change. Yellow circles mark the same region of interest, and the yellow arrows pointed at the tip of the 'finger feature. The sequence is from (a) to (g), also guided by the red arrows.

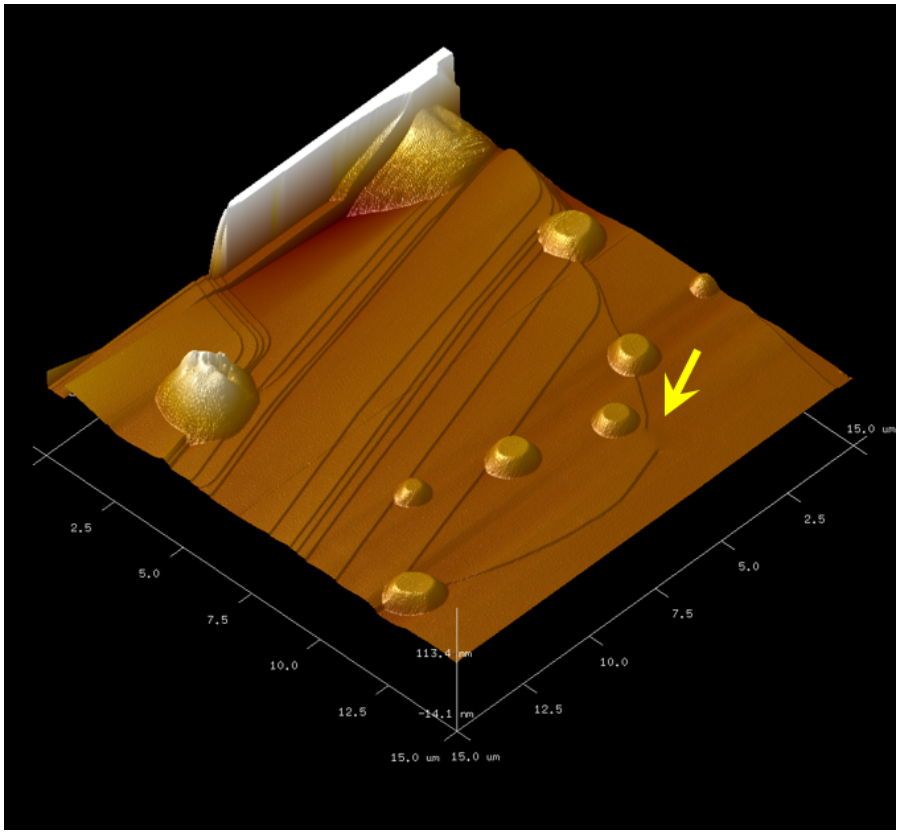

Figure 7.16: 3-Dimentional plot of Figure 7.15 (f). The yellow arrow points to the stitch-like defect resulted from the merging of two L_o domains.

pointed by the yellow arrow merged with each other during the finger retraction and created a stitch-like defect which stitches the top bilayer down to the one underneath, as pointed by the yellow arrow in (b). The defect pined the bilayer from retracting much further. As a result, the whole bilayer is dragged over to further reducing its overall length of the side (c $\sim$ g). A 3D image is created to better visualize the stitching defect (Figure 7.16).

The main reason for the terraces to re-structure to reduce the length of their sides is because of the interfacial energy of the open-ends against the humid air. The bilayer open ends expose the hydrophobic tail group of the lipid to water vapor in air. When the air humidity is low ($<$ 30% RH in room humidity), the interfacial energy is small; nonetheless, when RH increases to $\sim$ 96%, the energy cost becomes large and system needs to re-adjust.

Furthermore, after a L_o domain gets adsorbed to the terrace edge (indicated by blue arrows in (d, e, f)), the bilayer terrace would be pinned by the domain. The rule of reducing length of sides is simple: if a line is pinned on both sides, it will form a straight line; if the area has to be maintained with no pinning, it will form a round shape. The final morphology has to obey the minimum length of side rule, as it reaches its equilibrium of minimum energy. In the final images Figure 7.15 (f, g), and 3D image in Figure 7.16, we can appreciate the perfect straight parallel terrace edges as a beautiful proof of the minimum energy rule.

7.4 Acknowledgement

I would like to acknowledge my co-authors Laura Connelly, Nirav Patel, Fernando Teran Arce, Ratnesh Lal and Sunil K. Sinha for the work in this chapter.

Bibliography

[1] Kalina Hristova and Stephen H White. Determination of the hydrocarbon core structure of fluid dioleoylphosphocholine (dopc) bilayers by x-ray diffraction using specific bromination of the double-bonds: effect of hydration. *Biophysical journal*, 74(5):2419–2433, 1998.

[2] Stephanie Tristram-Nagle, Horia I Petrache, and John F Nagle. Structure and interactions of fully hydrated dioleoylphosphatidylcholine bilayers. *Biophysical journal*, 75(2):917–925, 1998.

[3] MC Wiener, RM Suter, and JF Nagle. Structure of the fully hydrated gel phase of dipalmitoylphosphatidylcholine. *Biophysical journal*, 55(2):315–325, 1989.

[4] Horia I Petrache, Nikolai Gouliaev, Stephanie Tristram-Nagle, Ruitian Zhang, Robert M Suter, and John F Nagle. Interbilayer interactions from high-resolution x-ray scattering. *Physical Review E*, 57(6):7014–7024, 1998.

[5] Giulio Caracciolo, Marco Petruccetti, and Ruggero Caminiti. A new experimental setup for the study of lipid hydration by energy dispersive x-ray diffraction. *Chemical physics letters*, 414(4):456–460, 2005.

[6] Horia I Petrache, Stephanie Tristram-Nagle, Klaus Gawrisch, Daniel Harries, V Adrian Parsegian, and John F Nagle. Structure and fluctuations of charged phosphatidylserine bilayers in the absence of salt. *Biophysical journal*, 86(3):1574–1586, 2004.

[7] Kai Simons and Elina Ikonen. Functional rafts in cell membranes. *Nature*, 387(6633):569–572, 1997.

[8] Sarah L Keller, Arun Radhakrishnan, and Harden M McConnell. Saturated phospholipids with high melting temperatures form complexes with cholesterol in monolayers. *The Journal of Physical Chemistry B*, 104(31):7522–7527, 2000.

[9] Sarah L Veatch and Sarah L Keller. Organization in lipid membranes containing cholesterol. *Physical review letters*, 89(26):268101, 2002.

[10] Sarah L Veatch and Sarah L Keller. Separation of liquid phases in giant vesicles of ternary mixtures of phospholipids and cholesterol. *Biophysical journal*, 85(5):3074–3083, 2003.

[11] Sarah L Veatch and Sarah L Keller. Miscibility phase diagrams of giant vesicles containing sphingomyelin. *Physical review letters*, 94(14):148101, 2005.

[12] SL Veatch, IV Polozov, K Gawrisch, and SL Keller. Liquid domains in vesicles investigated by nmr and fluorescence microscopy. *Biophysical journal*, 86(5):2910–2922, 2004.

[13] Sarah L Veatch, Klaus Gawrisch, and Sarah L Keller. Closed-loop miscibility gap and quantitative tie-lines in ternary membranes containing diphytanoyl pc. *Biophysical journal*, 90(12):4428–4436, 2006.

[14] Sarah L Veatch, Olivier Soubias, Sarah L Keller, and Klaus Gawrisch. Critical fluctuations in domain-forming lipid mixtures. *Proceedings of the National Academy of Sciences*, 104(45):17650–17655, 2007.

[15] Stephen H White and Glen I King. Molecular packing and area compressibility of lipid bilayers. *Proceedings of the National Academy of Sciences*, 82(19):6532–6536, 1985.

[16] Glen I King and Stephen H White. Determining bilayer hydrocarbon thickness from neutron diffraction measurements using strip-function models. *Biophysical journal*, 49(5):1047, 1986.

[17] Michael C Wiener and Stephen H White. Structure of a fluid dioleoylphosphatidylcholine bilayer determined by joint refinement of x-ray and neutron diffraction data. ii. distribution and packing of terminal methyl groups. *Biophysical journal*, 61(2):428, 1992.

[18] Chenghao Li, Doru Constantin, and Tim Salditt. Biomimetic membranes of lipid–peptide model systems prepared on solid support. *Journal of Physics: Condensed Matter*, 16(26):S2439, 2004.

[19] Z Khattari, G Brotons, E Arbely, IT Arkin, TH Metzger, and T Salditt. Sars e protein in phospholipid bilayers: an anomalous x-ray reflectivity study. *Physica B: Condensed Matter*, 357(1):34–38, 2005.

[20] C Li and T Salditt. Structure of magainin and alamethicin in model membranes studied by x-ray reflectivity. *Biophysical journal*, 91(9):3285–3300, 2006.

[21] Yili Wu, Ke He, Steve J Ludtke, and Huey W Huang. X-ray diffraction study of lipid bilayer membranes interacting with amphiphilic helical peptides: diphytanoyl phosphatidylcholine with alamethicin at low concentrations. *Biophysical journal*, 68(6):2361, 1995.

[22] Thomas M Weiss, Patrick CA van der Wel, J Antoinette Killian, Roger E Koeppe, and Huey W Huang. Hydrophobic mismatch between helices and lipid bilayers. *Biophysical journal*, 84(1):379–385, 2003.

[23] Jianjun Pan, D Peter Tieleman, John F Nagle, Norbert Kučerka, and Stephanie Tristram-Nagle. Alamethicin in lipid bilayers: combined use of x-ray scattering and md simulations. *Biochimica et Biophysica Acta (BBA)-Biomembranes*, 1788(6):1387–1397, 2009.

[24] Stephanie Tristram-Nagle, Rob Chan, Edgar Kooijman, Pradeep Uppamoochikkal, Wei Qiang, David P Weliky, and John F Nagle. Hiv fusion peptide penetrates, disorders, and softens t-cell membrane mimics. *Journal of molecular biology*, 402(1):139–153, 2010.

[25] Lobat Tayebi, Yicong Ma, Daryoosh Vashaee, Gang Chen, Sunil K Sinha, and Atul N Parikh. Long-range interlayer alignment of intralayer domains in stacked lipid bilayers. *Nature materials*, 11(12):1074–1080, 2012.

[26] Jens Als-Nielsen and Des McMorrow. *Elements of modern X-ray physics*. John Wiley & Sons, 2011.

[27] Metin Tolan. *X-ray scattering from soft-matter thin films*. Springer, 1999.

[28] Sebastian Aeffner. *Stalk structures in lipid bilayer fusion studied by x-ray diffraction*, volume 6. Universitätsverlag Göttingen, 2012.

[29] Lai Ding, Wenhan Liu, Wangchen Wang, Charles J Glinka, David L Worcester, Lin Yang, and Huey W Huang. Diffraction techniques for nonlamellar phases of phospholipids. *Langmuir*, 20(21):9262–9269, 2004.

[30] Lin Yang and Huey W Huang. A rhombohedral phase of lipid containing a membrane fusion intermediate structure. *Biophysical journal*, 84(3):1808–1817, 2003.

[31] Bernard Dennis Cullity and Stuart R Stock. *Elements of X-ray Diffraction*. Pearson, 2001.

[32] MJ Buerger. The correction of x-ray diffraction intensities for lorentz and polarization factors. *Proceedings of the National Academy of Sciences of the United States of America*, 26(11):637, 1940.

[33] Glen I King, Russell E Jacobs, and Stephen H White. Hexane dissolved in dioleoyllecithin bilayers has a partial molar volume of approximately zero. *Biochemistry*, 24(17):4637–4645, 1985.

[34] Russell E Jacobs and Stephen H White. The nature of the hydrophobic binding of small peptides at the bilayer interface: implications for the insertion of transbilayer helices. *Biochemistry*, 28(8):3421–3437, 1989.

[35] Allen E Blaurock. Structure of the nerve myelin membrane: proof of the low-resolution profile. *Journal of molecular biology*, 56(1):35–52, 1971.

[36] CR Worthington. Sampling-theorem expressions in membrane diffraction. *Journal of Applied Crystallography*, 21(4):322–325, 1988.

[37] CR Worthington. The determination of the first-order phase in membrane diffraction using electron density strip models. *Journal of Applied Crystallography*, 14(6):387–391, 1981.

[38] Claude Elwood Shannon. Communication in the presence of noise. *Proceedings of the IRE*, 37(1):10–21, 1949.

[39] David Sayre. Some implications of a theorem due to shannon. *Acta Crystallographica*, 5(6):843–843, 1952.

[40] M Seul and MJ Sammon. Preparation of surfactant multilayer films on solid substrates by deposition from organic solution. *Thin Solid Films*, 185(2):287–305, 1990.

[41] Deborah A Brown and John K Rose. Sorting of gpi-anchored proteins to glycolipid-enriched membrane subdomains during transport to the apical cell surface. *Cell*, 68(3):533–544, 1992.

[42] Kai Simons and Elina Ikonen. How cells handle cholesterol. *Science*, 290(5497):1721–1726, 2000.

[43] Daniel Lingwood, Hermann-Josef Kaiser, Ilya Levental, and Kai Simons. Lipid rafts as functional heterogeneity in cell membranes. *Biochemical Society Transactions*, 37(Pt 5):955–960, 2009.

[44] Lin Chen, Zhiwu Yu, and Peter J Quinn. The partition of cholesterol between ordered and fluid bilayers of phosphatidylcholine: a synchrotron x-ray diffraction study. *Biochimica et Biophysica Acta (BBA)-Biomembranes*, 1768(11):2873–2881, 2007.

[45] Wei-Chin Hung, Ming-Tao Lee, Fang-Yu Chen, and Huey W Huang. The condensing effect of cholesterol in lipid bilayers. *Biophysical journal*, 92(11):3960–3967, 2007.

[46] Thomas J McIntosh. The effect of cholesterol on the structure of phosphatidylcholine bilayers. *Biochimica et Biophysica Acta (BBA)-Biomembranes*, 513(1):43–58, 1978.

[47] DL Worcester and NP Franks. Structural analysis of hydrated egg lecithin and cholesterol bilayers ii. neutron diffraction. *Journal of molecular biology*, 100(3):359–378, 1976.

[48] NP Franks. Structural analysis of hydrated egg lecithin and cholesterol bilayers i. x-ray diffraction. *Journal of molecular biology*, 100(3):345–358, 1976.

[49] Norbert Kučerka, Stephanie Tristram-Nagle, and John F Nagle. Closer look at structure of fully hydrated fluid phase dppc bilayers. *Biophysical journal*, 90(11):L83–L85, 2006.

[50] Jeffery B Klauda, Norbert Kučerka, Bernard R Brooks, Richard W Pastor, and John F Nagle. Simulation-based methods for interpreting x-ray data from lipid bilayers. *Biophysical journal*, 90(8):2796–2807, 2006.

[51] Norbert Kučerka, Jason D Perlmutter, Jianjun Pan, Stephanie Tristram-Nagle, John Katsaras, and Jonathan N Sachs. The effect of cholesterol on short-and long-chain monounsaturated lipid bilayers as determined by molecular dynamics simulations and x-ray scattering. *Biophysical journal*, 95(6):2792–2805, 2008.

[52] Thalia T Mills, Stephanie Tristram-Nagle, Frederick A Heberle, Nelson F Morales, Jiang Zhao, Jing Wu, Gilman ES Toombes, John F Nagle, and Gerald W Feigenson. Liquid-liquid domains in bilayers detected by wide angle x-ray scattering. *Biophysical journal*, 95(2):682–690, 2008.

[53] Yicong Ma, Sajal K Ghosh, Sambhunath Bera, Zhang Jiang, Stephanie Tristram-Nagle, Laurence B Lurio, and Sunil K Sinha. Accurate calibration and control of relative humidity close to 100% by x-raying a dopc multilayer. *Physical Chemistry Chemical Physics*, 17(5):3570–3576, 2015.

[54] Alain Caille. Remarques sur la diffusion des rayons x dans les smectiques. *CR Acad. Sci. Paris Série B*, 274:891–893, 1972.

[55] Sajal Kumar Ghosh, Sebastian Aeffner, and Tim Salditt. Effect of pip2 on bilayer structure and phase behavior of dopc: An x-ray scattering study. *ChemPhysChem*, 12(14):2633–2640, 2011.

[56] NP Franks and WR Lieb. The structure of lipid bilayers and the effects of general anaesthetics: an x-ray and neutron diffraction study. *Journal of molecular biology*, 133(4):469–500, 1979.

[57] YK Levine and MHF Wilkins. Structure of oriented lipid bilayers. *Nature*, 230(11):69–72, 1971.

[58] Thalia T Mills, Juyang Huang, Gerald W Feigenson, and John F Nagle. Effects of cholesterol and unsaturated dopc lipid on chain packing of saturated gel-phase dppc bilayers. *General physiology and biophysics*, 28(2):126, 2009.

[59] RP Rand and VA Parsegian. Hydration forces between phospholipid bilayers. *Biochimica et Biophysica Acta (BBA)-Reviews on Biomembranes*, 988(3):351–376, 1989.

[60] John Katsaras. Adsorbed to a rigid substrate, dimyristoylphosphatidylcholine multibilayers attain full hydration in all mesophases. *Biophysical journal*, 75(5):2157–2162, 1998.

[61] John Katsaras and MJ Watson. Sample cell capable of 100% relative humidity suitable for x-ray diffraction of aligned lipid multibilayers. *Review of Scientific Instruments*, 71(4):1737–1739, 2000.

[62] Norbert Kučerka, Yufeng Liu, Nanjun Chu, Horia I Petrache, Stephanie Tristram-Nagle, and John F Nagle. Structure of fully hydrated fluid phase dmpc and dlpc lipid bilayers using x-ray scattering from oriented multilamellar arrays and from unilamellar vesicles. *Biophysical journal*, 88(4):2626–2637, 2005.

[63] Nanjun Chu, Norbert Kučerka, Yufeng Liu, Stephanie Tristram-Nagle, and John F Nagle. Anomalous swelling of lipid bilayer stacks is caused by softening of the bending modulus. *Physical review E*, 71(4):041904, 2005.

[64] IM Tidswell, TA Rabedeau, Peter S Pershan, and SD Kosowsky. Complete wetting of a rough surface: An x-ray study. *Physical review letters*, 66(16):2108, 1991.

[65] Kyle J Alvine, Oleg G Shpyrko, Peter S Pershan, Kyusoon Shin, and Thomas P Russell. Capillary filling of anodized alumina nanopore arrays. *Physical review letters*, 97(17):175503, 2006.

[66] Oleg Gang, Kyle J Alvine, Masafumi Fukuto, Peter S Pershan, Charles T Black, and Benjamin M Ocko. Liquids on topologically nanopatterned surfaces. *Physical review letters*, 95(21):217801, 2005.

[67] John F Nagle and John Katsaras. Absence of a vestigial vapor pressure paradox. *Physical Review E*, 59(6):7018, 1999.

[68] John F Nagle and Stephanie Tristram-Nagle. Structure of lipid bilayers. *Biochimica et Biophysica Acta (BBA)-Reviews on Biomembranes*, 1469(3):159–195, 2000.

[69] Horia I Petrache, Stephanie Tristram-Nagle, and John F Nagle. Fluid phase structure of epc and dmpc bilayers. *Chemistry and physics of lipids*, 95(1):83–94, 1998.

[70] Tim Salditt. Thermal fluctuations and stability of solid-supported lipid membranes. *Journal of Physics: Condensed Matter*, 17(6):R287, 2005.

[71] V Adrian Parsegian. *Van der Waals forces: a handbook for biologists, chemists, engineers, and physicists*. Cambridge University Press, 2005.

[72] H Vink. Precision measurements of osmotic pressure in concentrated polymer solutions. *European Polymer Journal*, 7(10):1411–1419, 1971.

[73] G Büldt, HU Gally, J Seelig, and G Zaccai. Neutron diffraction studies on phosphatidylcholine model membranes: I. head group conformation. *Journal of molecular biology*, 134(4):673–691, 1979.

[74] W-J Sun, RM Suter, MA Knewtson, CR Worthington, S Tristram-Nagle, R Zhang, and JF Nagle. Order and disorder in fully hydrated unoriented bilayers of gel-phase dipalmitoylphosphatidylcholine. *Physical Review E*, 49(5):4665, 1994.

[75] Mark E Servantes et al. *A study of supported lipid mulitlayers in a humidity controlled environment*. PhD thesis, NORTHERN ILLINOIS UNIVERSITY, 2011.

[76] EA Evans and VA Parsegian. Thermal-mechanical fluctuations enhance repulsion between bimolecular layers. *Proceedings of the National Academy of Sciences*, 83(19):7132–7136, 1986.

[77] Horia I Petrache, Thomas Zemb, Luc Belloni, and V Adrian Parsegian. Salt screening and specific ion adsorption determine neutral-lipid membrane interactions. *Proceedings of the National Academy of Sciences*, 103(21):7982–7987, 2006.

[78] Horia I Petrache, Stephanie Tristram-Nagle, Daniel Harries, Norbert Kučerka, John F Nagle, and V Adrian Parsegian. Swelling of phospholipids by monovalent salt. *Journal of lipid research*, 47(2):302–309, 2006.

[79] Evan Evans and David Needham. Physical properties of surfactant bilayer membranes: thermal transitions, elasticity, rigidity, cohesion and colloidal interactions. *Journal of Physical Chemistry*, 91(16):4219–4228, 1987.

[80] E Sackmann. Molecular and global structure and dynamics of membranes and lipid bilayers. *Canadian Journal of Physics*, 68(9):999–1012, 1990.

[81] Curt M DeCaro, Justin D Berry, Laurence B Lurio, Yicong Ma, Gang Chen, Sunil Sinha, Lobat Tayebi, Atul N Parikh, Zhang Jiang, and Alec R Sandy. Substrate suppression of thermal roughness in stacked supported bilayers. *Physical Review E*, 84(4):041914, 2011.

[82] Thomas Hønger, Kell Mortensen, John Hjort Ipsen, Jesper Lemmich, Rogert Bauer, and Ole G Mouritsen. Anomalous swelling of multilamellar lipid bilayers in the transition region by renormalization of curvature elasticity. *Physical review letters*, 72(24):3911, 1994.

[83] Jesper Lemmich, Kell Mortensen, John Hjort Ipsen, Thomas Hønger, Rogert Bauer, and Ole G Mouritsen. Pseudocritical behavior and unbinding of phospholipid bilayers. *Physical review letters*, 75(21):3958, 1995.

[84] Georg Pabst, John Katsaras, Velayudhan A Raghunathan, and Michael Rappolt. Structure and interactions in the anomalous swelling regime of phospholipid bilayers. *Langmuir*, 19(5):1716–1722, 2003.

[85] PC Mason, JF Nagle, RM Epand, and J Katsaras. Anomalous swelling in phospholipid bilayers is not coupled to the formation of a ripple phase. *Physical Review E*, 63(3):030902, 2001.

[86] H Seto, NL Yamada, M Nagao, M Hishida, and T Takeda. Bending modulus of lipid bilayers in a liquid-crystalline phase including an anomalous swelling regime estimated by neutron spin echo experiments. *The European Physical Journal E: Soft Matter and Biological Physics*, 26(1):217–223, 2008.

[87] Stine S Korreman and Dorthe Posselt. Chain length dependence of anomalous swelling in multilamellar lipid vesicles. *The European Physical Journal E*, 1(1):87–91, 2000.

[88] Norbert Kučerka, Mu-Ping Nieh, Jeremy Pencer, Thad Harroun, and John Katsaras. The study of liposomes, lamellae and membranes using neutrons and x-rays. *Current Opinion in Colloid & Interface Science*, 12(1):17–22, 2007.

[89] Jacob N Israelachvili. *Intermolecular and surface forces: revised third edition*. Academic press, 2011.

[90] Cynthia A Stanich, Aurelia R Honerkamp-Smith, Gregory Garbes Putzel, Christopher S Warth, Andrea K Lamprecht, Pritam Mandal, Elizabeth Mann, Thien-An D Hua, and Sarah L Keller. Coarsening dynamics of domains in lipid membranes. *Biophysical journal*, 105(2):444–454, 2013.

[91] Ilya M Lifshitz and Vitaly V Slyozov. The kinetics of precipitation from supersaturated solid solutions. *Journal of Physics and Chemistry of Solids*, 19(1):35–50, 1961.

[92] Takashi Taniguchi. Shape deformation and phase separation dynamics of two-component vesicles. *Physical review letters*, 76(23):4444, 1996.

[93] Mohamed Laradji and PB Sunil Kumar. Dynamics of domain growth in self-assembled fluid vesicles. *Physical review letters*, 93(19):198105, 2004.

[94] Mohamed Laradji and PB Sunil Kumar. Domain growth, budding, and fission in phase-separating self-assembled fluid bilayers. *The Journal of chemical physics*, 123(22):224902, 2005.

[95] Sanoop Ramachandran, Mohamed Laradji, and P B. Sunil Kumar. Lateral organization of lipids in multi-component liposomes. *Journal of the Physical Society of Japan*, 78(4), 2009.

[96] Jun Fan, Tao Han, and Mikko Haataja. Hydrodynamic effects on spinodal decomposition kinetics in planar lipid bilayer membranes. *The Journal of chemical physics*, 133(23):235101, 2010.

[97] Brian A Camley and Frank LH Brown. Dynamic scaling in phase separation kinetics for quasi-two-dimensional membranes. *The Journal of chemical physics*, 135(22):225106, 2011.

[98] SA Safran. Domain growth of degenerate phases. *Physical Review Letters*, 46(24):1581, 1981.

[99] Gary S Grest and David J Srolovitz. Impurity effects on domain-growth kinetics. i. ising model. *Physical review B*, 32(5):3014, 1985.

[100] David A Huse and Christopher L Henley. Pinning and roughening of domain walls in ising systems due to random impurities. *Physical review letters*, 54(25):2708, 1985.

[101] AJ Bray and K Humayun. Universality class for domain growth in random magnets. *Journal of Physics A: Mathematical and General*, 24(19):L1185, 1991.

[102] Joel D Shore, Mark Holzer, and James P Sethna. Logarithmically slow domain growth in nonrandomly frustrated systems: Ising models with competing interactions. *Physical Review B*, 46(18):11376, 1992.

[103] R Gallego, Maxi San Miguel, and Raúl Toral. Domain growth in a multivariable nonpotential system. *Physica A: Statistical Mechanics and its Applications*, 257(1):207–212, 1998.

[104] Patrycja Paruch, T Tybell, and Jean-Marc Triscone. Nanoscale control of ferroelectric polarization and domain size in epitaxial pb (zr 0.2 ti 0.8) o 3 thin films. *Applied Physics Letters*, 79(4):530–532, 2001.

[105] PE Jönsson, H Yoshino, Per Nordblad, H Aruga Katori, and A Ito. Domain growth by isothermal aging in 3d ising and heisenberg spin glasses. *Physical review letters*, 88(25):257204, 2002.

[106] Yicong Ma, Sajal K. Ghosh, David A. DiLena, Sambhunath Bera, Laurence B. Lurio, Atul N. Parikh, and Sunil K. Sinha. Cholesterol partition and condensing effect in phase separated ternary mixture lipid multilayers. *Submitted.*

[107] S-W Chen, H Guo, KA Seu, K Dumesnil, S Roy, and SK Sinha. Jamming behavior of domains in a spiral antiferromagnetic system. *Physical review letters*, 110(21):217201, 2013.

[108] Dag Scherfeld, Nicoletta Kahya, and Petra Schwille. Lipid dynamics and domain formation in model membranes composed of ternary mixtures of unsaturated and saturated phosphatidylcholines and cholesterol. *Biophysical journal*, 85(6):3758–3768, 2003.

[109] Ulrike Mennicke and Tim Salditt. Preparation of solid-supported lipid bilayers by spin-coating. *Langmuir*, 18(21):8172–8177, 2002.